

NORTHWESTERN UNIVERSITY

Soft Tissue Cutting in Core Biopsy

A DISSERTATION

SUBMITTED TO THE GRADUATE SCHOOL
IN PARTIAL FULFILLMENT OF THE REQUIREMENTS

For the degree of

DOCTOR OF PHILOSOPHY

Field of Mechanical Engineering

By

Marco Giovannini

EVANSTON, ILLINOIS

March 2020

© Copyright by Marco Giovannini 2020

All Rights Reserved

Abstract

Soft Tissue Cutting in Core Biopsy

Marco Giovannini

Hollow biopsy needles are widely adopted medical devices for the removal of biological tissue to better identify a lesion or an abnormality observed through a physical exam or a radiology scan. These procedures can provide significantly more information than most medical tests, and they are usually performed on dermis layers, bone lesions, breast masses, lymph nodes, and the prostate. The quality of the samples mainly depends on the forces exerted by the needle during the cutting process. The reduction of these forces is critical to extract high-quality tissue samples. The most important factors that affect the cutting forces are the geometry of the needle tip and its motion while it is penetrating the tissue. However, optimal needle tip configurations and cutting parameters are not well established for biopsy procedures.

This thesis, articulated in four topics, aims to investigate the geometry and cutting forces of biopsy needles. First, analytical models related to the cutting angles of several needle tip designs are presented and compared. Several needle tip geometries were ground and tested on different phantom tissues at different speeds. Second, novel three-dimensional (3D) needle geometries were conceived, and mathematical models were formulated to compute the cutting angles and tissue fracture forces. The proposed methodology was demonstrated on helical

needles, which were then manufactured and tested on soft tissue. Third, the characterization of polyvinyl chloride (PVC) tissue, which is commonly used to mimic human skin, was performed by means of uniaxial tests. Data coming from tissue characterization were used to calibrate a 3D FEM model to predict the cutting force during the insertion of core biopsy needles. Fourth, the application of bio-inspired micro-serrated cutting edges on the cutting edge of hollow needles was considered. Micro-serrations were created by adopting laser micro-machining, and their effectiveness was verified through the development of analytical and computational models.

The outcome of this study can benefit several clinical procedures, especially core and skin biopsy, in which a cannula device is adopted to cut and collect soft tissue samples.

Acknowledgment

First all, I wish to express my sincere gratitude to my Ph.D. advisors: Professor Kornel Ehmann and Professor Jian Cao, for their guidance and support during this journey. I also would like to thank my thesis committee member, Professor Albert Shih, for his advice and collaboration. This thesis benefited from the financial support of the National Science Foundation (Grant #CMMI-0825722), the Korea Institute of Machinery & Materials, and the Ryan Fellowship.

I have been fortunate enough to work and spend time with amazing people here at Northwestern. I especially would like to acknowledge my colleagues and friends: Huaqing Ren and Newell Moser, for their help in modeling and characterizing soft tissue, and Ramin Bostanabad for his assistance in statistical modeling. I also would like to thank Robert Taglia and Scott Simpson for helping me to prepare the components for the experimental setups, Mark Seniw, for his help in the uniaxial tests of soft tissue and Mike Beltran, for making the CNC machining center available for cutting of helical needles.

During these years at Northwestern, I received an incredible support from my peers and friends: a special thanks to Amartya Banerjee, Andrea Isgrò, David Pritchett, Demeng Che, Dohyun Leem, Ishan Saxena, Mojtaba Mozaffar, Nicolas Martinez Prieto, Orion Kafka, Ricardo Dahis, Simone Bianconi, Yi Shi, and the list goes on; please forgive me if I did not include your name and accept my thanks as well.

I also would like to acknowledge the past and current members of the Advanced Manufacturing Processes Laboratory (AMPL) for their support and motivation. I cannot forget

to express my gratitude to the staff of the Department of Mechanical Engineering, especially Rick Marzec, who always provided friendly assistance.

Last but not least, I would like to thank my friends and relatives back home for their support and encouragement. Most of all, I am infinitely thankful to my family: my father, my mother, and my sister. I could not pursue this path without you.

List of Abbreviations

BP	Biopsy Punch
CAD	Computer-Aided Design
CAM	Computer-Aided Manufacturing
DIC	Digital Image Correlation
FEM	Finite Element Method
PVC	Polyvinyl Chloride

Nomenclature

\mathbf{a}	$\mathbf{t} \times \mathbf{n}_r$
A_c	Cylindrical area of the cannula in contact with the tissue
A_{co}	Area of the tissue in contact with the biopsy punch
A_{SERR}	Area of the tissue in contact with a standard biopsy punch
A_{STAND}	Area of the tissue in contact with a micro-serrated biopsy punch
A_t	Area of the tissue subjected to elastic deformation
α	Rake angle at a point on the cutting edge
β	Unknown weights
α_p	Material constant adopted in the Ogden model
\mathbf{b}	$\mathbf{t} \times \mathbf{n}$
\mathbf{B}	Left Cauchy-Green deformation tensor
β	Multiplication factor
c	Parametric covariance function
\mathbf{C}	Correlation function
γ	Angular position of a point on the needle cutting edge
γ_h	Angular position of a point on the helical profile
γ_n	Angular position of a point on the cylindrical profile
d_e	External needle diameter
d_{final}	Needle displacement at which the needle is stopped
d_i	Internal needle diameter
d_{rup}	Needle displacement at which the first crack initiates
dh	Incremental displacement along the direction of F_H
dr	Resultant needle displacement along the rake face
dv	Incremental needle displacement along the direction of F_V
D	Material constant in the Arruda-Boyce model
e_{ij}	Engineering strain
E	Young`s modulus of tissue

ε	Angle identified on the rake face
$f_i()$	Basis function
f_{Hcut}	Cutting force perpendicular to the needle axis per unit of axial displacement
f_{Vcut}	Cutting force parallel to the needle axis per unit of axial displacement
\mathbf{F}	Deformation gradient
\mathbf{F}_{exp}	Vector of experimental fracture forces
F_F	Friction force
F_{FH}	Friction force perpendicular to the needle axis
F_{FV}	Friction force parallel to the needle axis
F_H	Force perpendicular to the needle axis
F_{Hcut}	Cutting force perpendicular to the needle axis
F_{Hel}	Tangential force due to the elastic tissue deformation
F_{Hrup}	Fracture force perpendicular to the needle axis
F_{Hf}	Force perpendicular to the needle axis at the final penetration depth
F_N	Force acting on the external surface of the needle
F_{surf}	Surface function representing the surface of a conical needle tip
F_V	Force parallel to the needle axis
F_{Vcut}	Cutting force parallel to the needle axis
F_{Vel}	Axial force due to the elastic tissue deformation
F_{Vf}	Force parallel to the needle axis at the final penetration depth
F_{Vrup}	Fracture force parallel to the needle axis
F_{\perp}	Fracture force perpendicular to the cutting edge
F_{\parallel}	Fracture force parallel to the cutting edge
θ	Included angle at a point on the cutting edge
\mathbf{g}	$n \times 1$ vector with i^{th} element $c(\mathbf{x}_i, \mathbf{x}^*) = \hat{\sigma}^2 r(\mathbf{x}_i, \mathbf{x}^*)$
G	Geometrical factor
\mathbf{h}	$\mathbf{1} - \mathbf{1}^T \mathbf{V}^{-1} \mathbf{g}(\mathbf{x}')$
η	Poisson ratio of tissue
I_k	Left Cauchy-Green deformation tensor invariants
J	Determinant of deformation tensor

J_e	Nonlinear energy release rate
l_b	Bevel length
l_c	Length of the cutting edge with respect to the needle axis
l_{fin}	Final length of the tissue column
l_{init}	Original length of the tissue column
l_t	Total needle length
k	Slice/push ratio
K	Shear constant
K_i	Crack intensification factor
λ	Inclination angle at a point on the cutting edge
λ_k	Principal stretches
λ_m	Locking stretch
μ	Shear modulus of the Arruda-Boyce model
μ_d	Coulomb dynamic friction coefficient
μ_{da}	Coulomb dynamic friction coefficient along the axial direction
μ_{dr}	Coulomb dynamic friction coefficient along the tangential direction
μ_p	Material constants adopted in the Ogden model
m	Coefficient that accounts for the nonlinearity of the material
n_s	Number of micro-serrations
\mathbf{n}	Normal vector to the xy -plane
\mathbf{n}_c	Normal vector to the cylindrical surface
\mathbf{n}_r	Normal vector to the rake face
\mathbf{n}_u	Unit vector normal to the rake face
N	Material constant adopted in the Ogden model
N_R	Contact force applied on the rake face
$OXYZ$	Coordinate system assigned to the needle tip for grinding
$O^*X^*Y^*Z^*$	Coordinate system assigned to the grinding surface
ξ	Bevel angle
ξ_0	Zero-mean Gaussian Process
p	Hydrostatic stress

p_h	Pitch of the helix
p_n	Contact pressure
P_l	Number of planes in multi-plane needles
P_{ij}	Engineering stress
q	Number of responses
r_c	Radius of the arc of the micro-serration
r_h	Radius of the conical helix
r_n	Radius of the needle
r_{ni}	Internal radius of the needle
r_{no}	External radius of the needle
r_s	Radius at the tip of the micro-serration
$r_{sph}, \theta_{sph}, z_{sph}$	Spherical coordinate system - spatial coordinates
$R_{sph}, \Theta_{sph}, Z_{sph}$	Spherical coordinate system - material coordinates
r_t	Radius of the deformed tissue column
r_{tip}	Radius of the needle tip
R	Strain energy release rate
\mathbf{R}_n	Rotation Matrix
ρ	Angle between micro-serrations
S	Needle rotation/translation ratio
σ_{ij}	Cauchy Stress
σ_v^2	Process variance
\mathbf{t}	Tangent vector to the cutting edge
\mathbf{t}_u	Unit vector tangent to the cutting edge
T_{el}	Torque due to the elastic tissue deformation
U	Strain energy density function
\mathbf{v}	Velocity vector
v_r	Needle rotational velocity
v_a	Needle axial velocity
v_{\perp}	Velocity perpendicular to the cutting edge
v_{\parallel}	Velocity parallel to the needle's cutting edge

\mathbf{V}	Covariance matrix
w	Length of the cutting edge
W_C	Work needed to propagate the crack
W_F	Work performed by the friction force
W_N	Work performed by the needle
φ	Inclination angle of the cylindrical surface
ϕ	Rotation angle between consecutive bevel planes
ϕ_g	Angle included between the grinding surface and Z^*
\mathbf{x}	Inputs of computer simulator
\mathbf{X}_n	Vector of the coordinates of the cylindrical needle surface
$\mathbf{X}_{n\varphi}$	Vector of the coordinates of the cylindrical surface inclined at an angle φ
$y(\mathbf{x})$	Random process
xyz	Coordinates of the needle tip
$x_h y_h z_h$	Coordinates of the conical helix
$x_i y_i z_i$	Coordinates of a point on the internal cutting edge
$x_n y_n z_n$	Coordinates of the cylindrical needle surface
$x_o y_o z_o$	Coordinates of a point on the external cutting edge
$x_{n\varphi} y_{n\varphi} z_{n\varphi}$	Coordinates of the cylindrical surface inclined at an angle φ
\mathbf{y}	Responses in the training data set
ψ	Angle of the helix
$\mathbf{\Omega}$	$diag(\mathbf{10}^\omega)$
ω	Scale parameters

Dedication

Dedico questa tesi ai miei genitori. Grazie di cuore per tutti i sacrifici fatti per me in questi anni e per il vostro amore incondizionato.

Table of contents

Abstract	3
Acknowledgment.....	5
List of Abbreviations	7
Nomenclature	8
Dedication.....	13
Table of contents	14
List of Tables.....	18
List of Figures	20
1 Introduction.....	25
1.1 Motivation.....	25
1.2 Objectives.....	27
1.3 Literature review	28
1.3.1 Cutting edge geometry.....	28
1.3.2 Micro-serration effect	31
1.3.3 Cutting motion	35
1.4 Outline	38
2 Design and Cutting Motions of Rotating Needles.....	40
2.1 Mathematical Models for Rotating Hollow Needles.....	40
2.1.1 Analytical Models for Conical and One-Plane Bevel Cannulas.....	41
2.1.2 Analytical Models for Symmetric Multi-Plane Cannulas.....	43
2.2 Analytical Models for Insertion Cutting Forces	45
2.2.1 Fracture Force.....	46
2.2.2 Cutting Force	50
2.3 Experimental Methods for Rotating Needles.....	52
2.3.1 Needle Grinding Process.....	53
2.3.1.1 Coordinate systems and kinematics in needle grinding.....	53
2.3.1.2 Five-axis needle grinding machine	55
2.3.2 Insertion Testbed.....	57
2.3.3 Phantom Tissue	58

	15
2.4 Impact of Different Needle Tips on Cutting Forces	59
2.4.1 Needle Tip Effect on Conical and One-Plane Bevel Needles	60
2.4.2 Needle Tip Effect in Symmetric Multi-Plane Needles.....	64
2.5 Impact of Different Cutting Motions on Cutting Forces.....	66
2.5.1 Impact of the Slice/Push Ratio on Cutting Forces	66
2.5.2 Impact of the Slice/Push Ratio at Different Axial Speeds	70
2.5.3 Impact of the Slice/Push Ratio for Different Materials	72
2.6 Conclusions on Rotating Needles	73
3 Design and Models of Helical Hollow Needles.....	76
3.1 Mathematical Models for Helical Needles	77
3.1.1 Geometric Description	77
3.1.2 Inclination Angle (λ).....	82
3.1.3 Included Angle (θ).....	85
3.1.4 Rake Angle (α)	87
3.1.5 Fracture Forces and Slice/Push Ratio	89
3.2 Manufacturing Process for Helical Needles.....	92
3.3 Impact of Helical Needles on Experimental Cutting Forces.....	94
3.3.1 Helical Needle`s Impact on Cutting Forces.....	94
3.3.2 Helical Needle`s Impact at Different Slice/Push Ratios.....	96
3.4 Optimization of Helical Geometry	98
3.4.1 Review on Gaussian Process Modeling	99
3.4.2 GP Application to Helical Needle Geometry	103
3.5 Conclusions on Helical Needles	105
4 Soft Tissue Characterization.....	107
4.1 Experimental Methods for Uniaxial Tests.....	108
4.1.1 Tension Test.....	108
4.1.2 Compression Test	109
4.2 Soft Tissue Constitutive Models	110
4.2.1 Arruda-Boyce Model.....	112
4.2.2 Ogden Model.....	113
4.2.3 Identification of Material Constants.....	113

	16
4.3 Analytical Force	115
4.3.1 Needle Insertion without Rotation	115
4.3.2 Needle Insertion with Rotation	117
4.4 Finite Element Model Validation for Hollow Needles	120
4.4.1 Hollow Needle Insertion without Rotation	120
4.4.1.1 3D Finite Element Model.....	120
4.4.1.2 2D Finite Element Model.....	125
4.4.2 Hollow Needle Insertion with Slicing Motion.....	129
4.4.3 Estimation of the Friction Coefficient in Tissue Cutting.....	133
4.5 Conclusions on Tissue Characterization.....	136
5 Micro-Texturing of Hollow Needles for Skin Biopsies	138
5.1 Experimental Setup for Micro-Serrated Biopsy Punches	139
5.1.1 Laser Ablation Process	139
5.1.2 Micro Serration Design.....	140
5.2 Fracture Mechanics Approach	142
5.3 Experimental Cutting Forces of Micro-Serrated Biopsy Punches	144
5.3.1 Insertion of Micro-Serrated BPs	145
5.3.2 Texture Depth Effect in Micro-Serrated BP Insertion.....	148
5.4 Computational Study of BP Insertion.....	149
5.4.1 Computational Study of Micro-Serrated BPs.....	150
5.4.2 Computational Study of Different Micro-Serrations.....	155
5.5 Conclusions on Micro-Serrated Biopsy Punch Insertion.....	158
6 Conclusions and Future Work	159
6.1 Conclusions.....	159
6.2 Future Work.....	162
References	164
Appendix A: Soft Tissue PVC Parameters	173
A1. S/P ratio: 0.25	173
A2. S/P ratio: 0.5	173
A3. S/P ratio: 1.....	173
Appendix B: Abaqus Input Files.....	174
B1. 3D FEM Model.....	174

	17
B2. 2D FEM Model.....	178
B3. 3D FEM Model: Insertion with Slicing Motion	181
B4. 3D FEM Model: Micro-Serrated Biopsy Punches	186
B5. 2D FEM Model: Micro-Serrated Biopsy Punches	190
Appendix C: Code for Laser Ablation.....	193

List of Tables

Table 2.1. Young's modulus for each phantom tissue characterized by a different softener/plastic ratio (S/P).....	59
Table 2.2. The mean value (μ), standard deviation (σ), p-value, t-test result, and force variation (ΔF_{Vf}) related to the value of the force in the axial direction at the maximum penetration depth for cylindrical (cyl.), conical (con.), one-plane (bev.) and two- and three-plane needles.	62
Table 2.3. The mean value (μ), standard deviation (σ), p-value, t-test result, and force variation (ΔF_{Hf}) related to the value of the force in the tangential direction at the maximum penetration depth for cylindrical (cyl.), conical (con.), one-plane (bev.) and two- and three-plane needles.	63
Table 2.4. Function parameters that are necessary to calculate the theoretical values of the axial and tangential cutting force (Eqs. (2.16)-(2.17)).....	67
Table 2.5. Polynomial regression equation with related R^2 and RMSE for dynamic friction coefficients as a function of the slice/push ratio (k).	68
Table 2.6. Polynomial regression equation with related R^2 and RMSE values for the axial and tangential forces as a function of the slice/push ratio (k) and speed (v_t).....	71
Table 2.7. Polynomial regression equation with related R^2 and RMSE values for the axial and tangential forces as a function of the slice/push ratio (k) and Young's modulus (E).....	73
Table 3.1. Needle tip profiles and their derivatives for the outside ($z_o(\gamma)$) and inside cutting edges ($z_i(\gamma)$) (Han et al., 2012; Moore et al., 2012b).....	85
Table 3.2. Cutting parameters (θ, λ, α) for helical and bevel needles.....	89
Table 3.3. The mean value (μ), standard deviation (σ), p-value, and force variation (ΔF) for helical and bevel needles. The p-value is not reported for bevel needle insertions since they represent the term of comparison.....	96
Table 3.4. Objective function F , with the computed values for the input angles (ψ, φ).....	104
Table 4.1. Material constants and fitting coefficients for each material model for a mixture with an S/P ratio equal to 0.....	115
Table 4.2. Polynomial regression equation with related R^2 and RMSE for the dynamic friction coefficients as a function of the slice/push ratio (k).	134

Table 5.1. Serration configurations. Each configuration is identified by a different micro-serration radius (r_c) (Fig. 5.2).....	141
Table 5.2. The mean value (μ), standard deviation (σ), p-value and force variation value presented for each serration configuration.....	149
Table A1. Material constants and fitting coefficients for phantom tissue with an S/P ratio equal to 0.25.....	173
Table A2. Material constants and fitting coefficients for phantom tissue with an S/P ratio equal to 0.5.....	173
Table A3. Material constants and fitting coefficients for phantom tissue with an S/P ratio equal to 1.....	173

List of Figures

Figure 1.1. Biopsy procedures: (a) bone marrow biopsy (National Cancer Institute © (2007) Terese Winslow LLC, U.S. Govt. has certain rights), (b) skin biopsy (image by BruceBlau, distributed under a CC BY-SA 4.0 license).....	26
Figure 1.2. Biopsy needles: (a) commercial bone marrow biopsy needle “Jamshidi,” (b) hollow cannula cross-section, and (c) multi-plane symmetric and nonsymmetric needles (Moore et al., 2010).....	29
Figure 1.3. SEM images of a honeybee’s stinger and of an acupuncture needle: (a) stinger, (b) stinger tip, (c) barbs on the stinger, (d) and acupuncture needle (Ling et al., 2017).	32
Figure 1.4. Effect of jagged shape on stress concentration (Aoyagi et al., 2008).	34
Figure 1.5. Rotating needles: (a) revolving needle driver supported by a Remote Center of Motion (RCM) orientation module and (b) target displacements with no-revolve, when rotating while inserting and after the insertion (post-revolve) (Badaan et al., 2011).....	36
Figure 1.6. An example of resistance force detected by the load cell for insertion with (a) straight and (b) jagged microneedle at a vibration of 30 Hz (Izumi et al., 2008).....	37
Figure 2.1. Illustration of needle geometries: (a) conical and (b) one-plane bevel cannula tip geometries (b).	41
Figure 2.2. (a) Included angle θ and (b) inclination angle λ for conical bevel cannulas.....	42
Figure 2.3. (a) Illustration of the tip geometry of two-plane, (b) three-plane bevel cannulas, and (c) its 3D scan after manufacturing, with the deviations with respect to the CAD model. ...	43
Figure 2.4. (a) Included angle θ and (b) inclination angle λ for multi-plane cannulas.....	44
Figure 2.5. (a) 3D model of the cannula with cutting forces (F_V , F_H) and (b) their behavior during needle penetration highlighting the cutting phases (I, II), the rupture forces (F_{Vrup} , F_{Hrup}) and the final axial and tangential forces (F_{Vf} , F_{Hf}).....	46
Figure 2.6. 3D model of the cutting edge during a slicing motion.	47
Figure 2.7. Free body diagram of the tool.....	48
Figure 2.8. (a) Fracture forces (F_{Vrup} , F_{Hrup}) vs. different slice/push ratios, calculated for different friction coefficients (μ_d) and (b) different strain energy release rates, R	49
Figure 2.9. Geometric schematics with coordinate systems of the needle grinding process. ...	53
Figure 2.10. (a) Grinding machine system and (b) the schematics of the main axes.	56

Figure 2.11. Testbed for the measurement of cutting forces and torques.....	57
Figure 2.12. (a) Fracture (F_{Vrup} , F_{Hrup}) and (b) cutting force values (F_{Vcut} , F_{Hcut}) for cylindrical ($\theta = 90^\circ$), conical and one-plane bevel needles ($\theta = 15^\circ, 45^\circ, 75^\circ$).....	61
Figure 2.13. (a) Axial force (F_V) and (b) tangential force (F_H) during needle penetration for cylindrical ($\theta = 90^\circ$), conical ($\theta = 15^\circ$) and one-plane bevel needles ($\theta = 15^\circ, 45^\circ, 75^\circ$).....	63
Figure 2.14. Fracture (F_{Vrup} , F_{Hrup}) and cutting force values (f_{Vcut} , f_{Hcut}) for needles with one, two, three, and infinite (cylindrical) number of planes.....	64
Figure 2.15. (a) Axial force (F_V) and (b) tangential force (F_H) behavior during needle penetration for cylindrical, one-plane, and multi-plane bevel needles ($\theta = 15^\circ$).....	65
Figure 2.16. Mean value and error bar of fracture forces (F_{Vrup} , F_{Hrup}) and the related analytical model curves (Eqs. (2.16)-(2.17)).	68
Figure 2.17. Mean values and error bars of cutting force (f_{Vcut} , f_{Hcut}) and the related analytical model curves (Section 2.2.2, Table 2.5).	69
Figure 2.18. (a) Axial force (F_V) and (b) tangential force (F_H) behavior during needle penetration for different slice/push ratios, k	69
Figure 2.19. (a) Maximum axial forces (F_V) and (b) tangential forces (F_H) for insertions performed at different slice/push ratios and different insertion speeds. The experimental points with related error bars are also shown.	70
Figure 2.20. (a) Maximum axial forces (F_V) and (b) tangential forces (F_H) for insertions performed at different slice/push ratios on different phantom materials. The experimental points with related error bars are also shown.	72
Figure 3.1. (a) Illustration of the breast biopsy device “Mammotome,” (b) hollow needle generated by a 2D profile, and (c) hollow needle generated by a 3D profile.	77
Figure 3.2. (a) Schematics of the intersection between the conical helical surface and the cylindrical surface and (b, c) the 3D geometrical model.....	79
Figure 3.3. (a) Illustration of the helical needle’s cutting edge and (b) its 3D scan after manufacturing, with the deviations with respect to the CAD model.....	80
Figure 3.4. (a) Illustration of one-plane bevel cutting edge and (b) the related 3D scan after manufacturing, with the deviations with respect to the CAD model.....	81
Figure 3.5. (a) Fourier fitting and analytical models (Table 3.1) for the outside and (b) inside cutting edge profiles of helical and bevel needles.	83
Figure 3.6. (a) Inclination angle (λ), for helical and bevel needles with respect to the angle γ and (b) to the distance z from the starting point of the cutting edge.....	84

Figure 3.7. SEM pictures showing: (a) the helical and (b) bevel needle tips.....	84
Figure 3.8. (a) Illustration of the mesh of the rake face, (b) the related normals for a few selected points of the mesh, and (c) the values of the angle θ	86
Figure 3.9. (a) Included angle, θ , for helical and bevel needles vs. the angle γ and (b) vs. the distance z from the starting point of the cutting edge.	87
Figure 3.10. (a) Rake angle, α , for helical and bevel needles vs. the angle γ and (b) vs. the distance z from the start point of the cutting edge.....	88
Figure 3.11. Helical cannula tip. The geometry and the main vectors representing directions, velocities, and forces.....	90
Figure 3.12. (a) Fracture force values for helical and bevel needles vs. the angle (γ) for a rotation/translation ratio (S), equal to 0.3 and (b) the behavior of the mean value of the fracture forces for different rotation/translation ratios (S).	91
Figure 3.13. VF-2 Haas vertical machining center with the motion axes (X, Y, Z) and the main components of the manufacturing setup highlighted.....	93
Figure 3.14. (a) Cutting force behavior in the axial (F_a) and (b) tangential direction (F_t) for helical and bevel needles.....	95
Figure 3.15. The mean value, error bar, and analytical values of fracture forces.	98
Figure 3.16. GP model scheme for the optimization of the helical needle geometry.....	100
Figure 3.17. (a) Cutting length (l_c) and (b) the maximum value of the inclination angle (λ) for different combinations of inputs, as predicted by the GP model.	104
Figure 4.1. Uniaxial tension testbed with the DIC 3D System.	109
Figure 4.2. Setup for the compression test and related mold.....	110
Figure 4.3. True Cauchy stress (σ_{11}) vs. stretches (λ_1) in the axial direction for a mixture with an S/P ratio equal to 0, coming from different samples.	114
Figure 4.4. True Cauchy stress (σ_{11}) vs. stretches (λ_1) in the axial direction for a mixture with an S/P ratio equal to 0.....	114
Figure 4.5. Comparison of axial forces obtained from the analytical model with the experimental measurements performed on the testbed (Section 2.3.2). The cannula was moving at the same axial speed as during the material testing (1 mm/s).....	117
Figure 4.6. (a) Comparison of axial and (b) tangential forces obtained from the analytical model with the experimental measurements performed on the testbed (Section 2.3.2). The cannula was moving at the same axial speed as during the material testing (1 mm/s).	119

- Figure 4.7.** Schematics of a BP (or hollow needle) tip: (a) CAD model and (b) cross-section showing the inner diameter (d_i), outer diameter (d_e), total length (l_t), bevel length (l_b), cutting tip radius (r_{tip}) and included angle (θ). 121
- Figure 4.8.** 3D Finite element model of hollow needle insertion. The geometry of the cannula and of the soft tissue is shown in the 3D view (a). The mesh is refined in the proximity of the cutting-edge area (b). 122
- Figure 4.9.** (a, c) Contour plots of the maximum principal stress for a cannula inserted to a penetration depth of 1 mm and (b, d) of 5 mm. 124
- Figure 4.10.** Comparison of axial forces obtained from the 3D FEM simulation with the experimental measurements performed on the testbed. The cannula was moving at the same axial speed adopted during the material testing (1 mm/s). 125
- Figure 4.11.** 2D Finite element model of hollow needle insertion. The mesh and geometry of the soft tissue are shown in the side view (a). The elements were swept around the simulation axis to provide a 3D view of the simulation (b). 126
- Figure 4.12.** Contour plot of the maximum principal stress at the contact zone between the cannula and soft tissue for (a) 3D and (b) 2D FEM model (b). 127
- Figure 4.13.** Comparison of axial forces obtained from the experimental measurements and from the 2D and 3D finite element simulation. The cannula was moving at the same axial speed adopted during the material testing (1 mm/s), without any rotation. 128
- Figure 4.14.** 3D Finite element model of hollow needle insertion. The mesh of the BP and of the soft tissue is shown: (a) in the side view, (b) 3D view, and (c) top view. (d) The mesh is refined in the proximity of the cutting-edge. 130
- Figure 4.15.** (a,b) Configuration of the soft tissue during deformation for the different 3D FEM models and (c) experimental and computational values of the axial force. 131
- Figure 4.16.** (a, b) Contour plot of maximum principal stress for the insertion of a cannula and experimental and computational values of the (c) axial force and (d) torque. The cannula axial speed was equal to 1 mm/s with a slice/push ratio, k , equal to 0.5. 132
- Figure 4.17.** (a) Mean values and error bars of the cutting forces (f_{Vcut} , f_{Hcut}) the analytical model curves (Eqs. (4.35)-(4.36), Table 4.2), and (b) the related friction coefficients. 134
- Figure 4.18.** Experimental and computational values of the (a) axial force and (b) torque for different values of the friction coefficient (μ_d). The cannula axial speed is equal to 1 mm/s with a slice/push ratio, k , equal to 0.5. 135
- Figure 5.1.** The axes of the motion system (X, Y, Z, B, C) and the main components of the laser setup are highlighted. 139

- Figure 5.2.** (a) Laser path for generating serrations on BP's cutting edge and (b) the geometry of the micro-serrations..... 140
- Figure 5.3.** Optical image of micro-serrations generated on BP's cutting tip. The external diameter is equal to 2.4 mm, internal diameter to 2 mm, while the arc radius of the BP's micro-serrations is equal to 400 μm 142
- Figure 5.4.** 3D geometric model of (a) standard and (b) micro-serrated BP. The contact area at the BP tip is highlighted..... 144
- Figure 5.5.** (a) Testbed for the measurement of cutting forces of biopsy punches and (b) axial force behavior for a commercial BP highlighting the different penetration phases. 145
- Figure 5.6.** Axial force at puncture for a standard biopsy punch BP with and without "C₄" micro-serrations (Table 5.1) at an insertion speed of 0.25 mm/s..... 147
- Figure 5.7.** Mean value and error bar of puncture force for standard and textured BPs with different micro-serration radius, r_c (Fig. 5.2). 148
- Figure 5.8.** 3D Finite element model for insertion with (a) standard and (b) and micro-serrated. The mesh is refined in the proximity of the micro-serrations (c, d). 151
- Figure 5.9.** Contour plot of maximum principal stress for the insertion of (a) micro-serrated and (b) standard BP. In the zoomed area, the BP cutting edge is hidden in order to show the stress distribution in the contact area. 153
- Figure 5.10.** Comparison of axial forces obtained from the experimental measurements and from the finite element simulation for standard and serrated BPs. 154
- Figure 5.11.** 2D Finite element model of biopsy punch insertion. The mesh and geometrical dimensions of the model are highlighted. 156
- Figure 5.12.** Contour plot of the maximum principal stress related to the insertion of a biopsy punch with a micro-serration radius of (a) 50 μm and (b) 600 μm 157
- Figure 5.13.** Comparison of axial forces obtained from the 2D FEM simulations related to insertions performed with a standard biopsy punch and with biopsy punches, characterized by micro-serration radii ranging from 50 μm to 600 μm 157

1 Introduction

1.1 Motivation

Numerous surgical cutting tools such as medical needles and biopsy punches are frequently used in minimally invasive procedures, aimed both at the extraction of tissue and at the delivery of medical fluids for common operations like regional anesthesia and special treatments.

Bone marrow biopsy (Fig. 1.1) is a critical medical procedure that is aimed at the removal of a small amount of fluid and cells from inside the bone. This procedure is of vital importance to diagnose diseases and disorders associated with red and white blood cells such as thrombocytopenia and leukemia. During bone marrow biopsies (Krause, 1981), a stainless steel hollow needle with an external diameter ranging from 18 to 11-gauge is inserted at the targeted location by a rotational motion to sever the tissue (Fig. 1.1a). Then, a tissue sample is extracted by using a syringe or other means.

A similar procedure to bone marrow biopsy is adopted by several breast biopsy devices such as the Mammotome (Devicor Medical Product, Inc.), where a rotational biopsy needle, typically of 14-gauge, is used to cut and extract tissue samples (Shin, 2016). Breast cancer is one of the most commonly diagnosed cancers among American women (American Cancer Society, 2017), and breast biopsy is the fundamental test for diagnosis.

Similar needles are used for skin biopsies, whereby a cutaneous lesion is extracted and delivered to a pathologist to perform the diagnosis. In punch biopsy, hollow needles—usually called biopsy punches (BP)—are pressed down into the skin to extract a tissue sample. BPs are the primary medical tools adopted for diagnosing skin disorders (Zuber, 2002) such as skin

cancer, which has a higher incidence than all other cancers combined in the United States (Linoss et al., 2016). If a punch biopsy is performed incorrectly, a pathologist's interpretation of a skin biopsy can be limited or erroneous.

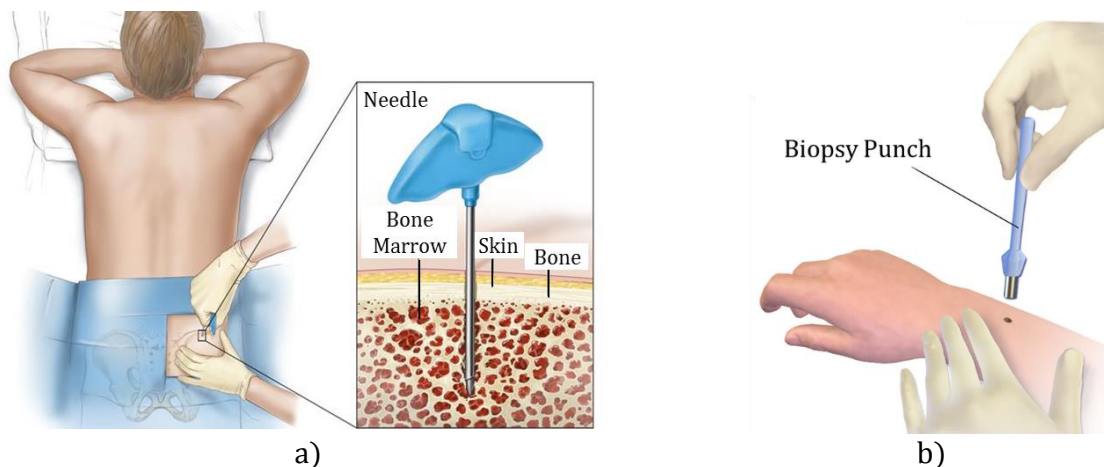


Figure 1.1. Biopsy procedures: (a) bone marrow biopsy (National Cancer Institute © (2007) Terese Winslow LLC, U.S. Govt. has certain rights), (b) skin biopsy (image by BruceBlaus, distributed under a CC BY-SA 4.0 license).

In the above-described medical procedures, the ability of the hollow needle to effectively sever the biological tissue, without compromising the quality of the samples before their extraction, is a critical factor. In fact, it was observed that larger biopsy samples could be obtained by lowering the forces applied to the needle during the cutting process (Moore et al., 2012a).

Needle insertion accuracy is another issue that arises during biopsy procedures, because: (i) the needle tends to deflect on its route to the target (Abolhassani & Patel, 2006a) and (ii) the targeted sample is constantly moving during needle insertions (Oldfield et al., 2015). Both effects are caused by the mechanical behavior of soft tissue, which experiences large deformations before the fracture is initiated.

Although the above medical procedures have been widely adopted, the problems related to the optimal cutting of soft tissue have, so far, not been completely addressed. In this research, the focus will be placed on the cutting performances of hollow needles, which are mainly adopted for core biopsy procedures.

1.2 Objectives

The work presented in this thesis aims to enhance the fundamental understanding of tissue cutting by investigating: (i) the geometry and (ii) the cutting motions of medical needles.

The first goal of this research is to investigate the design of the needle tips and propose novel geometries. The geometry of the needle's cutting edge fulfills a critical function in enhancing the cutting of soft tissue to maximize the quantity of the tissue sample that can be extracted. Since the dawn of modern medicine, only a few studies have proposed novel needle tip configurations. In this research, helical cutting edges characterized by a three-dimensional (3D) profile and micro-serrated cutting edges are conceived, analyzed, and tested.

The second goal of this research is to study the cutting motions of medical needles. Nowadays, most of the tissue cutting performed in clinical environments relies on the judgment and ability of the physician or the surgeon to perform the cut. However, in the foreseeable future, the number of incisions and medical operations assisted by automated arms and robots will increase. This will enhance the performance of cutting procedures by assigning specific speeds and motions to medical devices to ease and optimize tissue cutting.

Computational and analytical methods will be proposed to study the impact of novel cutting edges and motions on the cutting efficiency in soft tissue. All the investigated medical devices

will undergo comprehensive testing on a customized testbed by adopting phantom soft tissue samples that approximate human tissue.

The proposed general approaches (analytical, computational, and experimental) are intended to prove the effectiveness of the proposed novel ideas and their applicability to current medical devices and procedures. The hope is that the results of this research can be used to develop smarter cutting tools and automated systems for surgical simulation and robot-assisted surgical procedures.

1.3 Literature review

A review of the state of the art in tissue cutting is now presented in this section. The impact of needle cutting edge geometries on cutting forces and on the overall quality of the extracted tissue samples (Section 1.3.1) has been previously researched. However, few studies were focused on the application of serrated and micro-serrated patterns on the cutting edge of medical devices to enhance their performances (Section 1.3.2). Further, only a few research explored the implementations of different motions (rotational, vibrational) during soft tissue cutting (Section 1.3.3).

1.3.1 Cutting edge geometry

The force required to cut soft tissue is highly affected by the geometry of the cutting edge of the medical device being used. The geometry is mainly defined by its included angle θ and its radius (Han et al., 2012). Small values of both the included angle ($15^\circ\sim 30^\circ$) and of the cutting edge radius ($10\sim 20\ \mu\text{m}$) are crucial to achieving the maximum possible cutting edge sharpness (Atkins, 2009). In this regard, it was assessed (Atkins, 2009) that small included angles and

cutting edge radii eventually lead to improved sharpness of the cutting tool (Marsot et al., 2007; McCarthy et al., 2010; Mcgorry et al., 2005; Moore et al., 2010).

Moore et al. (Moore et al., 2010) derived relationships between the inclination angle, rake angle and the needle tip insertion length for different needle tip styles and assessed how they directly affect the cutting force and the quality of the biopsy tissue sample. In a separate study, Moore et al. (Moore et al., 2012a) also observed that the geometry of the needle tips directly affects the insertion force and the biopsy sample size.

A core biopsy needle is mainly composed of a hollow cannula, which is characterized by an outer and inner diameter (Fig. 1.2). Commercially, different needle tip geometries are offered, which range from the one-plane bevel tip to multi-plane needles characterized by planes oriented symmetrically or asymmetrically.

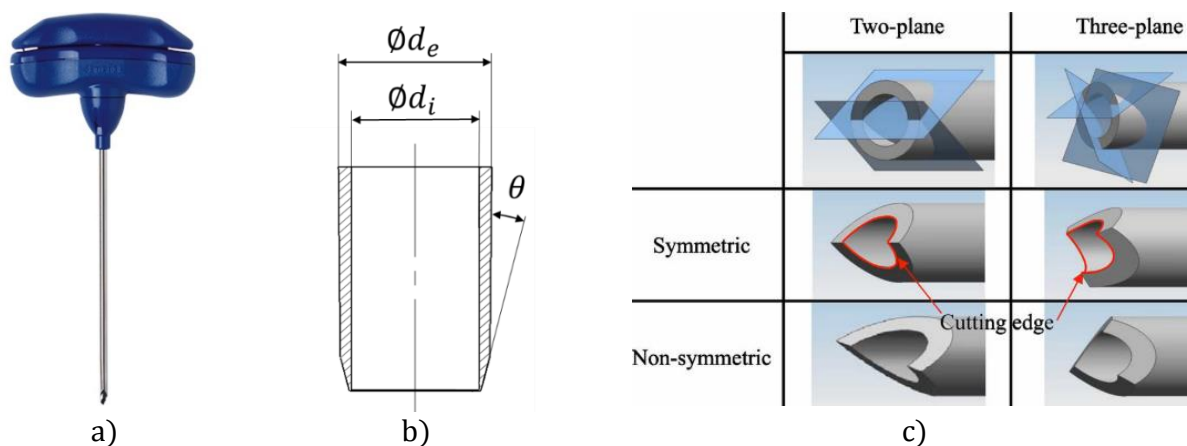


Figure 1.2. Biopsy needles: (a) commercial bone marrow biopsy needle “Jamshidi,” (b) hollow cannula cross-section, and (c) multi-plane symmetric and nonsymmetric needles (Moore et al., 2010).

Few researcher studies (Han et al., 2012; Moore et al., 2012b) have specifically analyzed the cutting parameters of different needle geometries including the inclination angle, the included

angle and the rake angle as they are defined in oblique cutting (Boothroyd & Knight, 2005; David A. Stephenson, 2016). Han et al. (Han et al., 2012) provided analytical models for the determination of the included and inclination angles for different needle cutting edges. The goal was to achieve a deeper understanding of the effect of different needle geometries (one-plane, multi-planes) on the angles defined at the needle's cutting edge. Moore et al. (Moore et al., 2011) applied the principles from metal cutting theory to model hollow biopsy needle tips and to identify the geometrical parameters that uniquely define their geometry.

Despite the abundance of research on the influence of cutting angles on the performances of needles and blades, few studies have analyzed the cutting motion that is adopted during bone marrow and breast biopsy procedures, where a hollow needle is advanced to a depth ranging from 20 to 80 mm while it is rotated. Furthermore, no studies have demonstrated the ability of novel needle tip geometries to lower the cutting forces of rotating hollow needles for biopsy procedures. Current needle tip geometries are mainly composed of one or multiple surfaces formed by two-dimensional (2D) profiles, which are extruded in one or more directions (Han et al., 2012; Moore et al., 2012b). This geometrical limitation simplifies the manufacturing process of the needle. However, current technology allows for the generation of virtually any three-dimensional (3D) surface, and while it may require a more sophisticated manufacturing process, it can also provide more efficient cutting capabilities. In this work, 3D needle tip geometries will be proposed, which are inspired by helical drills commonly used for cutting of polymers and metals (Che et al., 2012; Ehmann & Malukhin, 2012; Lin et al., 1995). A similar helical shape, described by its implicit surface equation, was proposed by Ehmann et al. (Ehmann et al., 2012). However, not all 3D needle geometries can be expressed in analytical form, and if the final needle geometry originates from the intersection of parametric surfaces, the application of numerical

methods is necessary to determine the 3D needle profile (Barnhill & Kersey, 1990; Hartmann, 2003), as it will be described in Chapter 3. Further, the medical devices proposed in the prior art (Che et al., 2012) were not manufactured and tested on phantom tissue to observe the effect of the helical geometry on the insertion forces.

1.3.2 Micro-serration effect

The presence of serrations on the cutting edge of kitchen knives and garden tools is quite common, and their general benefits to the cutting process that are also observable in nature are well established (Meyers et al., 2008). For instance, serrated cutting edges are usually adopted when slicing through fibrous materials, since serrated edges tend to “grab” or grip the surface. In fact, because the high points on the serration meet the object first, there will be more pressure per area available at these high points that will ease the initiation of the cutting process. Moreover, plain cutting edges will also lose their sharpness faster than serrated edges. This happens because, during a cutting process, the tip of the serrations will be responsible for the first contact with the soft tissue, thus becoming dull first, but also preventing the inner curvature of the serrations from early-stage damage. However, beyond these preliminary considerations, little research has been performed about the effectiveness of serrations and the relationships between their geometry, size, and cutting performance for their prospective application in medical devices.

In seeking a better approach to study the generation of serration patterns on the cutting edge of medical devices, Atkins and several other researchers (Atkins, 2009; Chen et al., 2012; Meyers et al., 2008) have already performed some preliminary studies related to the presence of

serrated cutting edges that mimic certain animal features, such as the quill of a porcupine, spine of a caterpillar, stinger of a bee, a mosquito's proboscis and a fish's teeth.

Cho et al. (Cho et al., 2012) investigated the cutting capabilities of the quills of porcupines. They observed that the microscopic barbs on the quill have a fundamental role in minimizing the force necessary for penetration. An analogous phenomenon was also noticed by Ma et al. (Ma et al., 2011), who studied the microstructure of a caterpillar's spine, capable of penetrating the skin with a minimal insertion force (about 173 μN) and without fracture. Ling et al. (Ling et al., 2016, 2017) observed similar effects when investigating the impact of a honeybee's stinger and its microstructured barbs on insertion and pull forces (Fig. 1.3).

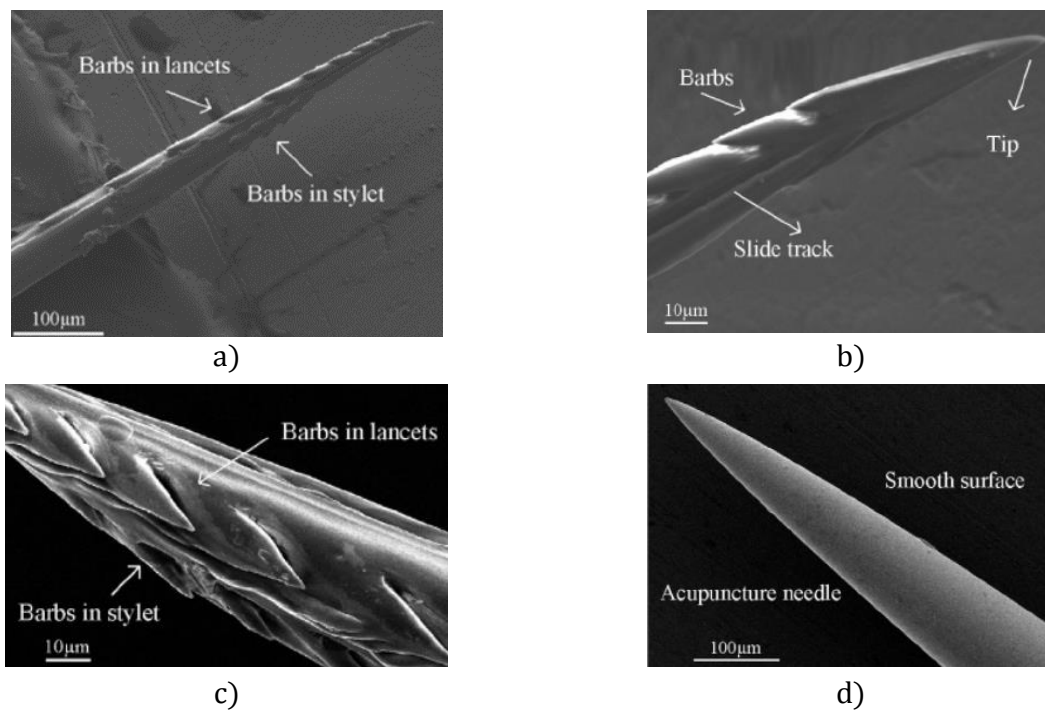


Figure 1.3. SEM images of a honeybee's stinger and of an acupuncture needle: (a) stinger, (b) stinger tip, (c) barbs on the stinger, (d) and acupuncture needle (Ling et al., 2017).

The results showed that the presence of the barbs on the stinger facilitates its easy penetration in the skin and strong adhesion during its removal.

The above-mentioned studies were also extended to a mosquito's proboscis, and several scientists explored its properties and tried to replicate it to obtain bioinspired microneedles (Jaiswal & Muthuswamy, 2015; Lenau et al., 2017; Ramasubramanian et al., 2008; Shoffstall et al., 2018). In fact, the mosquito proboscis is characterized by several micro-serrations, which are ultimately aimed to ease penetration and reduce nerve stimulation. Previous research was conducted to observe the geometry of its micro serrations. Izumi et al. (Izumi et al., 2011, 2008) have shown the effectiveness of the insertion of silicon microneedles inspired by the mosquito's proboscis into artificial skin.

Effects similar to the ones described above have also been observed with micro-needles created by MEMS techniques during insertion in the presence of vibrational motion (Izumi et al., 2011). Hollow micro-needles, made of silicon, were also fabricated by Oka et al. (Oka et al., 2002). The needles featured a jagged shape similar to that of a mosquito's maxilla and were capable of penetrating the surface of hard silicon rubber through standard insertion. Besides lithography and etching, three-dimensional laser lithography was also adopted to obtain microneedles inspired by the mosquito proboscis, but the process can be extremely expensive (Suzuki et al., 2018). Other researchers employed a similar technique to fabricate needles inspired by the honeybee's stinger (Sahlabadi & Hutapea, 2018), which resulted in a decrease in the penetration force by 46% in bovine liver tissue tests. Chen et al. investigated similar bioinspired needles by proposing a novel three dimensional additive manufacturing method (Chen et al., 2018). The presence of barbs on the microneedles enhances stress concentration at their location, which, in turn, determines the reduction of insertion and frictional forces.

Aoyagi et al. (Aoyagi et al., 2008, 2012) have proven the cutting efficiency of serrated profiles, also from a computational standpoint (Fig. 1.4). As shown in Fig. 1.4, the harpoon shape of the mosquito proboscis causes stress concentrations at many points, which eases its insertion into the skin.

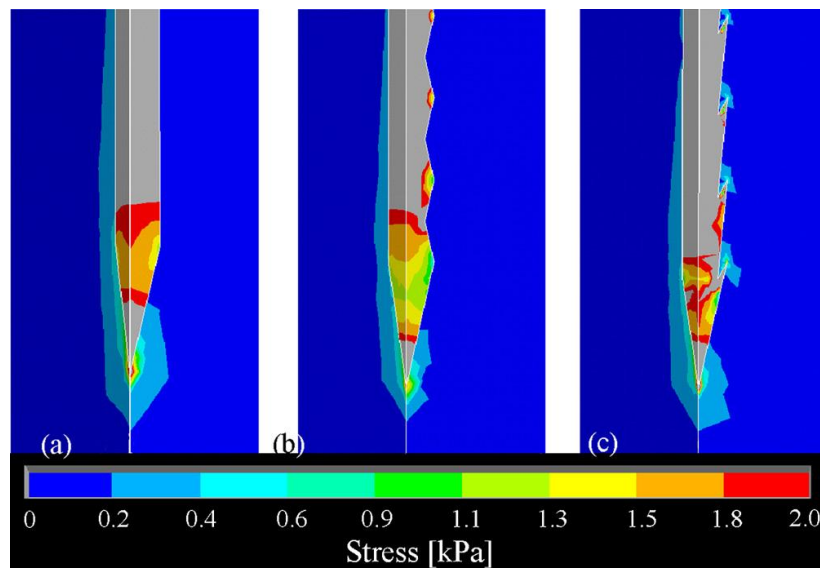


Figure 1.4. Effect of jagged shape on stress concentration (Aoyagi et al., 2008).

Kong et al. (Kong & Wu, 2009, 2010) have also performed a study on the prediction of the insertion force of the mosquito's fascicle from an experimental and computational standpoint. They identified the nanometer-sized tip radius of the mosquito's fascicle as one of the causes of its extremely low insertion force ($18 \mu\text{N}$). However, few research studies have been performed on the impact of micro-serrations—similar to those seen on the mosquito's proboscis—on insertion forces and their possible implementation on the cutting edge of medical devices, including knives, needles, and BPs.

1.3.3 Cutting motion

One of the critical aspects of the cutting process of soft tissue is represented by the relative motion of the cutting edge with respect to the reference target tissue that needs to be cut. Several researchers have focused their attention on this subject to provide a deeper understanding of the parameters and conditions that could lead to an optimal cutting motion. For instance, the effect of insertion velocity on the force has been studied by Heverly et al. and Hing et al. (Heverly et al., 2005; Hing et al., 2006). Their results show that higher insertion velocities lead to lower tissue deformation during cutting.

Atkins et al. (Atkins et al., 2004) investigated the effectiveness of a slicing motion on the cutting forces of a blade by using an energy-based fracture mechanics approach. They demonstrate that an increase in the slice/push ratio dramatically reduces the cutting forces. Also, Han et al. (Han & Ehmann, 2013a) researched tissue cutting mechanics and focused specifically on the application of efficient cutting motions for biopsy needles. They observed that the combination of rotational and translational motion has the potential to improve cutting performance.

Abolhassani et al. (Abolhassani et al., 2006a, 2007a, 2004, 2006b, 2007b) observed the impact of rotational motion on the needle's axial force. Meltsner et al. (Meltsner et al., 2007) performed similar studies on 18-gauge hollow cannulas for brachytherapy robots and observed that the needle's rotational motion leads to a reduction of insertion forces with a minimal increase in tissue damage. Furthermore, Wan et al. (Wan et al., 2005) noticed that rotating a brachytherapy cannula can lead to the minimization of the displacement error during its insertion. Badaan et al. (Badaan et al., 2011) have also explored the application of rotational motion to commercial needles of various sizes to improve lesion targeting (Fig. 1.5).

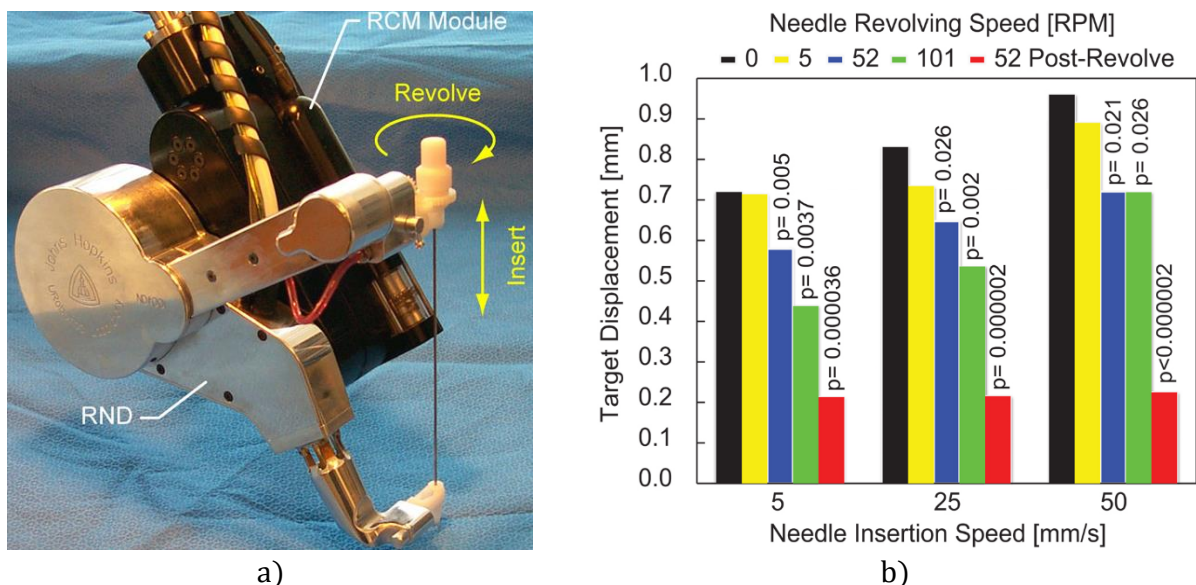


Figure 1.5. Rotating needles: (a) revolving needle driver supported by a Remote Center of Motion (RCM) orientation module and (b) target displacements with no-revolve, when rotating while inserting and after the insertion (post-revolve) (Badaan et al., 2011).

Very few research studies have focused on the development of new cutting motions that could further reduce the cutting force and address the need for efficient cutting in clinical environments. To successfully address this gap, inspiration from the mosquito's proboscis will be taken, as a mosquito's insertion is characterized by painless penetration and high targeting accuracy (Izumi et al., 2008; Kong et al., 2009). As observed by Aoyagi et al. and Izumi et al. (Aoyagi et al., 2008; Izumi et al., 2008), the mosquito's proboscis vibrations range between 1 to 30 Hz and provide a crucial contribution to tissue penetration along the jagged cutting edge (Fig. 1.6). In their work, Aoyagi et al. (Aoyagi et al., 2008) combined micro-needles like the mosquito's proboscis, which are composed of a central straight needle and two jagged outer ones. Cutting experiments with the fabricated micro-needles into artificial skin were carried out, and the effectiveness of vibrational motion in easing the insertion of jagged needles was confirmed.

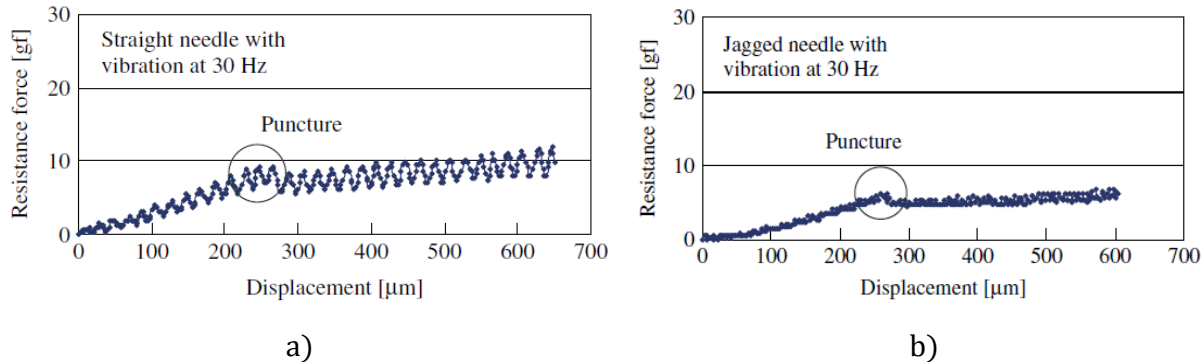


Figure 1.6. An example of resistance force detected by the load cell for insertion with (a) straight and (b) jagged microneedle at a vibration of 30 Hz (Izumi et al., 2008).

Begg et al. (Begg & Slocum, 2014) observed how the application of linear vibrational motions, with frequencies ranging from 50 to 500 Hz and amplitudes ranging from 0.1 to 3 mm, lead to a consistent decrease of the cutting forces in hypodermic needle insertion. Also, the application of ultrasonic devices, with frequencies ranging from 23 to 60 kHz and amplitudes ranging from 80 to 200 μm , lead to similar reductions in the axial force (Zucker Karl A., 2001). However, these ultrasonic devices can also cause more immediate tissue damage (Begg & Slocum, 2014). Vibrational motions were also adopted by marketed devices such as the “GentleSharp” (U.S. Patent No. 10219832, 2014), a blood sampling system for animal studies, which adds a low-frequency oscillatory motion to the axial needle motion to reduce the puncture force. Several researchers also investigated different techniques for performing needle insertion by actuated steerable cannulas for prostate biopsy and diagnostic procedures. Ayvali et al. implemented a multi-degrees of freedom actuated cannula to deliver diagnostic toolings, like a needle or surgical video camera (Ayvali et al., 2012). However, the cutting motion that is adopted during skin biopsy and procedures has not been analyzed.

1.4 Outline

According to the stated objectives, this thesis suggests a scientific approach for (i) the design of novel biopsy needle cutting edges and cutting motions, (ii) the development of manufacturing processes necessary for their realization, and (iii) their testing on phantom tissue. This thesis also provides analytical and computational models for the prediction and simulation of cutting forces during biopsy needle insertions.

In Chapter 2, analytical models related to the cutting angles of several needle tip designs will be defined and compared. Furthermore, several experimental cutting tests will be performed with different cannula tip designs to assess: (i) the optimal geometry for rotating insertion, and (ii) the benefits of rotational motions at different needle axial speeds and on different phantom materials.

Chapter 3 focuses on the development of mathematical models to compute the main cutting angles and fracture forces related to needle tips characterized by any three-dimensional (3D) surface. The proposed methodology will be applicable to virtually any needle geometry. The analytical results will be compared with the ones related to one-plane bevel needles, which represent the most common geometry adopted in clinical environments. Furthermore, a helical geometry will be designed, manufactured, and tested on phantom tissue for translational and rotational insertions.

Chapter 4 explores the characterization of phantom tissue by uniaxial compression and tension tests. Data coming from the tissue characterization were used to calibrate an analytical model, and the finite element method (FEM) models to predict the cutting force during the insertion of core biopsy needles. The phantom tissue was modeled as a hyperelastic material

using several constitutive models, and experimental tests were performed to assess the reliability of the proposed tissue characterization method.

Chapter 5 investigates the effects of micro-serrated cutting edges on soft tissue cutting by means of biopsy punches (BP). A setup for laser ablation of BP cutting edges will be implemented and micro-features manufactured on their cutting edges. Insertion tests will be performed with the aim of investigating the influence of BP micro-serrations on the cutting force. 3D finite element simulations will be performed regarding the deformation of hyperelastic soft tissue undergoing large deformations.

Finally, Chapter 6 presents the conclusions on the work that has been accomplished and outlines the future directions for the further development of this research.

2 Design and Cutting Motions of Rotating Needles

In this chapter, cutting motions used during bone marrow and breast biopsy procedures are analyzed in detail. During these procedures, a hollow needle is advanced to depths ranging from 20 to 80 mm to collect tissue samples for further analysis and diagnosis. The ultimate goal is to provide a series of guidelines for clinicians and surgeons to correctly choose the needle tip geometry and motion speeds for rotating insertions. First, the mathematical models related to the cutting parameters and forces of hollow needles with different needle tip geometries are explained and compared. Second, the experimental methods adopted during this research are introduced. They include the setups for (i) manufacturing and testing of hollow needles, and (ii) characterization of soft materials by means of uniaxial tests. Third, the performance of conical, bevel, and multi-plane needles is studied through penetration tests into phantom tissue. Finally, several tests at different axial and rotational speeds are performed on different phantom tissues. The results will identify the optimal geometry and motion parameters that lower the cutting forces to obtain larger biopsy samples (Moore et al., 2010). The findings of this research are applicable to bone marrow biopsy, breast biopsy, and several clinical settings where hollow needles or similar medical devices are used. This chapter is based on Giovannini et al. (Giovannini et al., 2018a).

2.1 Mathematical Models for Rotating Hollow Needles

In this section, different hollow needle (cannula) designs—including conical, one-plane bevel, and multi-plane bevel tip needles—will be explored. The tip geometry and cutting angle

computations for each needle will be described first, while their manufacturing process will be presented in Section 2.3.

2.1.1 Analytical Models for Conical and One-Plane Bevel Cannulas

The cannula tip geometry can be mainly described by two parameters: the included angle θ and the inclination angle λ (Han et al., 2012; Moore et al., 2010), which depend on the cannula's geometry. θ is defined as the angle between the rake face and the cylindrical side surface, while λ represents the angle between the vector \mathbf{t} tangent to the cutting edge and the xy -plane (Fig. 2.1). One-plane bevel cannulas are also characterized by the bevel angle (ξ), which is the angle at which the plane was ground, and it is equal to θ in conical cannulas (Fig. 2.1). According to previous studies (Han et al., 2012), it is desirable to have a small θ and large λ values to reduce the cutting force.

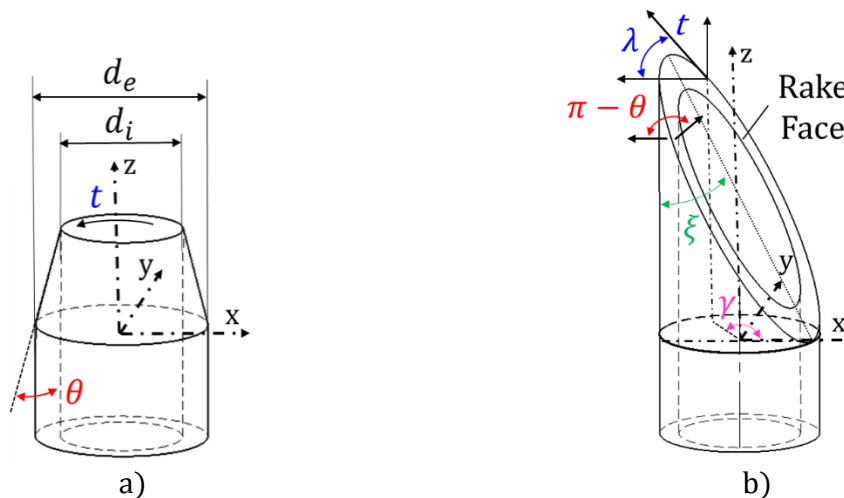


Figure 2.1. Illustration of needle geometries: (a) conical and (b) one-plane bevel cannula tip.

To define θ and λ , the angular position of a point on the cutting edge must be assigned by the angle γ (Fig. 2.1b). According to Han et al. (Han et al., 2012), θ and λ can be calculated from:

$$\theta(\gamma) = \pi - \arccos(\cos\xi\cos\gamma) \quad 0 < \xi \leq \frac{\pi}{2} \quad (2.1)$$

$$\lambda(\gamma) = \arcsin \frac{|\cot\xi\sin\gamma|}{\sqrt{1 + \cot^2\xi\sin^2\gamma}} \quad 0 < \xi \leq \frac{\pi}{2} \quad (2.2)$$

Figure 2.2 shows the comparison between conical and one-plane bevel cannulas with bevel angles (ξ) equal to 15°, 45° and 75°. Conical hollow cannulas have a constant included angle, while in one-plane bevel cannulas, both θ and λ vary with the cannula angle (γ) (Fig. 2.2). In this regard, one-plane bevel cannulas feature greater inclination angles (λ), than conical cannulas, which have a null λ since their cutting edge is perpendicular to the cannula axis. The presence of the bevel could potentially ease the penetration process, especially for one-plane bevel cannulas with bevel angles (ξ) equal to 15° and 45°, due to the consistent decrease of the needle cross-section for these bevel angles.

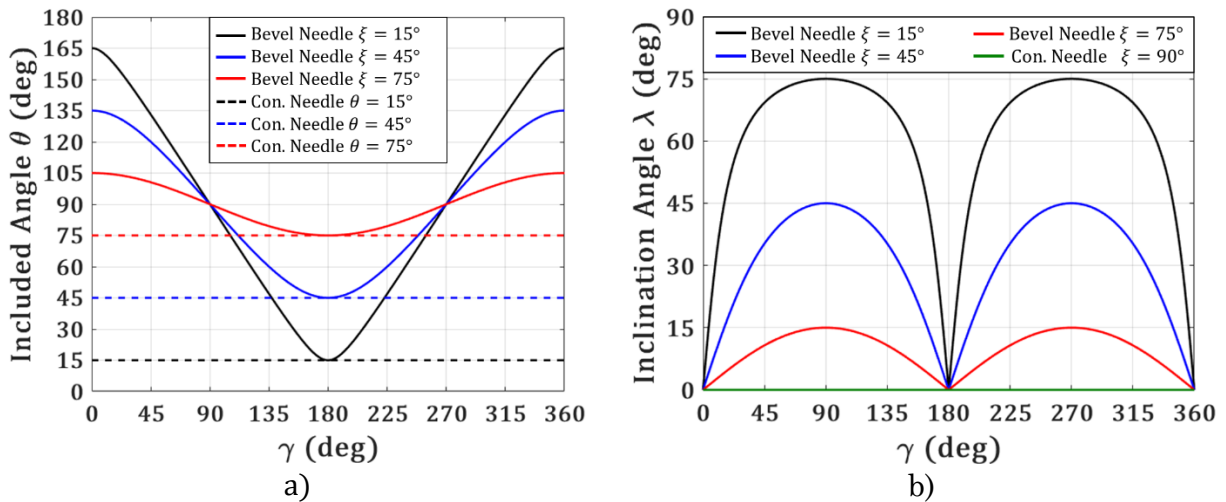


Figure 2.2. (a) Included angle θ and (b) inclination angle λ for conical bevel cannulas.

In this study, conical and one-plane bevel cannulas with ξ equal to 15° , 45° , and 75° will be manufactured and their cutting performance tested in Section 2.4.

2.1.2 Analytical Models for Symmetric Multi-Plane Cannulas

One-plane bevel cannulas seem to represent a viable solution for effectively cutting soft tissue, but they are characterized by an asymmetric design that could lead to higher forces during their rotating insertion (detailed in Section 2.4). For this reason, symmetric multi-plane tip designs will be proposed and analyzed here (Fig. 2.3).

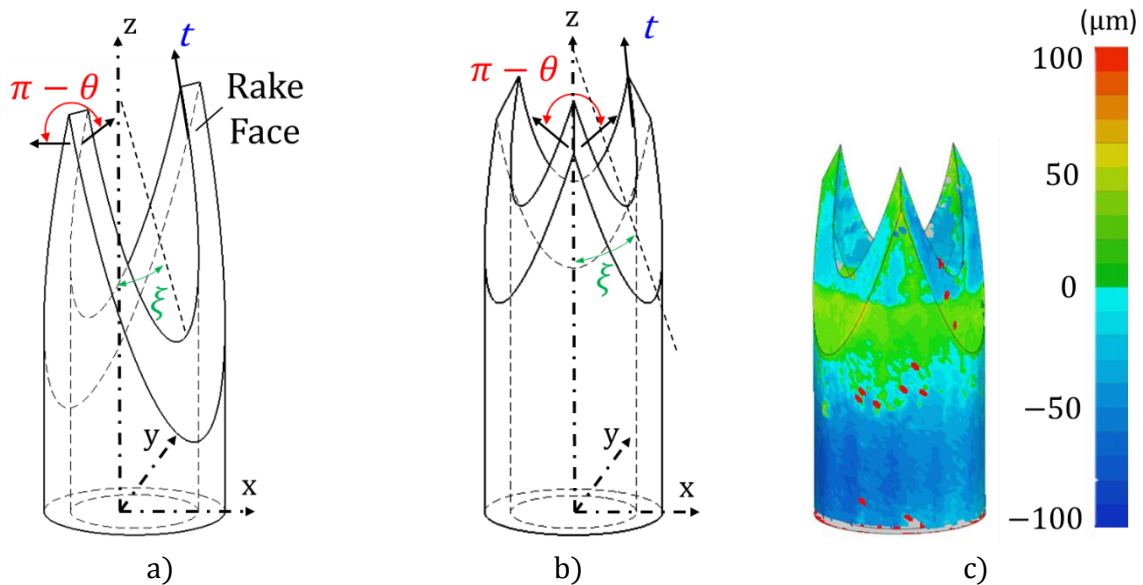


Figure 2.3. (a) Illustration of the tip geometry of two-plane, (b) three-plane bevel cannulas, and (c) its 3D scan after manufacturing, with the deviations with respect to the CAD model.

In multi-plane needles, the cutting edge is obtained by the intersection between two or more bevel planes. These cannulas are characterized by a constant bevel angle (ξ), which represents the angle between each of the planes and the cannula axis. The included angle (θ) is defined as

the angle between the cannula's cutting edges, while λ is defined in a manner identical to the one-plane bevel cannula. Multi-plane cannulas are also characterized by the angle ϕ , which is the rotation angle between consecutive bevel planes and is equal to $\phi = 2\pi/P_l$, where P_l represents the number of planes. According to Han et al. (Han, 2014), θ and λ for multi-plane cannulas can be obtained from:

$$\theta(\xi) = \pi - \arccos(\cos^2\xi\cos\phi + \sin^2\xi) \quad 0 < \xi \leq \frac{\pi}{2} \quad \phi = \frac{2\pi}{P_l} \quad (2.3)$$

$$\lambda(\gamma) = \arcsin \frac{|\cot\xi\sin\gamma|}{\sqrt{1 + \cot^2\xi\sin^2\gamma}} \quad 0 < \xi \leq \frac{\pi}{2} \quad -\frac{\pi}{P_l} < \gamma \leq \frac{\pi}{P_l} \quad (2.4)$$

Figure 2.4 illustrates the value of the included angle θ for cannulas with a different number of planes. A small bevel angle (ξ) leads to a small included angle (θ), and for a fixed value of ξ , the value of θ increases with the number of planes, P_l . When P_l is equal to 2, the minimal value of θ is reached and for $P_l > 3$, θ increases consistently making the geometry less efficient for cutting purposes (Fig. 2.4).

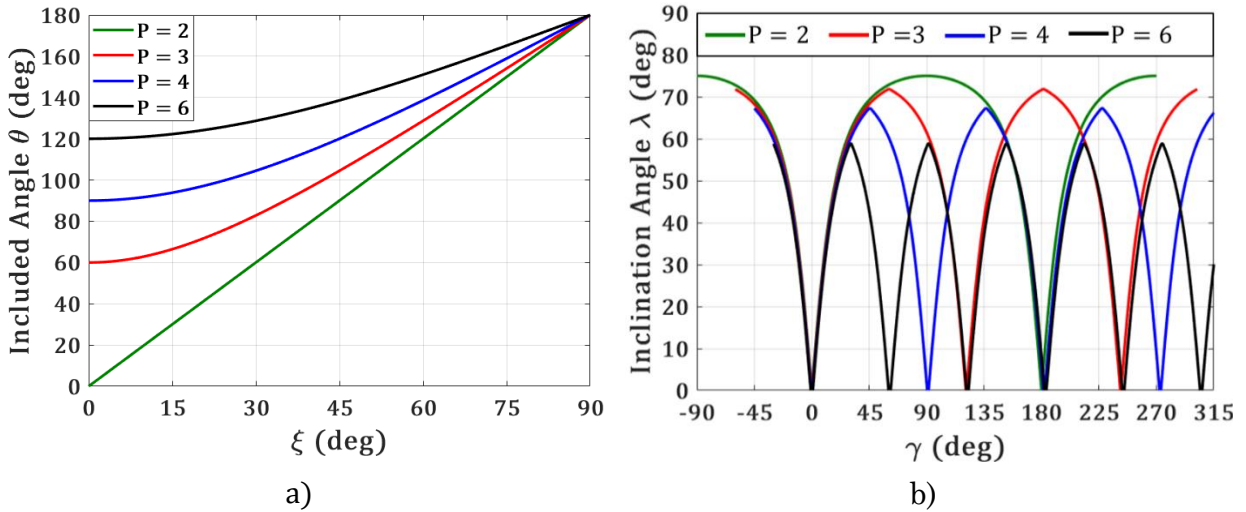


Figure 2.4. (a) Included angle θ and (b) inclination angle λ for multi-plane cannulas.

The inclination angle (λ) varies as a function of the cannula angle (γ), and its behavior is identical through the angle span related to each plane of the cannula (Eq. (2.4)). When P_l is equal to 2, the maximum value of λ is reached; greater values of P_l cause lower values of λ (Fig. 2.4) and, consequently, increase the axial cutting force (Han et al., 2012).

2.2 Analytical Models for Insertion Cutting Forces

During insertion, the hollow needle, or cannula, is pressed against the tissue at a steady speed, parallel to its longitudinal axis (v_a), while it is rotated in one direction (v_r). The cannula is acted upon by the axial cutting force (F_V), which is perpendicular to the cutting edge, and the cutting force (F_H), which is tangential to the cutting edge of the cannula (Fig. 2.5). Each of these two forces (F_V, F_H) have two components: (i) a rupture force, which determines the initial fracture of the tissue (F_{rup}), and (ii) a cutting force (F_{cut}), which is responsible for the crack growth in the tissue (Giovannini et al., 2018b).

$$F_V = F_{Vrup} + F_{Vcut} \quad (2.5)$$

$$F_H = F_{Hrup} + F_{Hcut} \quad (2.6)$$

Figure 2.5 shows the behavior of F_V and F_H during needle penetration. The tissue is first subjected to an elastic deformation until the first crack initiates at d_{rup} , (Phase I); then F_V increases until the peak force is reached, i.e., the rupture force (F_{Vrup} at d_{rup}). In Phase II, the needle is advancing into the soft tissue while it is steadily cutting it. F_V continues increasing to a maximal value, called the final force (F_{Vf}), until the cannula is stopped. These phases are also evident in the F_H profile (Fig. 2.5) and it is possible to identify the value of the fracture force

(F_{Hrup}) in the tangential direction by observing its value for a similar penetration depth that marks F_{Vrup} . In the next subsection, each force component will be analyzed in more detail.

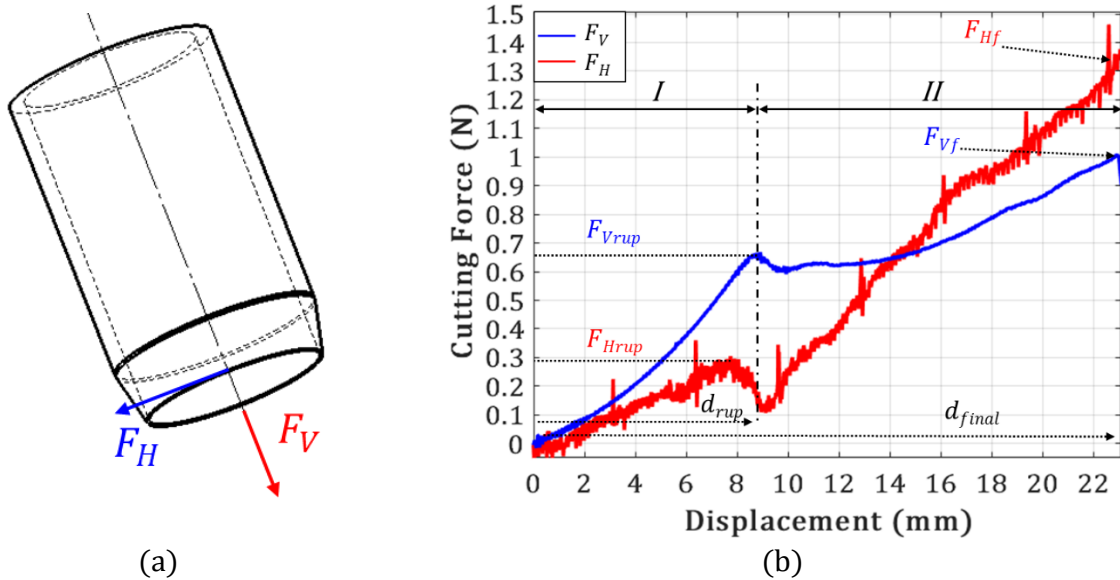


Figure 2.5. (a) 3D model of the cannula with cutting forces (F_V , F_H) and (b) their behavior during needle penetration highlighting the cutting phases (I, II), the rupture forces (F_{Vrup} , F_{Hrup}) and the final axial and tangential forces (F_{Vf} , F_{Hf}).

2.2.1 Fracture Force

According to Atkins et al. (Atkins et al., 2004), when the material being cut is not permanently deformed, the work performed by the cutting tool (W_N) is equal to the sum of the work needed to propagate the crack (W_C) and the work dissipated due to the friction between the material and the tool (W_F):

$$W_N = W_C + W_F \quad (2.7)$$

One can further develop each term of this equation (Atkins et al., 2004), where the work performed by the needle is equal to the sum of the work performed by the axial cutting force

(F_V) in the axial direction (d_v) and the work performed by the tangential force (F_H) in the tangential direction (d_h):

$$W_N = F_V dv + F_H dh \quad (2.8)$$

The work due to the propagation of the crack is calculated by (Atkins, 2009):

$$W_C = Rwdv \quad (2.9)$$

where R is the strain release rate and w is the tool contact length, which is equal to the internal circumference of the needle cutting edge ($w = \pi d_i = 2\pi r_{ni}$). The friction work (W_F) originated from the contact between the material and the tool, can be obtained from the product between the friction force (F_F) and the resultant displacement of the needle along the rake face (d_r), as shown in Fig. 2.6 (Atkins, 2009):

$$W_F = F_F dr \quad (2.10)$$

$$dr = \sqrt{\left(\frac{dv}{\cos(\theta)}\right)^2 + dh^2} \quad (2.11)$$

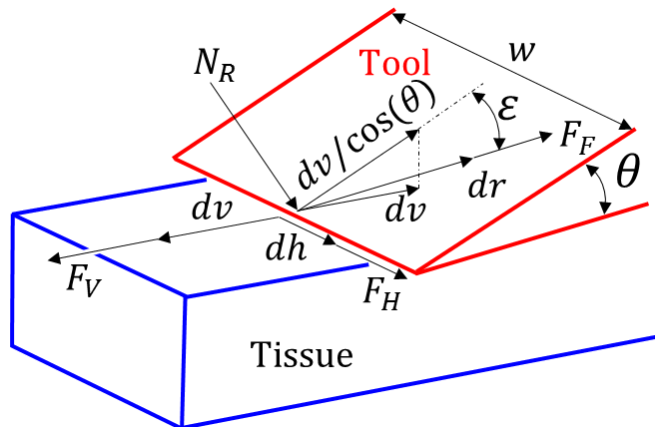


Figure 2.6. 3D model of the cutting edge during a slicing motion.

Since floppy offcuts are in contact with the needle, Coulomb friction is assumed, and the friction force is equal to $F_F = \mu_d N_R$, where N_R is equal to the contact force on the rake face of the needle and μ_d is the Coulomb dynamic friction coefficient. The equilibrium equation along the V direction can be written as (Fig. 2.7):

$$F_V = F_F \cos(\varepsilon) \cos(\theta) + N_R \sin(\theta) = N_R (\mu_d \cos(\varepsilon) \cos(\theta) + \sin(\theta)) \quad (2.12)$$

which leads to:

$$N_R = \frac{F_V}{(\mu_d \cos(\varepsilon) \cos(\theta) + \sin(\theta))} \quad (2.13)$$

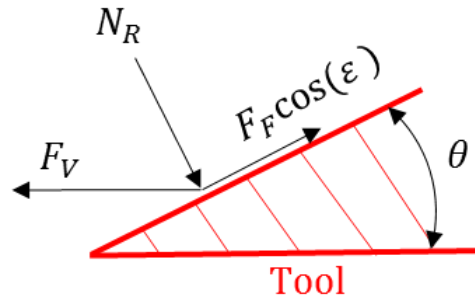


Figure 2.7. Free body diagram of the tool.

According to Fig. 2.6, the angle ε can be expressed as:

$$\varepsilon = \tan^{-1} \left(\frac{dh \cos(\theta)}{dv} \right) = \tan^{-1} (k \cos(\theta)) \quad (2.14)$$

where k represents the ratio between the displacements in the tangential and axial directions ($k = dh/dv$), which is also equal to the ratio between the speed parallel (v_{\parallel}) and perpendicular to the cutting edge (v_{\perp}). For conical needles, since their cutting edge is perpendicular to the needle axis, the speed parallel to the cutting edge (v_{\parallel}) is equal to the rotational speed (v_r); the speed perpendicular to the cutting edge (v_{\perp}) is equal to the axial speed (v_a). Consequently, the work balance can be written as:

$$F_V + F_H k = R w + \mu_d \frac{F_V}{(\mu_d \cos(\varepsilon) \cos(\theta) + \sin(\theta)) \cos(\theta)} \frac{1}{\sqrt{k^2 \cos^2(\theta) + 1}} \quad (2.15)$$

From Eq. (2.15), the fracture forces in the axial direction F_{Vrup} and in the tangential direction F_{Hrup} can be written as:

$$F_{Vrup} = F_V = \frac{R \pi d_i}{1 + k^2 - \frac{\mu_d \sqrt{(k \cos(\theta))^2 + 1}}{\cos(\theta) (\mu_d \cos(\varepsilon) \cos(\theta) + \sin(\theta))}} \quad (2.16)$$

$$F_{Hrup} = F_H = \frac{R \pi d_i k}{1 + k^2 - \frac{\mu_d \sqrt{(k \cos(\theta))^2 + 1}}{\cos(\theta) (\mu_d \cos(\varepsilon) \cos(\theta) + \sin(\theta))}} \quad (2.17)$$

This force model does not consider the impact of different needle tip geometries, which requires the development of finite element simulation models, but it describes the impact of the slice/push ratio (k), friction coefficient (μ_d) and strain energy release rate (R) on the fracture force (Fig. 2.8).

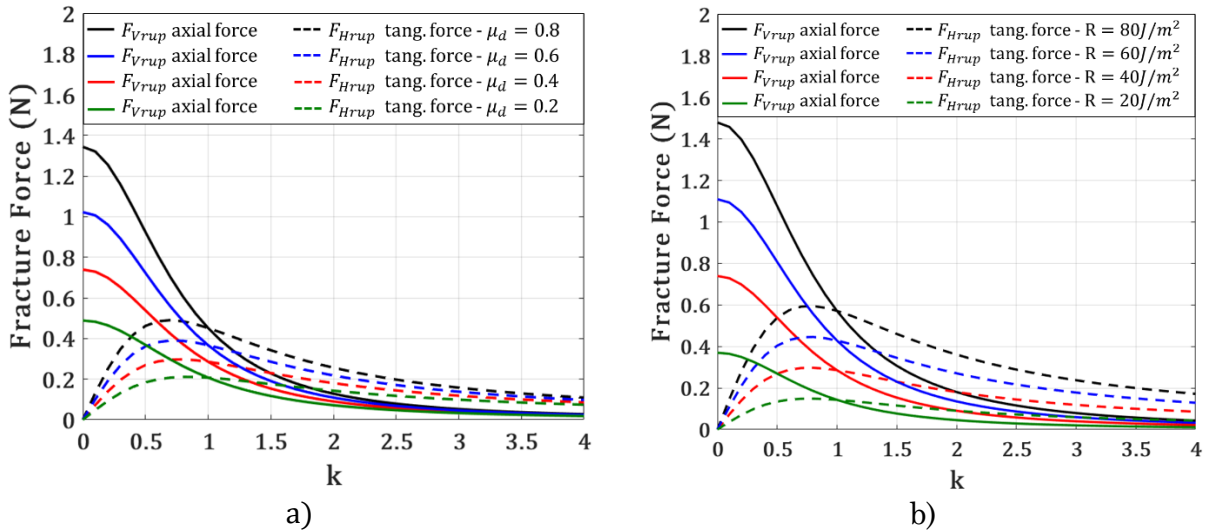


Figure 2.8. (a) Fracture forces (F_{Vrup} , F_{Hrup}) vs. different slice/push ratios, calculated for different friction coefficients (μ_d) and (b) different strain energy release rates, R .

The optimal slice push ratio is obtained from the intersection between the analytical curve referred to the fracture force in the axial direction (F_{Vrup}) and the one related to the fracture force in the tangential direction (F_{Hrup}). Higher friction coefficients (Fig. 2.8a) and tougher materials (Fig. 2.8b) lead to higher fracture forces, which, in turn, determine an increase of the optimal slice push ratio to cut the material.

2.2.2 Cutting Force

The cutting force (F_{Vcut}) is mostly composed of the friction force (Begg et al., 2014) and can be evaluated by the product of the coefficient of dynamic friction (μ_d) and the normal force applied to the inner and outer cannula surfaces. Begg et al. (Begg et al., 2014) evaluated the normal force (F_N) acting on the external surface of the needle by considering the pressure that the tissue is exerting in the radial direction as the needle is inserted. The formula to calculate F_N is derived from the interface pressure for a pin press-fit into a hole as (Slocum, 1992):

$$F_N = A_c \frac{E}{2(1+\eta)} = 2\pi(r_{ni} + r_{no})x \frac{E}{2(1+\eta)} = \frac{\pi(r_{ni} + r_{no})E}{(1+\eta)} x \quad (2.18)$$

where A_c represents the sum of the inner and outer areas of the cannula that are in contact with the tissue, r_e the outer radius of the cannula ($r_{no} = d_e/2$, Fig. 2.1a), x the cannula's displacement in the axial direction (x), E the Young's modulus of the tissue evaluated for a small strain, and η the Poisson ratio. The cutting force (F_{Vcut}) in the axial direction is given by (Begg et al., 2014):

$$F_{Vcut} = \mu_{da} F_N = \mu_{da} \frac{\pi(r_{ni} + r_{no})E}{(1+\eta)} x \quad (2.19)$$

where μ_{da} is the coefficient of dynamic friction in the axial direction and it is a function of the slice/push ratio k ($\mu_{da} = f(k)$). The friction force can also be expressed per unit of axial displacement by dividing Eq. (2.19) by x :

$$f_{Vcut} = \mu_{da} \frac{\pi(r_{ni} + r_{no})E}{(1 + \eta)} \quad (2.20)$$

By following the same approach (Eqs. (2.19)), it is possible to calculate the cutting force in the tangential direction (F_{Hcut}):

$$F_{Hcut} = \mu_{dr} \frac{\pi(r_{ni} + r_{no})E}{(1 + \eta)} x \quad (2.21)$$

where μ_{dr} is the dynamic friction coefficient in the rotational direction due to the contact between the cannula's surfaces and soft tissue. The overall axial cutting force (F_V) required to insert the cannula into the tissue is equal to (Begg et al., 2014; Han et al., 2013a):

$$F_V = \frac{2R\pi r_{ni}}{1 + k^2 - \frac{\mu_d \sqrt{(k \cos(\theta))^2 + 1}}{\cos(\theta) (\mu_d \cos(\varepsilon) \cos(\theta) + \sin(\theta))}} + \mu_{da} \frac{\pi(r_{ni} + r_{no})E}{(1 + \eta)} x \quad (2.22)$$

This analytical formulation assumes that the cannula is not deformed during tissue cutting. A similar approach can be adopted to calculate the force in the tangential direction, F_H , where the formulations of the fracture force (F_{Hrup}) and of the cutting force (F_{Hcut}) were shown respectively in Eq. (2.17) and Eq. (2.21), and can be added to obtain the overall tangential force, F_H :

$$F_H = \frac{2R\pi r_{ni} k}{1 + k^2 - \frac{\mu_d \sqrt{(k \cos(\theta))^2 + 1}}{\cos(\theta) (\mu_d \cos(\varepsilon) \cos(\theta) + \sin(\theta))}} + \mu_{dr} \frac{\pi(r_{ni} + r_{no})E}{(1 + \eta)} x \quad (2.23)$$

Further, during the application of the slicing motion, the friction force (F_F) (Eq. (2.10)), acts in the direction of the resulting displacement and can be expressed as the vector sum of its components (F_{FV}, F_{FH}):

$$F_F = \sqrt{F_{FV}^2 + F_{FH}^2} = \mu_d N_R \quad (2.24)$$

where the friction coefficient (μ_d) in Eq. (2.22) and Eq. (2.23), can be calculated as:

$$\mu_d = \sqrt{\mu_{da}^2 + \mu_{dr}^2} \quad (2.25)$$

By combining Eq. (2.25) with Eq. (2.23) and Eq. (2.22), the resultant axial (F_V) and tangential (F_H) cutting force required to insert the cannula into the tissue can be expressed as follow:

$$F_V = \frac{2R\pi r_{ni}}{1 + k^2 - \frac{\sqrt{\mu_{da}^2 + \mu_{dr}^2} \sqrt{(k \cos(\theta))^2 + 1}}{\cos(\theta) (\sqrt{\mu_{da}^2 + \mu_{dr}^2} \cos(\varepsilon) \cos(\theta) + \sin(\theta))}} + \mu_{da} \frac{\pi(r_{ni} + r_{no})E}{(1 + \eta)} x \quad (2.26)$$

$$F_H = \frac{2R\pi r_{ni} k}{1 + k^2 - \frac{\sqrt{\mu_{da}^2 + \mu_{dr}^2} \sqrt{(k \cos(\theta))^2 + 1}}{\cos(\theta) (\sqrt{\mu_{da}^2 + \mu_{dr}^2} \cos(\varepsilon) \cos(\theta) + \sin(\theta))}} + \mu_{dr} \frac{\pi(r_{ni} + r_{no})E}{(1 + \eta)} x \quad (2.27)$$

In Section 2.5.1, the analytical values of the fracture and cutting forces will be compared with experimental values. The axial (F_{Vcut}) and tangential cutting forces (F_{Hcut}) can be obtained by subtracting the rupture force from the value of F_V and F_H at the final penetration depth (Fig. 2.5). These values can be expressed per unit displacement (f_{Vcut}) and they are adopted as the metrics to assess needle performance with different designs in cutting soft tissue after initial fracture, i.e.:

$$F_{Vcut} = F_{Vf} - F_{Vrup} \quad (2.28)$$

$$f_{Vcut} = \frac{F_{Vf} - F_{Vrup}}{d_{final} - d_{rup}} \quad (2.29)$$

2.3 Experimental Methods for Rotating Needles

In this section, the experimental methods used in this study are introduced. They include the setups for (i) needle grinding, and (ii) cutting test on phantom tissue.

2.3.1 Needle Grinding Process

Hollow needles with different tip configurations were manufactured using 14-gauge cannulas that are very common in the clinical environment, and are characterized by an external diameter (d_e) of 2.108 mm and an internal diameter (d_i) of 1.6 mm (Fig. 2.1). Section 2.3.1.1 will introduce a kinematic description of the needle grinding processes, while Section 2.3.1.2 will present the grinding machine components.

2.3.1.1 Coordinate systems and kinematics in needle grinding

During the manufacturing process, the desired geometry is generated from the relative motion of the grinding wheel and the needle tip. Two coordinate systems are defined to describe the process. They are located respectively at the needle tip and at the grinding wheel surface. Figure 2.9 shows the position of the coordinate systems.

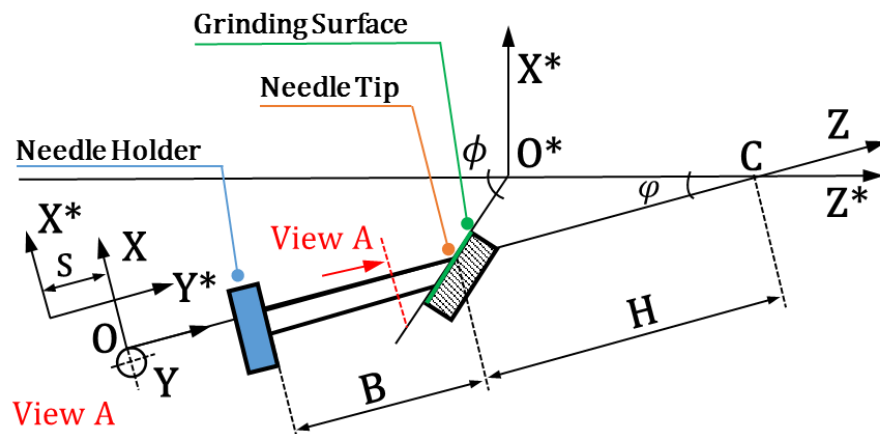


Figure 2.9. Geometric schematics with coordinate systems of the needle grinding process.

The Z^* axis represents the spindle axis and describes the rotation of the needle tip axis Z . The intersection between the Z^* axis and the grinding wheel surface coincides with the origin O^* ,

while the Y^* axis direction is obtained by the right-hand rule. The coordinate system OXYZ is assigned to the needle tip (Fig. 2.9), where the Z axis represents the needle axis, the Y axis is parallel to the Y^* axis, and the X axis is obtained by the right-hand rule.

During the grinding operations, the needle progressively translates towards the grinding wheel along a direction parallel to the Z^* axis, while it is rotating around the Z axis to obtain a conical tip geometry. The surface generated by the relative motion of the needle can be expressed in $O^*X^*Y^*Z^*$ as (Che et al., 2012; Lin et al., 1995):

$$Z^* = -\frac{\sqrt{X^{*2} + Y^{*2}}}{\tan(\phi_g)} \quad (2.30)$$

The coordinate system OXYZ is obtained from $O^*X^*Y^*Z^*$ by applying the transformation (Che et al., 2012):

$$\begin{bmatrix} X^* \\ Y^* \\ Z^* \\ 1 \end{bmatrix} = \begin{bmatrix} \cos\varphi & 0 & \sin\varphi & X_0^* \\ 0 & 1 & 0 & Y_0^* \\ -\sin\varphi & 0 & \cos\varphi & Z_0^* \\ 0 & 0 & 0 & 1 \end{bmatrix} \begin{bmatrix} X \\ Y \\ Z \\ 1 \end{bmatrix} \quad (2.31)$$

where:

$$X_0^* = -H\sin\varphi \quad (2.32)$$

$$Y_0^* = 0 \quad (2.33)$$

$$Z_0^* = \frac{X_0^*}{\tan(\phi_g)} \quad (2.34)$$

This transformation allows the expression of Eq. (2.30) in OXYZ coordinates, which shows the surface generated by the relative motion of the needle. This operation yields the following function (F_{surf}) which represents the surface of a conical needle tip:

$$F_{surf} = -X\sin\varphi + Z\cos\varphi + \frac{\sqrt{(X\cos\varphi + Z\sin\varphi - H\sin\varphi)^2 + Y^2} - H\sin\varphi}{\tan\phi_g} = 0 \quad (2.35)$$

For $Y = 0$, the conical surface turns into a single plane describing a one-bevel plane:

$$X(\cos\varphi - \sin\varphi\tan\phi_g) + Z(\cos\varphi\tan\phi_g + \sin\varphi) - 2H\sin\varphi = 0 \quad (2.36)$$

The bevel angle ξ (Fig. 2.1), which is adopted to describe one-plane bevel tip geometries, can be calculated as:

$$\xi = \phi_g - \varphi \quad (2.37)$$

Equation (2.36) is also applicable for describing multi-plane geometries, where the angle ϕ identifies the different planes that will be ground. The distance H can be expressed as a function of the distance OC and the angles φ and ϕ_g (Fig. 2.9) as:

$$H = OC(\cos\varphi + \sin\varphi\tan(90^\circ - \phi_g + \varphi)) \quad (2.38)$$

These equations allow the determination of the kinematic relationships between the X, Y, and Z axes, which are used to control the machine as it will be explained in the following section.

2.3.1.2 Five-axis needle grinding machine

A 5-axis grinding machine system (Che et al., 2012; Lin et al., 1995) was adopted to generate needles with different tip designs. This machine allows the rotation of the grinding wheel axis (r_5) to generate needle tips characterized by different cutting angles and to move the needle in two translational directions (t_1 and t_2) and two rotational directions (r_3, r_4). As described in Section 2.3.1.1, the Z axis coincides with the needle axis, while the X axis is parallel to the motion axis, t_2 . The position of the needle tip along the Z axis is controlled by the motion axis t_1 . The Y axis is perpendicular to X and Z axes, and it is described by the rotation of the needle (r_3) around the Z* axis (Fig. 2.10b).

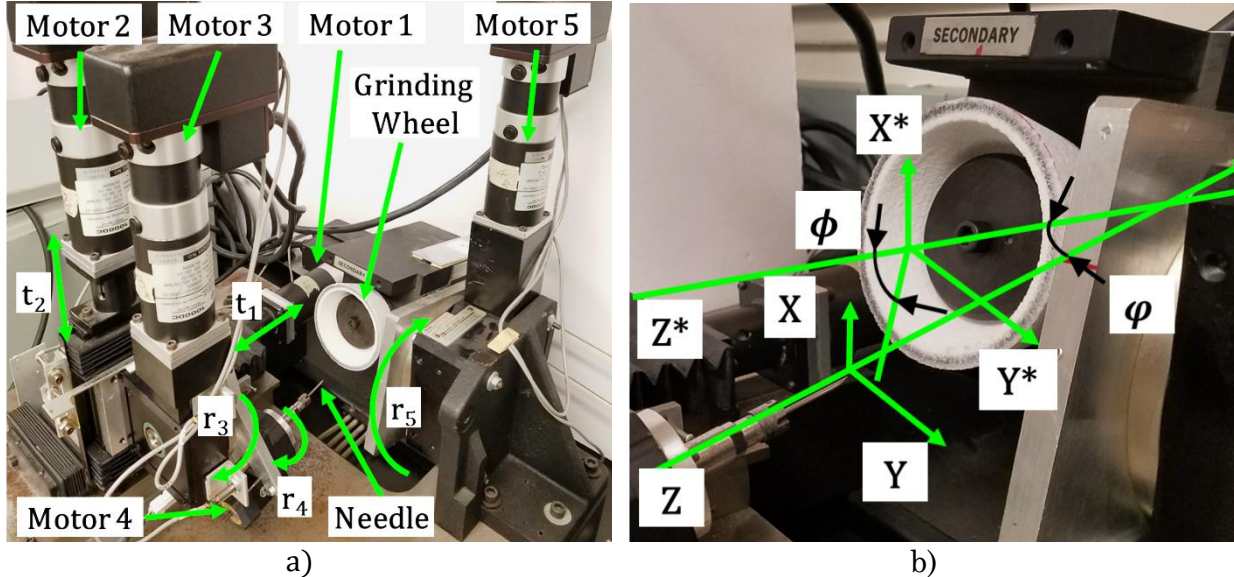


Figure 2.10. (a) Grinding machine system and (b) the schematics of the main axes.

During these grinding operations, r_3 is equal to zero and, therefore, the needle does not move along the Y^* axis. The acute angle between the grinding wheel surface plane and the Z^* axis ϕ , can be controlled by the motion r_5 , while the rotation of the needle around its axis, Z , can be controlled by the stepper motor acting on the rotational direction r_4 . The acute angle between the Z and Z^* axes (ϕ) is constant due to the machine set up and is equal to 10 degrees.

A straight cup grinding wheel (100 mm diameter, 33 mm thickness, 8 mm rim thickness and 10 mm back thickness, made of ceramic material) was used for the grinding operations. The needles were mounted in an ER8 collet, which is placed on a shaft connected to the stepper motor. During the grinding operations of one-plane and multi-plane bevel needles, the needle was kept in place by the stepper motor, and it was not rotating. However, during the grinding operations of conical needle tips, the cannula was rotated at 1,000 rpm. During machining, the needle was moving towards the grinding wheel at feed rates ranging from 0.02 to 0.5 mm/s.

2.3.2 Insertion Testbed

Cutting tests were performed on a custom-built testbed (Han et al, 2013a) with the goal of evaluating the cutting forces during the penetration of needles into soft tissue. The testbed is composed of a linear motor module, a stepper motor, a needle fixture, a three-component piezoelectric force dynamometer, a torque sensor, and a controller (Fig. 2.11).

The Copley linear motor module is responsible for the linear insertion. It has a resolution of 12 μm , and it can reach a maximal velocity of 10 m/s with a peak acceleration of 222 m/s^2 . A stepper motor (Model: HT17-268, Applied Motion Products) with a 1.8 $^\circ$ step angle and a holding torque of 0.16 Nm is used to impart the rotational motion of the needle. The linear motor is controlled by a Copley Xenus digital drive (Model: XTL-230-18-S), while the stepper motor is controlled by a step motor drive (Model: STR2, Applied Motion Products).

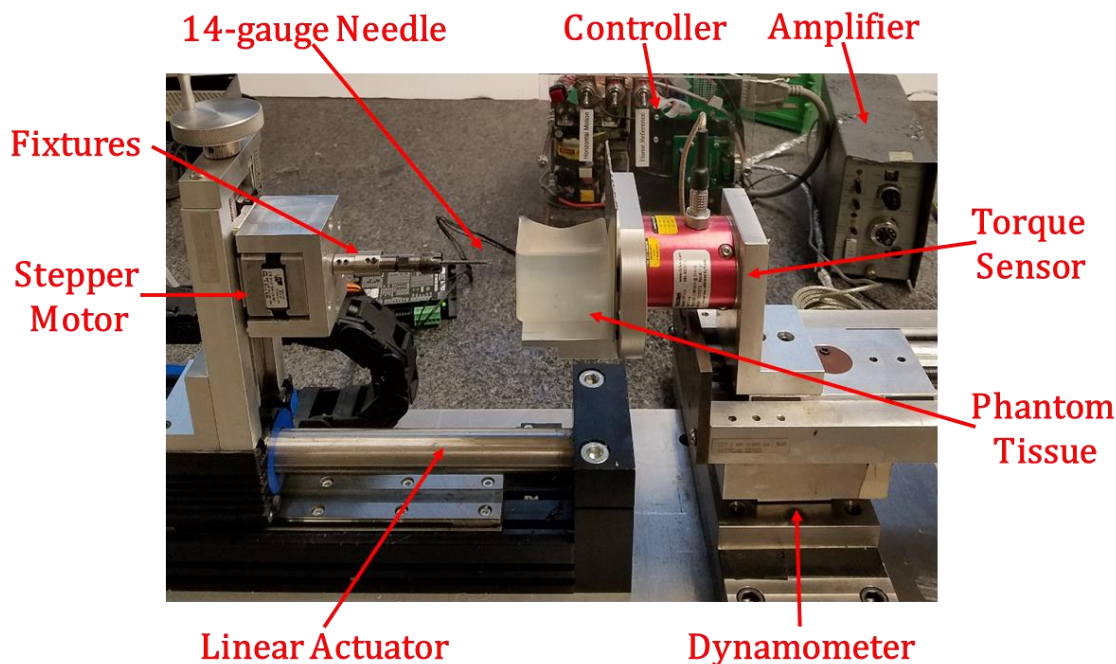


Figure 2.11. Testbed for the measurement of cutting forces and torques.

A customized fixture is used to attach the cannula to the shaft of the stepper motor. The fixture is composed of steel support in which a shank collet holder accommodates an ER8 collet for clamping the needle. Cutting forces are measured by a Kistler 9067 3-component piezoelectric dynamometer with a threshold of 0.01 N. Torque measurements are obtained by a torque sensor (FUTEK TFF425), capable of measuring a maximal torque of 0.1412 Nm with an output of 2.188 mV/V. Before each insertion, the radial runout of the needle was verified with a dial indicator and corrected to be limited to 20 μm or less. Both the sensors and actuators are placed on a granite table, but on different bases so that the vibrations induced by the linear actuator and the stepper motor will not affect the force measurements.

All the data was recorded with a NI Data acquisition board DAQ Card - 6036E at a 1,000 Hz sampling rate and then processed using LabView programs. The signal measurements from each experiment are filtered and post-processed in MATLAB after passing them through a low pass filter with a stop band of 50 Hz. The phantom tissue samples are placed on an aluminum plate which is affixed to the torque sensor.

2.3.3 Phantom Tissue

The experimental results in this thesis are based on cutting tests performed on phantom tissue, commonly utilized in several medical investigations (Podder et al., 2005b) for its homogeneity and consistency. The phantom tissue was made of Polymerizing Vinyl Chloride (PVC) mixture composed of 8116SS plastic (*P*) with 4116S plastic softener (*S*) (M-F Manufacturing, Texas) in a ratio S/P equal to 0, 0.25, 0.5, 1. However, PVC does not have fluid inside that leads to greater friction forces during needle penetration in comparison to insertions performed in biological tissue. To make the PVC material more realistic, a lubricating agent was

added into the PVC sample to simulate the interstitial fluids of the tissue as suggested by Wang et al. and Li et al. (Li et al., 2015; Wang et al., 2014). In this study, white mineral oil (Swan Mineral Oil, Smyrna, TN) was added in the amount of 5% with respect to the overall mixture. The tissue was then heated to 180°C and poured into a mold to obtain phantom blocks. By following this procedure, four different phantom materials were prepared (Table 2.1). Each phantom material is characterized by different properties since bone marrow tissue has an effective Young's modulus that ranges from 0.25 to 24.7 kPa (Jansen et al., 2015), while breast tissues are characterized by Young's modulus ranging from 7.5 to 66 kPa (Gefen & Dilmoney, 2007). The characterization of phantom tissue will be described in detail in Chapter 4, where the definition of the constitutive equations will be essential for the elaboration of the computational model.

Table 2.1. Young's modulus for each phantom tissue characterized by a different softener/plastic ratio (S/P).

Ratio S/P	Young's Modulus (kPa)
0	32.96
0.25	20.30
0.5	13.60
1	4.88

2.4 Impact of Different Needle Tips on Cutting Forces

In this section, several 14-gauge needles with different tip designs were generated (Section 2.1) and tested on phantom tissue composed of 8116SS plastic with 4116S plastic softener in a ratio S/P equal to 0.25, which was described in Section 2.3.3.

Each needle was inserted six times into the target tissue to a penetration depth of 23 mm. During the insertion process, the needles were steadily rotated counterclockwise as during

typical clinical procedures. The rotational (v_r) and translational speeds (v_t) were set respectively to 2 mm/s and 1 mm/s through all the tests. The analysis of the cutting forces for the conical and one-plane bevel needles will be presented in Section 2.4.1, while Section 2.4.2 will show a similar analysis for multi-plane needles.

2.4.1 Needle Tip Effect on Conical and One-Plane Bevel Needles

Insertions with conical needles and one-plane bevel needles with different included angles (θ) equal to 15°, 45°, 75°, and 90° were performed to observe the impact of different tip geometries. Needles with $\theta = 90^\circ$, will be referred to as cylindrical needles (cyl.) in the figures that follow (Fig. 2.12 and 2.13). All the tests were run according to the specifics provided in the introduction of Section 2.4. By comparing the values of the rupture forces (F_{Vrup} , F_{Hrup}) and cutting forces (f_{Vcut} , f_{Hcut}), it is apparent that the needle tip design has a crucial role in the penetration of the cannula into soft tissue.

Figure 2.12 shows that conical needles with smaller included angles tend to lead to smaller axial fracture forces. The same behavior was also observed for one-plane bevel needles. In addition, insertions performed with one plane-bevel needles result in lower axial fracture forces than insertions executed with conical needles with the same included angle θ (Fig. 2.12a). For instance, one-plane bevel needles with θ equal to 15° generate an axial fracture force that is 47.4% lower than the axial force measured during conical needle insertion (Fig. 2.12a). On the contrary, the tangential fracture force observed during conical and one-plane bevel needle insertions tends to have higher values with respect to the value measured for cylindrical needle insertion.

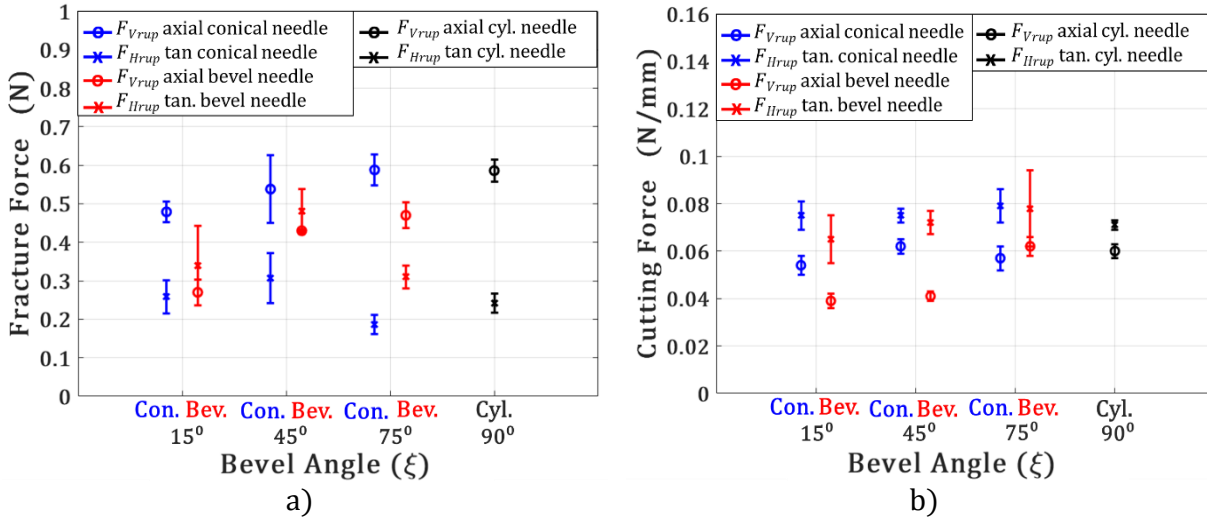


Figure 2.12. (a) Fracture (F_{Vrup} , F_{Hrup}) and (b) cutting force values (F_{Vcut} , F_{Hcut}) for cylindrical ($\theta = 90^\circ$), conical and one-plane bevel needles ($\theta = 15^\circ, 45^\circ, 75^\circ$).

Figure 2.12b illustrates the value of the cutting forces per unit displacement in both axial (F_{Vcut}), and tangential directions (F_{Hcut}). The experimental values of the cutting forces for bevel needles are similar to the values observed for the conical needles, except for the one-plane bevel needles with θ equal to 15° and 45° , which exhibit lower cutting forces in the axial direction.

This result suggests that the force necessary for cutting the tissue after initial rupture is less dependent on the needle tip geometry, which mostly affects the fracture forces.

To confirm that insertion forces are dependent on the needle geometry, an unpaired two-tailed test was developed to compare the value of the axial and tangential forces (Tables 2.2 and 2.3) for cylindrical ($\theta = 90^\circ$) and conical/bevel needle insertions at the maximum penetration depth (F_{Vf} , F_{Hf}) (Fig. 2.5b). The test was not applied to the fracture (F_{rup}) and cutting forces (F_{cut}), since their identification across all the experimental data can be subject to interpretation (Fig. 2.5). The test assumes unequal variances between samples and was run with a significance level (α) equal to 0.05. Table 2.2 presents the test outcomes for the best performing needle tip

configurations, which are compared to a cylindrical needle. For instance, for the one-plane bevel needle, the axial force ($\mu = 0.584 \text{ N}$, $\sigma = 0.040$) is 36.21% lower (p-value = 1.52×10^{-7}) than the axial force measured with a cylindrical needle ($\mu = 0.915$, $\sigma = 0.041$). The presence of conical and one-plane bevel tips leads to lower axial fracture forces (Fig. 2.13a) and consequently higher variations of ΔF_{Vf} in the axial force ($\Delta F_{Vf} = \frac{F_{Vf\text{bevel}} - F_{Vf\text{cyl}}}{F_{Vf\text{cyl}}} 100\%$) at the maximum penetration depth. This behavior is probably determined by the concentration of the insertion force on a smaller contact area, which leads to tissue fracture at a lower value of the axial force.

Table 2.2. The mean value (μ), standard deviation (σ), p-value, t-test result, and force variation (ΔF_{Vf}) related to the value of the force in the axial direction at the maximum penetration depth for cylindrical (cyl.), conical (con.), one-plane (bev.) and two- and three-plane needles.

Needle	μ	σ	p-Value	Result	$\Delta F_{Vf}(\%)$
Cyl. ($\theta = 90^\circ$)	0.915	0.041	-	-	-
Con. ($\theta = 15^\circ$)	0.825	0.054	0.0166	PASSED	-9.83
Bev. ($\theta = 15^\circ$)	0.584	0.040	1.52×10^{-7}	PASSED	-36.21
Bev. ($\theta = 45^\circ$)	0.629	0.027	4.08×10^{-7}	PASSED	-31.25
Two-Plane	0.591	0.020	1.05×10^{-6}	PASSED	-35.45
Three-Plane	0.704	0.048	2.29×10^{-5}	PASSED	-23.07

Table 2.3 confirms that the values of the tangential force observed during conical and one-plane bevel needle insertions at the maximum penetration depth present similar values as insertions performed with a cylindrical needle. In fact, the values of the force variation in the tangential direction are quite limited ($-12.61\% < \Delta F_{Hf} < -9.22\%$) and for a bevel needle with $\theta = 45^\circ$, it was not possible to assess from the t-test whether its tangential force (F_{Vf}) is higher or lower than the tangential force measured for a cylindrical needle.

Table 2.3. The mean value (μ), standard deviation (σ), p-value, t-test result, and force variation (ΔF_{Hf}) related to the value of the force in the tangential direction at the maximum penetration depth for cylindrical (cyl.), conical (con.), one-plane (bev.) and two- and three-plane needles.

Needle	μ	σ	p-Value	Result	ΔF_{Hf} (%)
Cyl. ($\theta = 90^\circ$)	1.285	0.184	-	-	-
Con. ($\theta = 15^\circ$)	1.122	0.089	0.1198	PASSED	-12.61
Bev. ($\theta = 15^\circ$)	1.167	0.024	0.2125	PASSED	-9.22
Bev. ($\theta = 45^\circ$)	1.291	0.122	0.9564	NOT PASSED	-0.43
Two-Plane	1.659	0.087	0.0046	NOT PASSED	+29.02
Three-Plane	1.549	0.082	0.0228	NOT PASSED	+20.47

According to the preceding analysis, needle tip geometry mostly affects the axial fracture forces. Insertions performed with one-plane bevel needles with θ equal to 15° and 45° are characterized by the lowest axial forces (Fig. 2.13), and a slight reduction in the value of the final tangential force (Table 2.3). However, one-plane bevel needles are characterized by an asymmetric tip geometry, which causes several oscillations in the tangential force behavior (F_H), especially for θ equal to 15° (Fig. 2.13b).

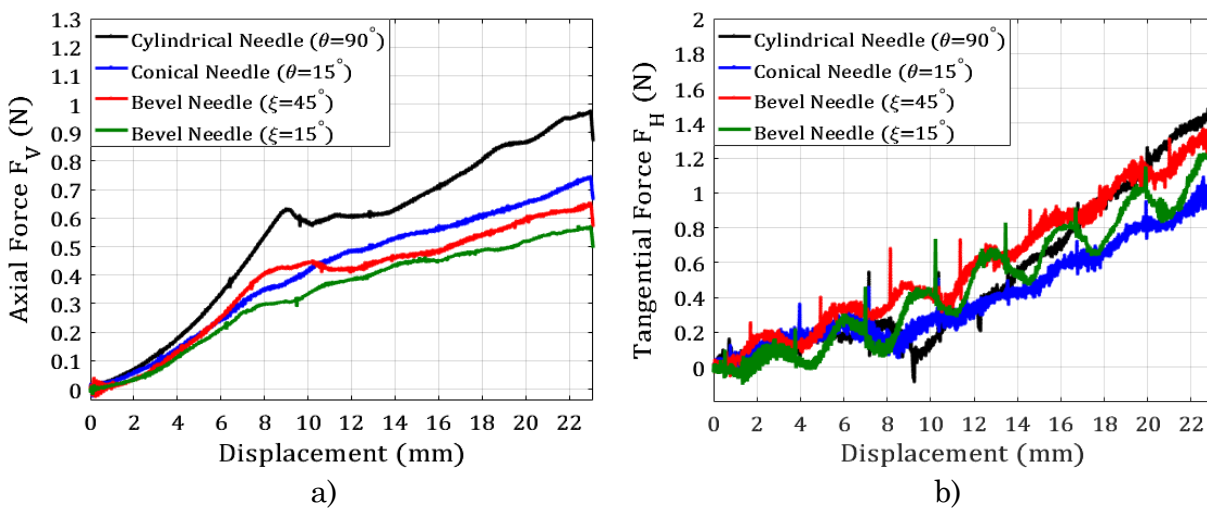


Figure 2.13. (a) Axial force (F_V) and (b) tangential force (F_H) during needle penetration for cylindrical ($\theta = 90^\circ$), conical ($\theta = 15^\circ$) and one-plane bevel needles ($\theta = 15^\circ, 45^\circ, 75^\circ$).

With the purpose of improving the behavior of one-plane bevel needles, symmetric multi-plane needles (Section 2.1.2) were designed, manufactured, and tested. The results will be shown in Section 2.4.2.

2.4.2 Needle Tip Effect in Symmetric Multi-Plane Needles

Symmetric needle tip geometries with an included angle θ of 15° and two- and three-plane bevel needles were studied and compared to cylindrical needles, which are characterized by an infinite number of planes. The goal was to investigate multi-plane geometries and their impact on rupture (F_{Vrup} , F_{Hrup}) and cutting forces (f_{Vcut} , f_{Hcut}).

Figure 2.14 shows that the values of the axial fracture force are higher in insertions performed with multi-plane needles rather than in insertions executed with a one-plane bevel needle. However, the force reduction ΔF_{Vf} for multi-plane bevel needles is consistent (Table 2.3).

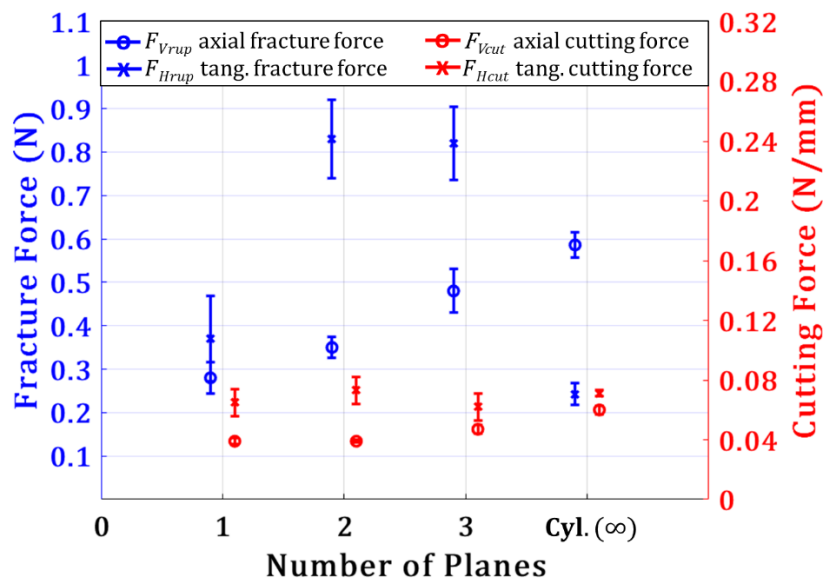


Figure 2.14. Fracture (F_{Vrup} , F_{Hrup}) and cutting force values (f_{Vcut} , f_{Hcut}) for needles with one, two, three, and infinite (cylindrical) number of planes.

or a two-plane bevel needle, the axial force ($\mu = 0.591, \sigma = 0.020$) is 35.45% lower (p-value = 1.05×10^{-6}) than the axial force measured for a cylindrical needle ($\mu = 0.915, \sigma = 0.041$). Tangential forces observed during multi-plane bevel needle insertions have higher values in comparison to the same type of forces measured for the one-plane bevel needle (Fig. 2.14, Table 2.3). However, it was not possible to assess from the t-test whether the tangential force for multi-plane needles is higher or lower than the tangential force for a cylindrical needle (Table 2.3).

Figure 2.15b shows how the values of the tangential force reached by the one-plane bevel needles are lower than the respective force values reached by multi-plane needles. However, multi-plane needle insertions do not present the fluctuations typical of one-plan bevel needle penetrations (Fig. 2.13b), and they are still effective in reducing the axial force (Fig. 2.15a). For these reasons, two and three-plane bevel needles represent the best needle geometries to lower the cutting forces during soft tissue cutting.

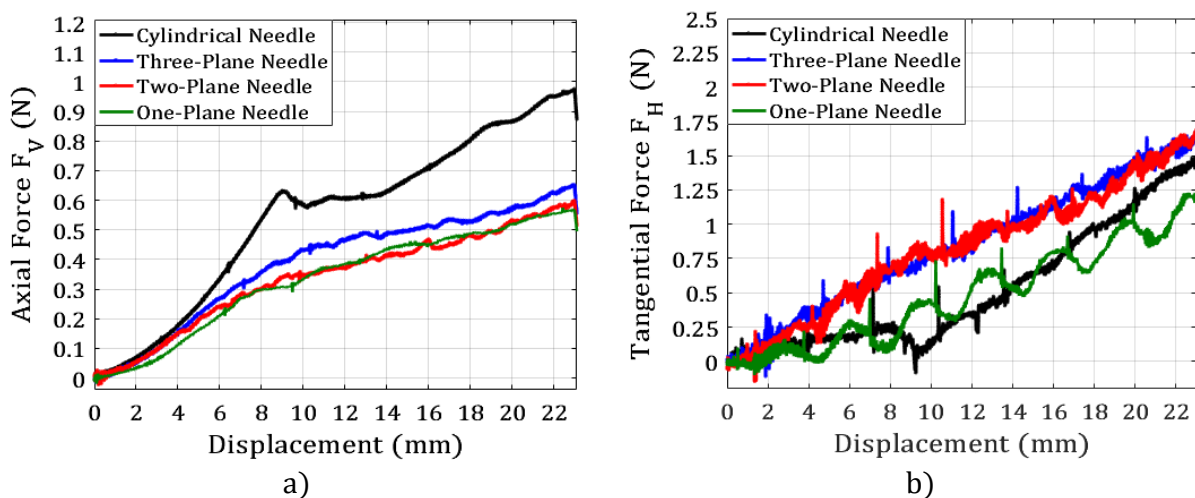


Figure 2.15. (a) Axial force (F_V) and (b) tangential force (F_H) behavior during needle penetration for cylindrical, one-plane, and multi-plane bevel needles ($\theta = 15^\circ$).

2.5 Impact of Different Cutting Motions on Cutting Forces

In this section, the impact of the rotational motion on the cutting forces is investigated. In Section 2.5.1, the effect of the slice push/ratio (k) on the cutting forces will be analyzed and the results will be compared with the force values obtained from the analytical models described in Section 2.2. In Sections 2.5.2 and 2.5.3, additional experimental cutting tests will be described in order to identify the optimal slice/push ratio for different needle axial speeds (Section 2.5.2) and different materials (Section 2.5.3). In all the tests, the 14-gauge cannula will be inserted 23 mm into the target phantom tissue while it was steadily rotated counterclockwise.

2.5.1 Impact of the Slice/Push Ratio on Cutting Forces

The first objective was to study the impact of the slice/push ratio on the fracture and cutting forces during needle insertion. To this end, a conical needle with an included angle θ of 15° was used; the translational speed (v_t) was set to 1 mm/s and the slice/push ratios ($k = v_r/v_t$), were set to 0, 0.25, 0.5, 1, 1.5, 2, 3 and 4. The cannula was inserted five times for each scenario for a total of 40 insertions into phantom tissue. This tissue was composed of 8116SS plastic with 4116S plastic softener in a ratio S/P equal to 0.5, as described in Section 2.3.3. For each insertion, the values of the rupture force component for both axial (F_{Vrup}) and tangential forces (F_{Hrup}) were recorded, while the values of the cutting force components (f_{Vcut} , f_{Hcut}) were calculated from the experimental measurements (Section 2.2.2). Figure 2.16 shows the values of the fracture forces for different values of the slice/push ratio. The experimental force values were measured on the cutting testbed (Section 2.3.2) and compared with the results from the analytical models presented in Section 2.2. Table 2.4 sums up the parameter values for the prediction of the cutting forces, according to Eqs. (2.22)-(2.23), and material characterization

results (Section 2.3.3). The Poisson coefficient, η , is considered equal to 0.5, which is the theoretical value for incompressible materials.

Table 2.4. Function parameters that are necessary to calculate the theoretical values of the axial and tangential cutting force (Eqs. (2.16)-(2.17)).

Parameter	Value
R	35 J/m ²
E	12.9 kPa
η	0.5

The dynamic friction coefficients, μ_{da} and μ_{dr} (Eqs. (2.22)-(2.23)), are a function of the slice/push ratio (k), and were obtained through a polynomial fit of the experimental cutting forces (Table 2.5).

Each mark in Fig. 2.16 represents the mean value of five insertions performed for a specific k with the related error bars. It is apparent that as soon as the needle starts to rotate ($k = 0.25$), the value of the axial force (F_{Vrup}) drops by approximately 45% and its minimum value at $k = 4$ is 83% lower than the value of F_{Vrup} for $k = 0$. However, the reduction rate in the axial fracture force (F_{Vrup}) is quite limited for $k > 1.5$. Instead, the tangential fracture force (F_{Hrup}) tends to slightly increase for increasing values of k .

These results suggest that a slice/push ratio ranging from 1 to 2 ($1 < k < 2$) is highly recommended to decrease the fracture forces. The results are aligned with the findings obtained in previous studies performed with similar medical devices (Han et al., 2013a). The presence of the slicing motion determines a rise of localized stresses in the contact area and decreases the amount of axial force needed to initiate the fracture of the tissue.

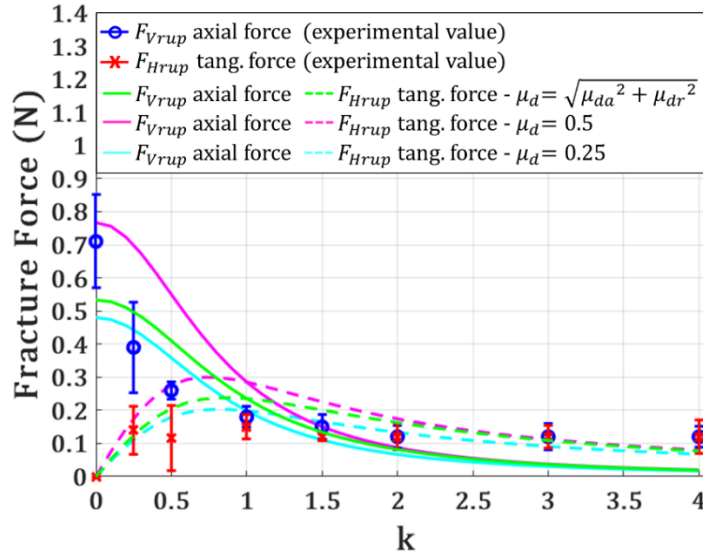


Figure 2.16. Mean value and error bar of fracture forces (F_{Vrup} , F_{Hrup}) and the related analytical model curves (Eqs. (2.16)-(2.17)).

Table 2.5. Polynomial regression equation with related R^2 and RMSE for dynamic friction coefficients as a function of the slice/push ratio (k).

Coefficient	Polynomial Regression Equation	R^2	RMSE
$\mu_{da}(k)$	$0.002418 k^2 - 0.0294k + 0.294$	0.925	0.001
$\mu_{dr}(k)$	$-0.03423 k^2 + 0.2181k + 0.0542$	0.942	0.034

Figure 2.17 shows the behavior of the cutting forces per unit displacement (f_{Vcut} , f_{Hcut}) after fracture is initiated. From Fig. 2.17, it can be noticed that the impact of the rotational motion on the axial cutting forces is quite limited: f_{Vcut} decreases by 21% for insertions performed at $k = 4$ with respect to insertions performed at $k = 0.25$. In fact, the needle is advancing at the same axial speed for each k and, consequently, the rotational motion does not greatly affect the cutting force in the axial direction. Instead, tangential cutting forces increase consistently for higher values of k ($k > 0.5$) since the needle is rotating at a faster speed for increasing values of the slice/push ratio (k).

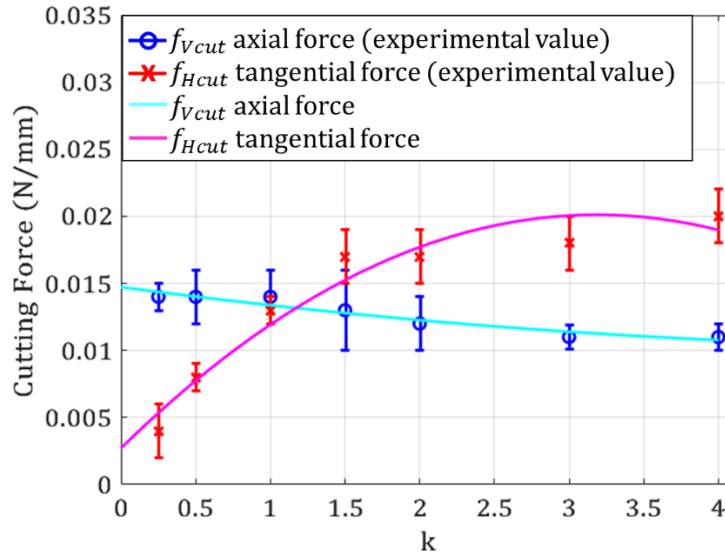


Figure 2.17. Mean values and error bars of cutting force (f_{Vcut} , f_{Hcut}) and the related analytical model curves (Section 2.2.2, Table 2.5).

These results suggest that a slice/push ratio smaller than 1.5 is recommended to contain the increase of tangential cutting forces after fracture initiation. Figure 2.18 shows the axial and tangential force behavior and confirms the impact of the rotational motion on lowering the axial fracture force and increasing the tangential force during cannula insertion.

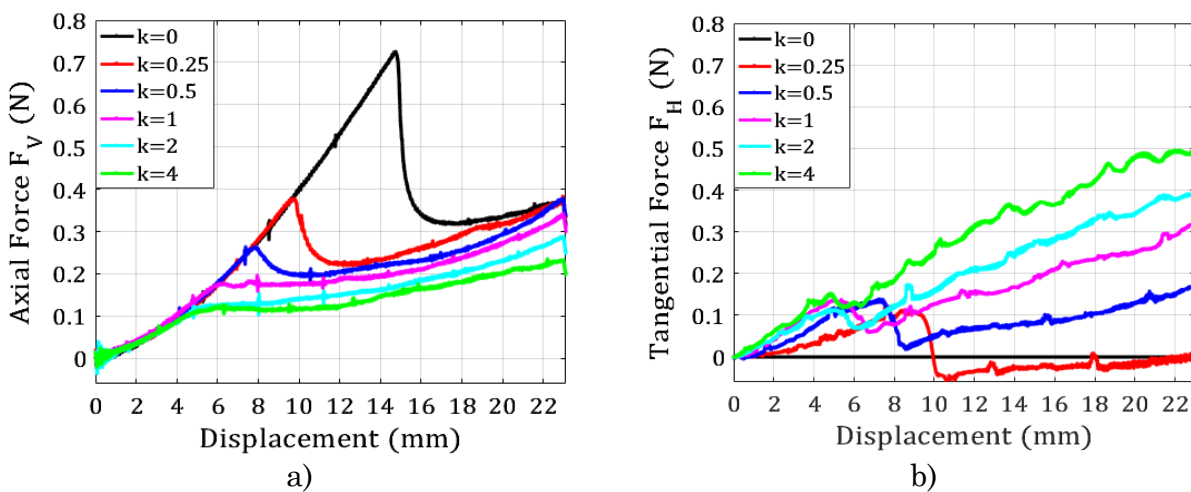


Figure 2.18. (a) Axial force (F_V) and (b) tangential force (F_H) behavior during needle penetration for different slice/push ratios, k .

2.5.2 Impact of the Slice/Push Ratio at Different Axial Speeds

In these tests, the goal was to assess the impact of the rotational motion on tissue cutting at several axial speeds since clinical needle insertion velocities may vary from 0.4 to 10 mm/s (Dimaio & Salcudean, 2003). A conical 14-gauge cannula with an included angle θ of 15° was inserted at translational speeds (v_t) equal to 0.5, 1, 2, 4 and 6 mm/s. For each insertion speed, the slice/push ratio ($k = v_r/v_t$) was set to 0, 0.25, 0.5, 1, 1.5, 2, 3 and 4. The cannula was inserted five times for each scenario for a total of 200 insertions. For each insertion, the maximum value of the axial cutting force (F_V), and the maximal value of the tangential cutting force (F_H), during the needle insertions were recorded. The values of the rupture forces (F_{rup}), are not highlighted in this analysis because it was extremely difficult to identify the penetration depth at which soft tissue fractures for slice/push ratios (k), greater than 2, and axial speeds greater than 1mm/s.

Figure 2.19 shows the maximum values of the axial and tangential forces (F_V and F_H) for different slice/push ratios and different axial speeds. The surfaces represent the best polynomial fits for F_V and F_H as a function of the slice push ratio (k) and translational speed (v_t).

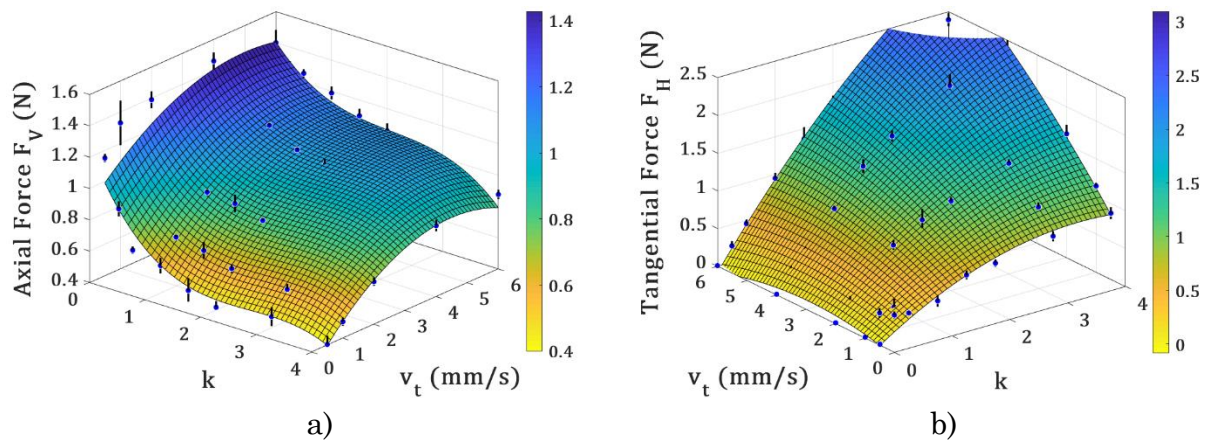


Figure 2.19. (a) Maximum axial forces (F_V) and (b) tangential forces (F_H) for insertions performed at different slice/push ratios and different insertion speeds. The experimental points with related error bars are also shown.

The data fit in Fig. 2.19b (Eq. (2.39)) was realized with a 2nd order polynomial surface and provided an $R^2 = 0.977$ with a root-mean-square deviation (RMSE) equal to 0.1 (Table 2.6):

$$F_H(k, v_t) = -0.0561 + 0.457k + 0.1258v_t - 0.0743 k^2 + 0.1058kv_t - 0.0217v_t^2 \quad (2.39)$$

For each insertion speed, the minimum value of the axial force is achieved at the maximum value of the slice push ratio, k (Fig. 2.19a). However, the rotational motion is more effective for axial speeds ranging from 0.5 to 2 mm/s for which the axial force decreases respectively by 50% and 35% for insertions performed at $k = 1$ with respect to insertions performed without any rotations ($k = 0$). Moreover, the reduction of the axial cutting forces is particularly consistent for low slice/push ratios ($k < 2$), as observed previously in Section 2.5.1. These findings show how the application of rotational motion is particularly crucial at low insertion speeds, which are usually very common in the clinical environment to reduce distress on tissues and organs.

Figure 2.19b illustrates how tangential forces are mostly independent of the values of the axial speeds and are directly dependent on the value of the slice/push ratio. The greater the value of k is, the greater will be the rotational speed and, consequently, the tangential force during the cutting procedure.

Table 2.6. Polynomial regression equation with related R^2 and RMSE values for the axial and tangential forces as a function of the slice/push ratio (k) and speed (v_t).

Force	Polynomial Regression Equation	R^2	RMSE
$F_V(k, v_t)$	$0.888 - 0.653k + 0.216v_t + 0.251 k^2 + 0.047kv_t - 0.0217v_t^2 - 0.0317 k^3 - 0.009 k^2v_t - 0.0019kv_t^2$	0.923	0.090
$F_H(k, v_t)$	$-0.0561 + 0.457k + 0.1258v_t - 0.0743 k^2 + 0.1058kv_t - 0.0217v_t^2$	0.977	0.108

2.5.3 Impact of the Slice/Push Ratio for Different Materials

In these tests, the goal was to assess the impact of the rotational motion on tissue cutting of different phantom materials described in Section 2.3.3. In fact, core biopsies are performed on different organs and soft tissues such as breast tissue, bone marrow, and prostate. Each of these tissues possesses different material properties. For this reason, rotating insertions were performed on four different phantom materials (Table 2.1), with Young's modulus ranging from 5 to 32 kPa. For each material, a conical 14-gauge cannula needle with an included angle θ of 15° was inserted at a translational speed (v_t) equal to 1 mm/s and at slice/push ratios (k) equal to 0, 0.25, 0.5, 1, 1.5, 2, 3 and 4. The cannula was inserted five times for each scenario for a total of 160 insertions. For each insertion, the maximum value of the axial cutting force (F_V) and of the tangential cutting force (F_H) during the insertions were recorded as in Section 2.4. Figure 2.20 shows the values of the axial and tangential forces (F_V and F_H) for different slice/push ratios and different phantom materials.

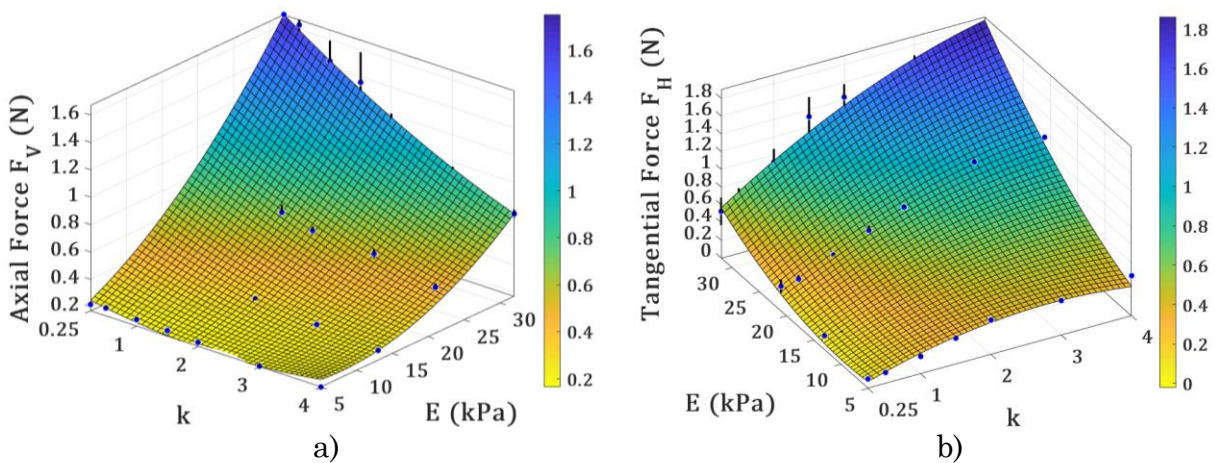


Figure 2.20. (a) Maximum axial forces (F_V) and (b) tangential forces (F_H) for insertions performed at different slice/push ratios on different phantom materials. The experimental points with related error bars are also shown.

The surfaces, in Fig. 2.20, represent the polynomial fits of F_V and F_H as a function of the slice push ratio (k), and of the Young's modulus. The corresponding surface coefficients, R^2 and RMSE are given in Table 2.7. For each material, the minimum value of the axial force is achieved at the maximum value of the slice push ratio, k (Fig. 2.20a). However, the rotational motion is more effective for hard phantom materials, characterized by Young's modulus (E) nearly equal to or higher than 13 kPa. In fact, for these materials, the axial force decreases between 75% and 60% for insertions performed at $k = 4$ in comparison to insertions performed without any rotations ($k = 0$). Moreover, the reduction of the axial cutting forces is particularly consistent for $k < 1$. These results show how the application of rotational motion is particularly crucial for "hard" tissues rather than for soft tissues ($E < 10$ kPa). Figure 2.20b illustrates how tangential forces are consistently higher for harder phantom materials. In particular, the tangential force has a higher increase rate with the slice/push ratio for materials with Young's modulus (E) equal to or higher than 21 kPa.

Table 2.7. Polynomial regression equation with related R^2 and RMSE values for the axial and tangential forces as a function of the slice/push ratio (k) and Young's modulus (E).

Force	Polynomial Regression Equation	R^2	RMSE
$F_V(k, E)$	$0.1354 + 0.0377k + 0.0083E + 0.0073 k^2 - 0.009kE + 0.0012E^2$	0.982	0.065
$F_H(k, E)$	$0.0905 + 0.22k - 0.0211E - 0.0479 k^2 + 0.0103kE + 0.001E^2$	0.966	0.096

2.6 Conclusions on Rotating Needles

In this chapter, an experimental study related to the impact of rotational motions during core biopsy procedures was performed. The ultimate goal was to provide a series of guidelines for

clinicians and surgeons to properly select the best needle tip geometry and cutting parameters for rotating needle insertions.

The study was conducted on 14-gauge cannula needles, which are common medical devices used for breast and bone marrow biopsies. The analytical models related to the cutting angles of several needle tip designs were analyzed and compared. Furthermore, a series of experimental cutting tests were performed with different cannula tip designs to assess: (i) the optimal geometry for rotating insertions, (ii) the benefits of rotational motions at different needle axial speeds, and (iii) on different phantom materials.

The results show that needles with low included angles (θ) and high inclination angles (λ) lead to lower cutting forces, as suggested by the analytical models. Two- and three-plane bevel needles with an included angle θ of 15° or lower represent the best tip geometries for soft tissue cutting. The application of these geometries during rotating needle insertion lower the axial fracture cutting force.

The analysis of the cutting motions at different slice/push ratios shows that the application of rotational motions leads to: (i) consistent decrease of the axial fracture forces, up to 80%, especially for $k < 2$, and (ii) a consistent increase of the tangential cutting forces after fracture is initiated. For this reason, a slice/push ratio of at least 1 is recommended before the rupture of soft tissue occurs. On the other hand, a slice/push ratio below 1.5 is recommended once the needle has penetrated the material. Moreover, the application of rotational motions is more critical for: (i) axial speeds ranging from 0.5 to 2 mm/s, which are the most common in a clinical environment, and for (ii) soft materials characterized by Young's modulus equal or higher than 13 kPa.

Additional investigations are needed on: (i) performing cutting tests on different phantom and biological tissues, such as pork skin or chicken breast, and (ii) developing analytical models to predict cutting forces. The findings of this study can be applied and extended to several biopsy procedures in which a cannula is adopted to extract a tissue sample from the human body.

3 Design and Models of Helical Hollow Needles

In the present chapter, 3D needle tip geometries will be proposed, which are inspired by helical drills, usually adopted for cutting of polymers and metals (Che et al., 2012; Ehmann et al., 2012; Lin et al., 1995). Current needle tip geometries are mainly obtained from a two-dimensional (2D) profile, which is extruded in one or more directions (Han et al., 2012; Moore et al., 2012b). However, current technology allows for the generation of virtually any three-dimensional (3D) surface. Even though such a surface may require a more sophisticated manufacturing process, this new geometry can also enhance the needle's cutting capabilities (Fig. 3.1). The fundamental goal is to demonstrate the design, mathematical models, manufacturing, and testing of helical needles. The proposed methodology can be applied to study any 3D needle geometry. First, the parametric equations that define the geometry of helical needles will be shown. The resulting surface will be defined and processed by using 3D computer aided design (CAD) and mesh software. The mathematical models to compute the cutting angles and fracture forces will be resolved and compared to the analytical models of the one-plane biopsy needle, commonly used in the clinical practice. Second, the experimental setup for the manufacture of helical needles is presented in detail. Finally, the performance of the helical needle geometry will be demonstrated through several insertions into phantom tissue. The results will prove the benefits accrued by the adoption of helical needles, which lead to lower cutting forces, and consequently provide larger biopsy samples (Moore et al., 2011). The findings of this study can be implemented by biomedical engineers to optimize the helical geometry and conceive novel 3D cutting edges for core biopsy examinations. This chapter is based on Giovannini et al. (Giovannini et al., 2019).

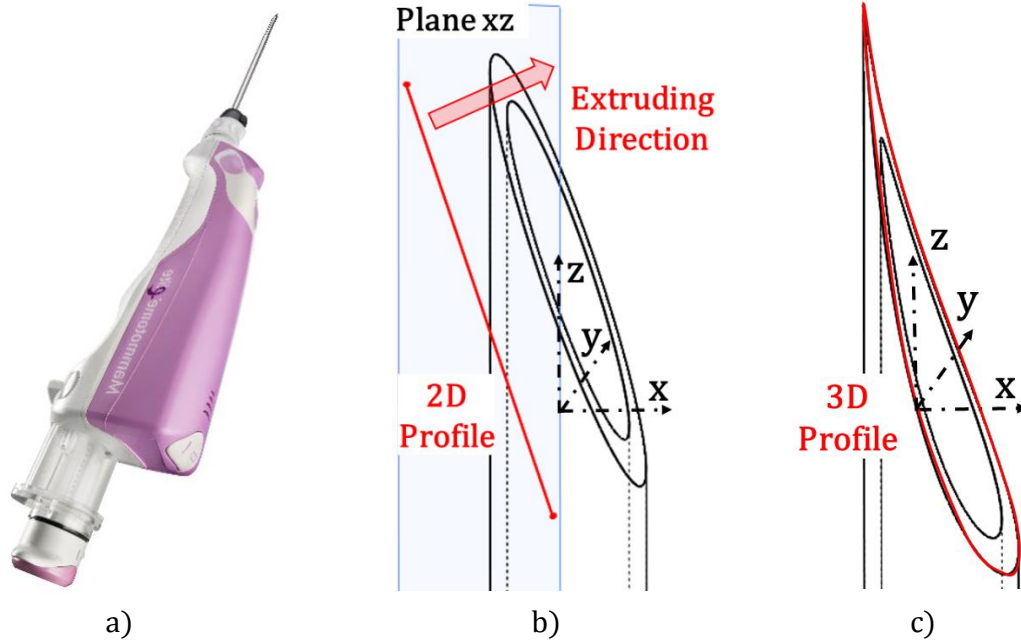


Figure 3.1. (a) Illustration of the breast biopsy device “Mammotome,” (b) hollow needle generated by a 2D profile, and (c) hollow needle generated by a 3D profile.

3.1 Mathematical Models for Helical Needles

In the present section, the design of helical needles will be investigated and applied to a 14-gauge cannula, which is commonly used for core biopsies. The tip geometry and cutting angle formulations will be explained and compared to those related to the widely used one-plane bevel needles. The manufacturing process of the helical needles will be presented in Section 3.2.

3.1.1 Geometric Description

The helical needle tip geometry can be obtained from the intersection of a conical helicoid with the cylindrical surface of the hollow needle (Ehmann et al., 2012). This geometry will be adopted to demonstrate the proposed procedure for the computation of the cutting angles for any arbitrary 3D needle geometry. A Cartesian coordinate system is defined with its x_h - and y_h -

axes passing through the origin of the conical helix and with the z_h -axis aligned with its longitudinal axis (Fig. 3.2). The parametric equations that describe the conical helix are:

$$x_h = -z_h \tan(\psi) \cos(\gamma_h) \quad (3.1)$$

$$y_h = -z_h \tan(\psi) \sin(\gamma_h) \quad (3.2)$$

$$z_h = -\frac{p_h}{2\pi} \gamma_h \quad (3.3)$$

where ψ and p_h are respectively the angle and the pitch of the helix, while γ_h defines the angular position on the helical profile. The radius of the conical helix r_h is given by:

$$r_h = z_h \tan(\psi) \quad (3.4)$$

The surface of the hollow needle is defined in a different Cartesian coordinate system (Fig. 3.2), where the x_n - and y_n -axes pass through the center of the needle's circular base and the z_n -axis is parallel to the z_h -axis. The needle's cylindrical surface is defined by the following parametric equations:

$$x_n = r_n \cos(\gamma_n) \quad (3.5)$$

$$y_n = r_n \sin(\gamma_n) \quad (3.6)$$

$$z_n = z \quad (3.7)$$

where r_n is the radius of the hollow needle and can refer to the external radius of the needle (r_{no}) or to the internal radius (r_{ni}), γ_n is the angular position on the cylindrical profile, and z represents the height of the needle. The cylindrical surface is centered at the origin of the x_n - and y_n -axes, and it is rotated by an angle φ with respect to the conical helix.

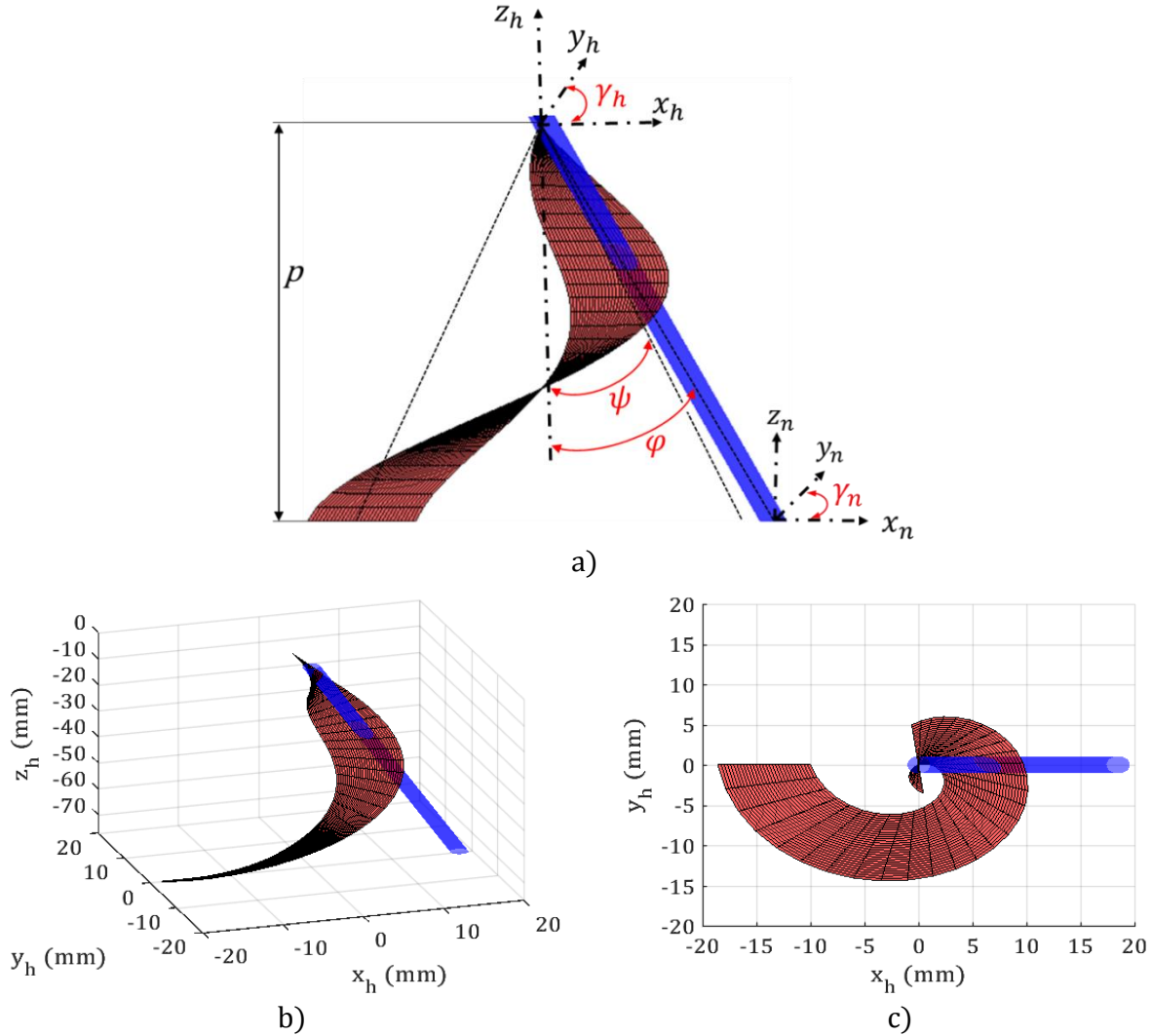


Figure 3.2. (a) Schematics of the intersection between the conical helical surface and the cylindrical surface and (b, c) the 3D geometrical model.

The final coordinates of the needle surface can be obtained by multiplying Eq. (3.5)-(3.7) by the rotation matrix R_n :

$$\mathbf{X}_{n\varphi} = \mathbf{R}_n \mathbf{X}_n \quad (3.8)$$

$$\begin{bmatrix} x_{n\varphi} \\ y_{n\varphi} \\ z_{n\varphi} \end{bmatrix} = \begin{bmatrix} \cos(\varphi) & 0 & \sin(\varphi) \\ 0 & 1 & 0 \\ -\sin(\varphi) & 0 & \cos(\varphi) \end{bmatrix} \begin{bmatrix} x_n \\ y_n \\ z_n \end{bmatrix} \quad (3.9)$$

The resulting profile of the helical needle cutting edge can be obtained by intersecting the conical helical surface (Eqs. (3.1)-(3.3)) with the cylindrical surface of the needle (Eq. (3.9)). The analytical equation of the intersection profile between two surfaces can be easily determined only in simple cases (Barnhill et al., 1990). Several algorithms (Hartmann, 2003), which are embedded in commercial software, are usually adopted in more complex scenarios. For this reason, the helical profile of the needle cutting edge was obtained by defining the surfaces in CAD software (Fig. 3.3) and postprocessing them to investigate their geometry.

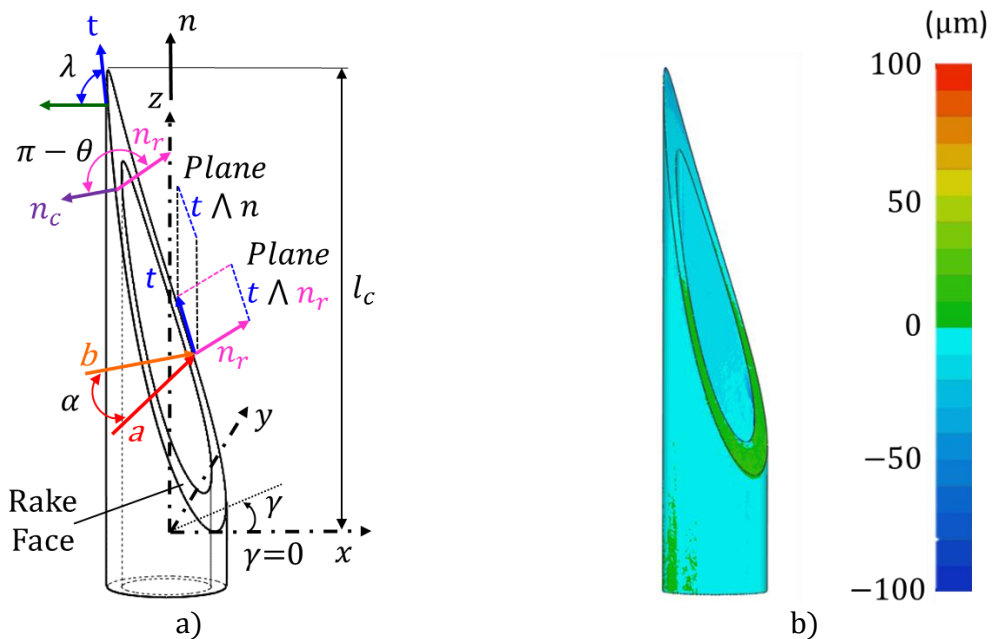


Figure 3.3. (a) Illustration of the helical needle's cutting edge and (b) its 3D scan after manufacturing, with the deviations with respect to the CAD model.

The cannula tip geometry can be characterized by three cutting angles (Han et al., 2012; Moore et al., 2010; Zheng et al., 2008): the inclination angle (λ), the included angle (θ), and the rake angle (α). Previous studies (Han et al., 2012) observed that a small θ and a large λ and α ,

lead to lower tissue fracture forces. In the next subsections, each parameter and variable introduced in Figs. 3.3 and 3.4 to define the needle's geometry will be defined. Furthermore, a methodology to compute each cutting angle (θ, λ, α) will be devised and demonstrated on a helical needle characterized by p_h of 100 mm, ψ of 10° , and φ of 13.5° .

To demonstrate the general validity of the above procedure for virtually any 3D surface, the determination of the parameters θ, λ , and α for the one-plane bevel needle (Table 3.2), will be demonstrated and compared to the helical tip. The helical needle parameters (p, ψ, φ) were chosen to compare helical needles with one-plane needles characterized by an identical length of the cutting edge (l_c).

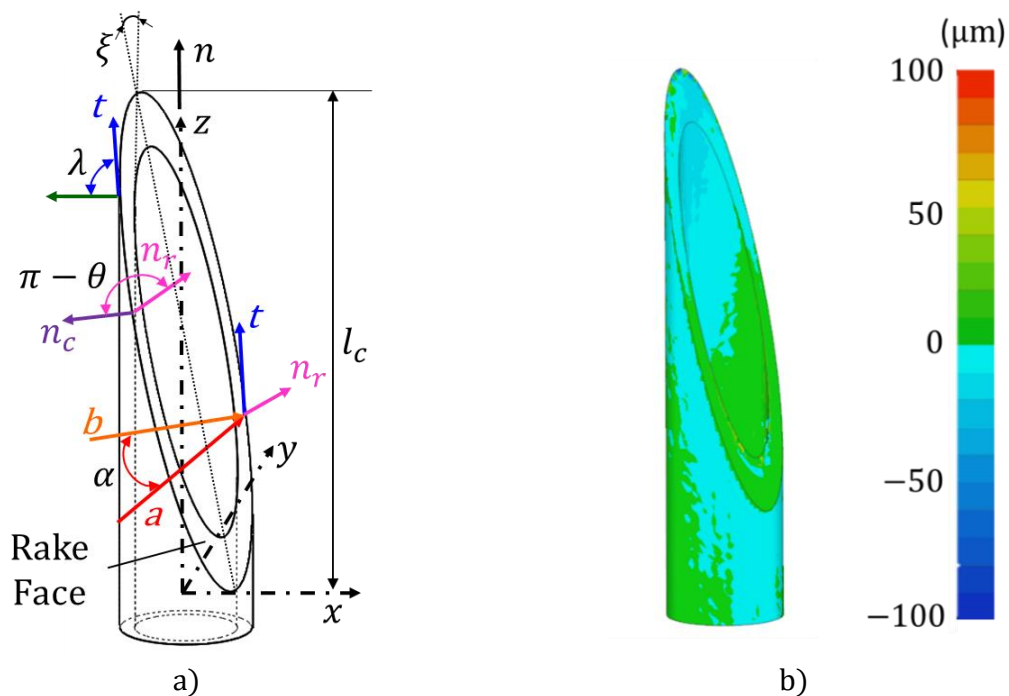


Figure 3.4. (a) Illustration of one-plane bevel cutting edge and (b) the related 3D scan after manufacturing, with the deviations with respect to the CAD model.

3.1.2 Inclination Angle (λ)

To analyze the needle's cutting angles, the needle geometry was imported into a 3D mesh processing software (Hypermesh), and a Cartesian coordinate system was defined with its x - and y -axes parallel to the base of the needle and the z -axis collinear with its longitudinal axis. The inclination angle, λ (Fig. 3.3), corresponds to the angle included between the vector \mathbf{t} tangent to the needle's cutting edge and the xy -plane with normal vector \mathbf{n} , where $\mathbf{n} = [0 \ 0 \ 1]$. The cross product between \mathbf{t} and \mathbf{n} allows to express the inclination angle (λ), as:

$$\lambda_o = \arcsin\left(\frac{|z_o'(\gamma)|}{\sqrt{r_{no}^2 + z_o'(\gamma)^2}}\right) \quad (3.10)$$

$$\lambda_i = \arcsin\left(\frac{|z_i'(\gamma)|}{\sqrt{r_{ni}^2 + z_i'(\gamma)^2}}\right) \quad (3.11)$$

where λ , z' and r_n can refer to the outside cutting edge (λ_o , z_o' , r_{no}) or to the inside cutting edge of the needle (λ_i , z_i' , r_{ni}) and z' refers to the first-order derivative of the cutting edge, which is assumed to be continuous (class C^1). To compute the inclination angle, λ (Fig. 3.3), the meshes related to the external and internal cutting edges were composed of 363 and 302 linear elements of 50 μm length. The coordinates of each element's nodes were then imported into MATLAB and fitted to a Fourier distribution ($R^2 = 1.000$) to obtain the needle tip profile $z_o(\gamma)$ and its derivative $z_o'(\gamma)$, as shown by the following equations:

$$\begin{aligned} z_o(\gamma) = & a_0 + a_1 \cos(w\gamma) + b_1 \sin(w\gamma) + a_2 \cos(2w\gamma) \\ & + b_2 \sin(2w\gamma) + a_3 \cos(3w\gamma) + b_3 \sin(3w\gamma) + a_4 \cos(4w\gamma) \\ & + b_4 \sin(4w\gamma) + a_5 \cos(5w\gamma) + b_5 \sin(5w\gamma) \end{aligned} \quad (3.12)$$

$$\begin{aligned} z_o'(\gamma) = & -wa_1 \sin(w\gamma) + wb_1 \cos(w\gamma) - 2wa_2 \sin(2w\gamma) \\ & + 2wb_2 \sin(2w\gamma) - 3wa_3 \sin(3w\gamma) + 3wb_3 \cos(3w\gamma) \\ & - 4wa_4 \sin(4w\gamma) + 4wb_4 \cos(4w\gamma) - 5wa_5 \sin(5w\gamma) \\ & + 5wb_5 \cos(5w\gamma) \end{aligned} \quad (3.13)$$

The same procedure was adopted to calculate the helical tip profile on the inside cutting edge $z_i(\gamma)$ and its derivative $z_i'(\gamma)$. Both the outside and inside helical tip profiles were compared with the ones related to the bevel needle (Fig. 3.5), which can be formulated through analytical equations (Han et al., 2012; Moore et al., 2012b), as shown in Table 3.1. Figure 3.5a shows that in the proximity of the tip ($\gamma = 157^\circ$), the helical tip presents a narrower outside profile, $z_o(\gamma)$, and a steeper derivative function, $z_o'(\gamma)$, with respect to the bevel tip; while the internal tip profiles of the helical and bevel tip ($z_i(\gamma)$) seem quite similar (Fig. 3.5b).

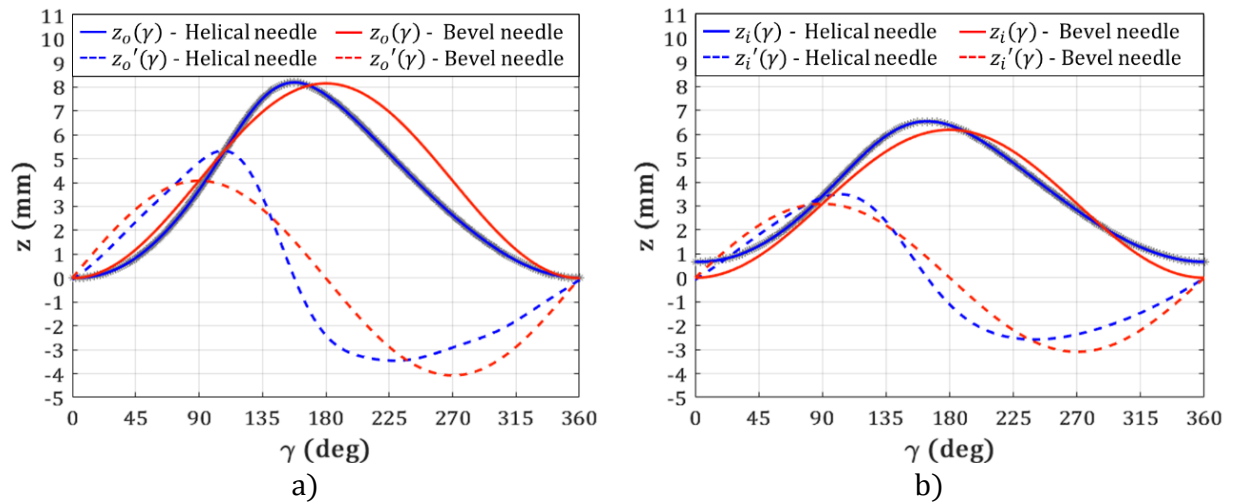


Figure 3.5. (a) Fourier fitting and analytical models (Table 3.1) for the outside and (b) inside cutting edge profiles of helical and bevel needles.

Figure 3.6 shows the values of the inclination angles, which were computed and plotted as a function of the angle γ and the z axis of helical (Eq. (3.10)-(3.11)) and bevel needle tips (Table (3.2)). In order to facilitate a comparison between different cutting edge profiles, the origin of the z axis was set at the starting point of the external cutting edge, ($z = 0$), which corresponds to the origin of the angle γ (Figs. 3.3-3.4).

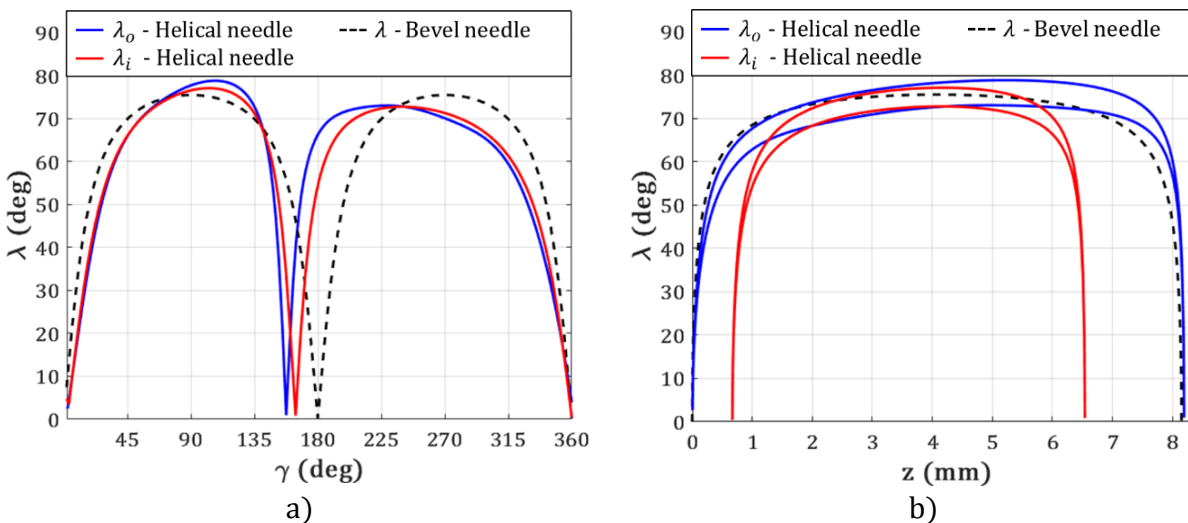


Figure 3.6. (a) Inclination angle (λ), for helical and bevel needles with respect to the angle γ and (b) to the distance z from the starting point of the cutting edge.

In bevel needles (Fig. 3.6), the inclination angle (λ), is equal to zero at the bottom ($\gamma = 0^\circ$, $z = 0$) and at the top of the needle tip ($\gamma = 180^\circ$, $z \cong 8$ mm) and it is symmetric with respect to the angle γ . Helical needles (Fig. 3.7a) present an asymmetric behavior of the inclination angle profiles, thus enhancing the flexibility of designing the needle tip for both the inside and the outside cutting edge.

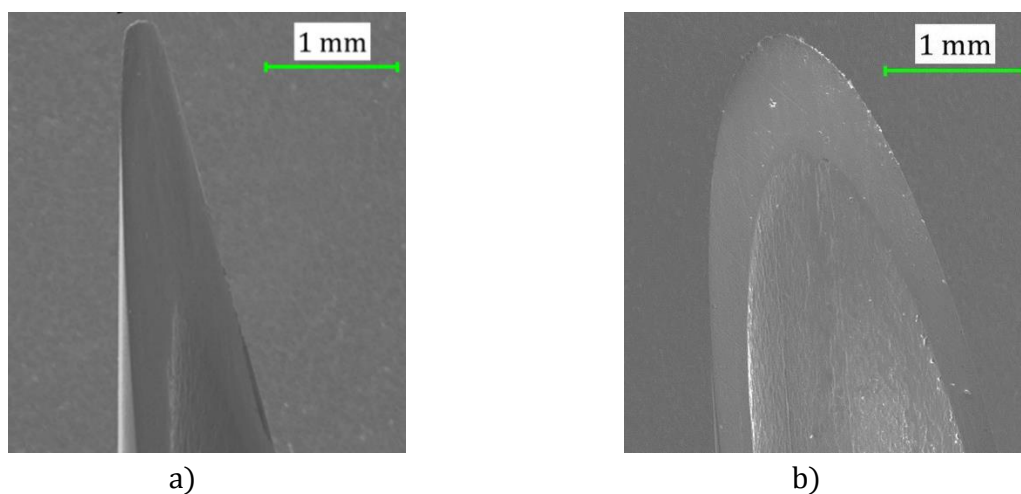


Figure 3.7. SEM pictures showing: (a) the helical and (b) bevel needle tips.

Furthermore, the shape of the helical cutting edges (Fig. 3.7), allows one to maintain higher values of λ at the needle tip (Fig. 3.6b) for values of z between 4 mm and 8 mm ($4 < z < 8$). It has been proven through mechanistic modeling that higher values of the inclination angle (λ), and of the rake angle (α), in hollow biopsy needles lead to lower tissue fracture forces (Han et al., 2012; Moore et al., 2011).

Table 3.1. Needle tip profiles and their derivatives for the outside ($z_o(\gamma)$) and inside cutting edges ($z_i(\gamma)$) (Han et al., 2012; Moore et al., 2012b).

$z(\gamma)$	Helical Needle	Bevel Needle
$z_o(\gamma)$	$3.535 - 3.884 \cos(w\gamma) + 0.696 \sin(w\gamma) + 0.339 \cos(2w\gamma) - 0.551 \sin(2w\gamma) + 0.033 \cos(3w\gamma) + 0.161 \sin(3w\gamma) - 0.0378 \cos(4w\gamma) - 0.0325 \sin(4w\gamma) + 0.0205 \cos(5w\gamma) - 0.002 \sin(5w\gamma)$ [$w = 0.999$; $R^2 = 1.00$]	$r_o(1 - \cos\gamma)\cot\xi$
$z_o'(\gamma)$	$-w3.884 \sin(w\gamma) + w0.696 \cos(w\gamma) - 2w0.339 \sin(2w\gamma) + 2w0.551 \sin(2w\gamma) + 3w0.033 \sin(3w\gamma) + 3w0.161 \cos(3w\gamma) - 4w0.0378 \sin(4w\gamma) - 4w0.0325 \cos(4w\gamma) + w0.020 \sin(5w\gamma) - w0.002 \cos(5w\gamma)$ [$w = 0.999$]	$r_o \sin\gamma \cot\xi$
$z_i(\gamma)$	$2.675 - 2.866 \cos(w\gamma) + 0.303 \sin(w\gamma) + 0.2 \cos(2w\gamma) - 0.26 \sin(2w\gamma) - 0.001 \cos(3w\gamma) + 0.058 \sin(3w\gamma) - 0.009 \cos(4w\gamma) + 1.988 \sin(4w\gamma) + 0.003 \cos(5w\gamma)$ [$w = 1.006$; $R^2 = 1.00$]	$r_i(1 - \cos\gamma)\cot\xi$
$z_i'(\gamma)$	$-w2.866 \sin(w\gamma) + w0.303 \cos(w\gamma) - 2w0.2 \sin(2w\gamma) + 2w0.26 \sin(2w\gamma) - 3w0.001 \sin(3w\gamma) + 3w0.058 \cos(3w\gamma) - 4w0.009 \sin(4w\gamma) + 4w1.988 \cos(4w\gamma) - w0.003 \sin(5w\gamma)$ [$w = 1.006$]	$r_i \sin\gamma \cot\xi$

3.1.3 Included Angle (θ)

The included angle, θ , is related to the rake face, which represents the surface included between the outside ($z_o(\gamma)$) and inside cutting edges ($z_i(\gamma)$) of the needle (Figs. 3.3- 3.4). The angle θ is defined as the angle between the vector normal to the rake face (\mathbf{n}_r) and the vector normal to the cylindrical face of the needle (\mathbf{n}_c) which is equal to: $\mathbf{n}_c = [\cos(\gamma) \ \sin(\gamma) \ 0]$. The dot product between the unit vectors \mathbf{n}_r and \mathbf{n}_c allows one to express the included angle θ as:

$$\theta = \pi - \arccos(\mathbf{n}_r \cdot \mathbf{n}_c) \quad (3.14)$$

To determine the components of the normal vector (\mathbf{n}_r), the mesh of the rake face of the helical needle was generated. The mesh was composed of 1,889 quadrilateral elements of symmetric group 4 (S4). The Computer Vision System Toolbox™ algorithms built in MATLAB were used to compute the surface normals, \mathbf{n}_r (Fig. 3.8b). The included angle (θ), was then computed for each node of the mesh and plotted in 3D (Fig. 3.8c).

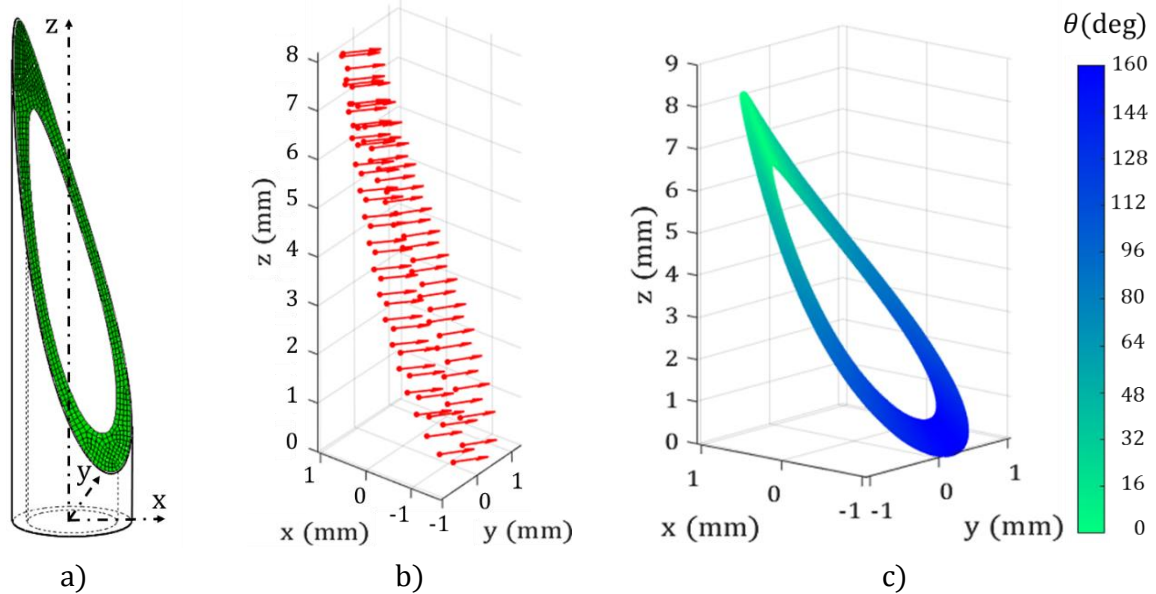


Figure 3.8. (a) Illustration of the mesh of the rake face, (b) the related normals for a few selected points of the mesh, and (c) the values of the angle θ .

Figure 3.9 shows the comparison between the behavior of the included angle (θ) for helical and one-plane bevel needles. It is observed (Fig. 3.9b) that the helical geometry allows for lower included angles at each point located in the upper part of the needle's rake face ($2 < z < 8$), which is the first part of the needle that enters in contact with the tissue during cutting. According to previous studies (Atkins, 2009; Han et al., 2012), small included angles play a

crucial role in decreasing soft tissue fracture forces in needles and knives for medical and food applications.

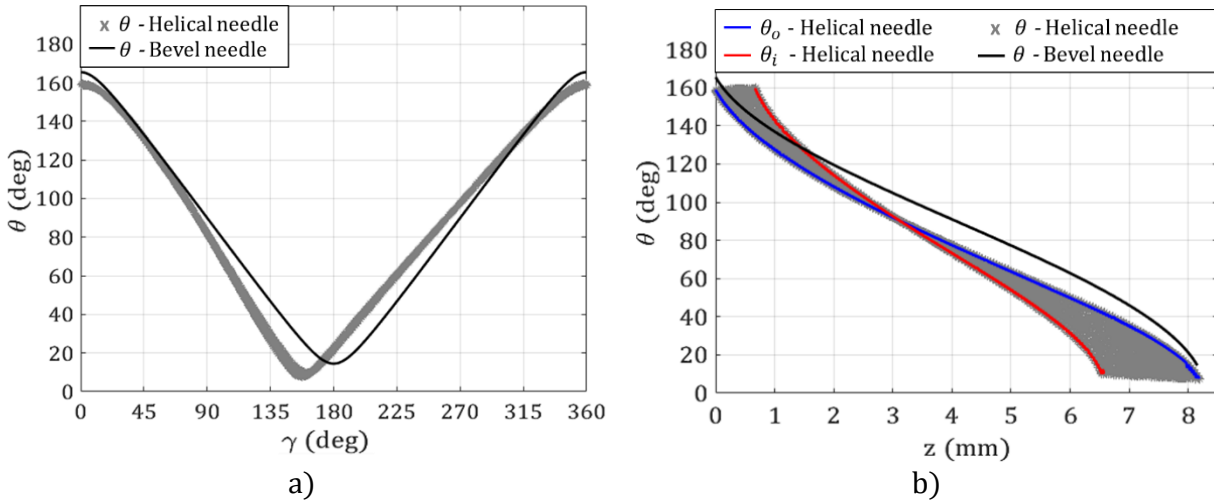


Figure 3.9. (a) Included angle, θ , for helical and bevel needles vs. the angle γ and (b) vs. the distance z from the starting point of the cutting edge.

3.1.4 Rake Angle (α)

The rake angle (α) is identified as the angle included between vectors \mathbf{a} and \mathbf{b} which intersects on the needle's cutting edge profile (David A. Stephenson, 2016; Moore et al., 2012b). The vector \mathbf{a} is perpendicular to the plane formed by the vector \mathbf{t} that is tangent to the needle's cutting edge, and by the vector \mathbf{n}_r , perpendicular to the rake face. Vector \mathbf{b} is perpendicular to the plane formed by the vector \mathbf{t} that is tangent to the needle's cutting edge, and by the vector \mathbf{n} perpendicular to the xy -plane (Figs. 3.3-3.4). Both the vectors \mathbf{a} and \mathbf{b} can be determined from the following cross products (Moore et al., 2012b):

$$\mathbf{a} = \mathbf{t} \times \mathbf{n}_r \quad (3.15)$$

$$\mathbf{b} = \mathbf{t} \times \mathbf{n} \quad (3.16)$$

The vectors \mathbf{t} , \mathbf{n} and \mathbf{n}_r were determined in Sections 3.1.1 and 3.1.2. The resulting rake angle, α , is then obtained from (Moore et al., 2012b):

$$\alpha = \arccos\left(\frac{\mathbf{a} \cdot \mathbf{b}}{|\mathbf{a}||\mathbf{b}|}\right) \quad (3.17)$$

The results for the outside and inside helical tip are presented in Fig. 3.10, where α is computed also for the one-plane bevel needle (Table 3.2).

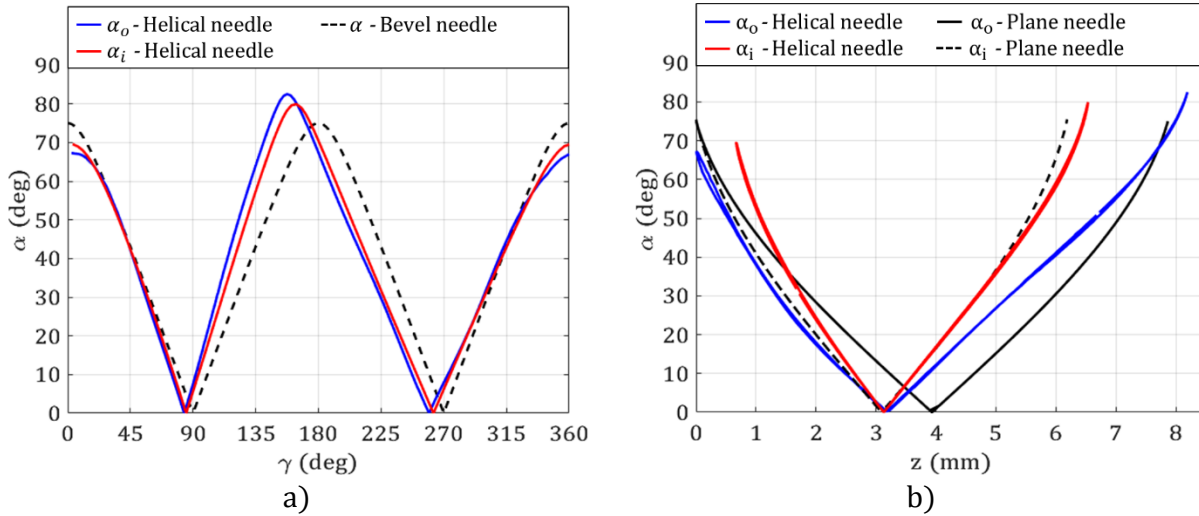


Figure 3.10. (a) Rake angle, α , for helical and bevel needles vs. the angle γ and (b) vs. the distance z from the start point of the cutting edge.

The helical needle tip presents more favorable geometry for tissue cutting for $z > 4$ mm, for which the value of the rake angle (α) is higher with respect to the value obtained for the bevel needle geometry. Furthermore, bevel needles present identical rake angle values with respect to the xy -plane, since:

$$\alpha(0^\circ < \gamma < 180^\circ) = \alpha(180^\circ < \gamma < 360^\circ) \quad (3.18)$$

whereas helical needles present an asymmetric behavior that could be exploited to lower the insertion forces.

Table 3.2. Cutting parameters $(\theta, \lambda, \alpha)$ for helical and bevel needles.

Needle	λ	θ	α
Helical	$\arcsin \left(\frac{ z_o'(\gamma) }{\sqrt{r_{no}^2 + z_o'(\gamma)^2}} \right)$	$\pi - \arccos(\mathbf{n}_r \cdot \mathbf{n}_c)$	$\arccos \left(\frac{\mathbf{a} \cdot \mathbf{b}}{ \mathbf{a} \mathbf{b} } \right)$
Bevel	$\arcsin \frac{ \cot \xi \sin \gamma }{\sqrt{1 + \cot^2 \xi \sin^2 \gamma}}$	$\pi - \arccos(\cos \xi \cos \gamma)$	$\arccos \sqrt{\cos^2 \gamma \sin^2 \xi + \sin^2 \gamma}$

3.1.5 Fracture Forces and Slice/Push Ratio

During tissue cutting, the needle's tip is subjected to an axial force (F_a), which is parallel to the needle's longitudinal axis and a tangential force (F_t), which is tangent to its external cylindrical surface (Fig. 3.11). These forces can be decomposed into F_{\perp} and F_{\parallel} , the forces perpendicular and tangent to the needle's cutting edge, respectively (Fig. 3.11). They play a fundamental role in tissue fracture. The cutting forces F_{\perp} and F_{\parallel} can be determined as shown in Section 2.2.1:

$$F_{\perp} = \frac{2R\pi r_{ni}G}{1 + k^2 - \frac{\mu_d \sqrt{(k \cos(\theta))^2 + 1}}{\cos(\theta) (\mu_d \cos(\varepsilon) \cos(\theta) + \sin(\theta))}} \quad (3.19)$$

$$F_{\parallel} = \frac{2R\pi r_{ni}kG}{1 + k^2 - \frac{\mu_d \sqrt{(k \cos(\theta))^2 + 1}}{\cos(\theta) (\mu_d \cos(\varepsilon) \cos(\theta) + \sin(\theta))}} \quad (3.20)$$

where R is the strain energy release rate of the tissue, k is the slice/push ratio ($k = v_{\parallel}/v_{\perp}$) between v_{\parallel} and v_{\perp} : the velocities tangential and perpendicular to the needle's cutting edge, respectively. G is a geometrical factor (0.3:0.4), which takes into account the needle contact

length at fracture, and it was considered 10% smaller for helical needles since they present a narrower tip (Fig. 3.7).

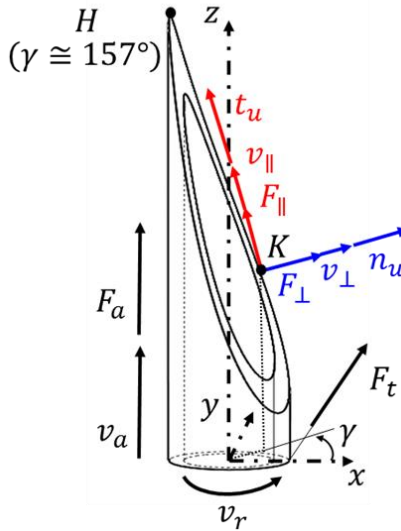


Figure 3.11. Helical cannula tip. The geometry and the main vectors representing directions, velocities, and forces.

The velocity v_{\parallel} can be calculated from the dot product between the velocity vector \mathbf{v} ($\mathbf{v} = [-v_r \sin(\gamma) \ v_r \cos(\gamma) \ v_a]$) and the unit vector \mathbf{t}_u , which is tangent to the needle's cutting edge profile (Han, 2014). For one plane bevel needles the tangent vector \mathbf{t}_u can be expressed as:

$$\mathbf{t}_u = \left[\frac{-\sin(\gamma)}{\sqrt{1 + \cot^2(\xi) \sin^2(\gamma)}} \quad \frac{\cos(\gamma)}{\sqrt{1 + \cot^2(\xi) \sin^2(\gamma)}} \quad \frac{\sin(\gamma) \cot(\xi)}{\sqrt{1 + \cot^2(\xi) \sin^2(\gamma)}} \right] \quad (3.21)$$

The velocity v_{\parallel} can then be obtained by (Han, 2014):

$$v_{\parallel} = \mathbf{v} \cdot \mathbf{t}_u = \frac{v_r + v_a \cot(\xi) \sin(\gamma)}{\sqrt{1 + \cot^2(\xi) \sin^2(\gamma)}} \quad (3.22)$$

The velocity v_{\perp} can be consequently calculated from: $v_{\perp} = \sqrt{|\mathbf{v}|^2 - v_{\parallel}^2}$. The resulting slice/push ratio can be expressed as (Han, 2014):

$$k = \frac{v_{\parallel}}{v_{\perp}} = \frac{|S + \cot(\xi) \sin(\gamma)|}{|1 - S \cot(\xi) \sin(\gamma)|} \quad (3.23)$$

where S is the needle rotation/translation ratio ($S = v_r/v_a$), which represents the ratio between the rotational speed of the needle (v_r) and the speed parallel to the longitudinal needle axis (v_a). The slice/push ratio k varies along the cutting edge, depending on the radial position γ of a point K at which k is calculated (Fig. 3.11) and it consequently determines the variation in the forces F_{\perp} and F_{\parallel} . The same procedure to calculate the slice push ratio (k), can also be used for helical needles, where the unit tangent vector \mathbf{t}_u can be obtained from the vector \mathbf{t} computed in Section 3.1.2.

Figure 3.12a shows the behavior of the tangential (F_{\parallel}) and perpendicular (F_{\perp}) fracture forces as a function of angle γ for helical and bevel needles characterized by the geometry described in Section 3.1.

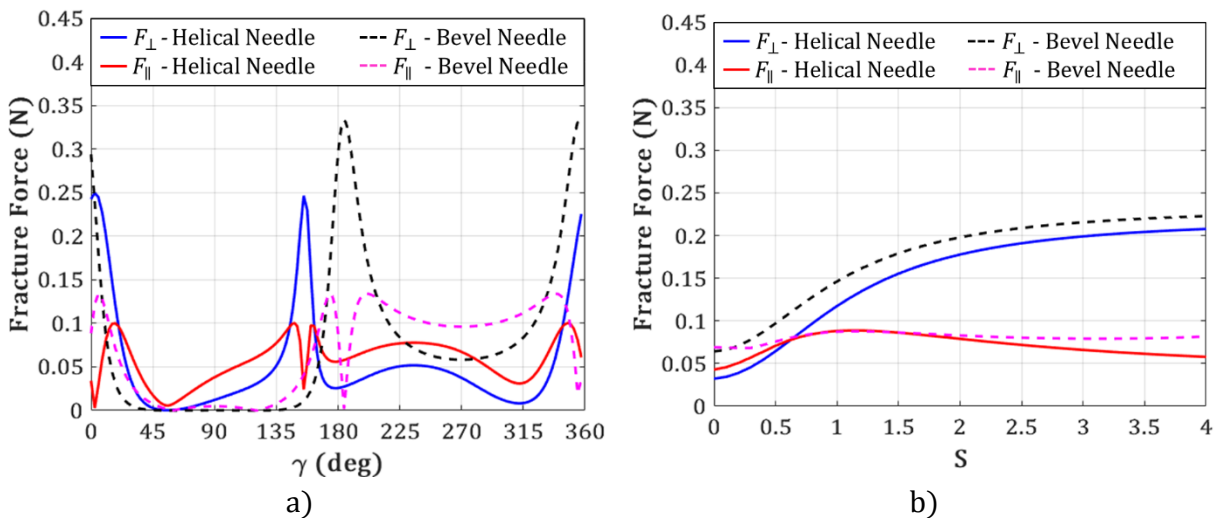


Figure 3.12. (a) Fracture force values for helical and bevel needles vs. the angle (γ) for a rotation/translation ratio (S), equal to 0.3 and (b) the behavior of the mean value of the fracture forces for different rotation/translation ratios (S).

The dynamic friction coefficients (μ_d), and the strain energy release rate (R), were considered equal respectively to 0.4 (Section 2.2.1) and 45 J/m², which are common values adopted for similar soft tissue (Han et al., 2013a). The maximum value of F_{\perp} is reached at the base of the needle's rake face ($\gamma = 0^\circ$) and at the tip of the cutting edge. This corresponds to $\gamma = 180^\circ$ for the one-plane bevel needle, and to $\gamma = 157^\circ$ for the helical needle (Fig. 3.11).

The comparison between the fracture forces of the helical and bevel needles is performed by considering the average value of the forces as a function of the angle. The average force values are plotted for different rotation/translation ratios (S) (Fig. 3.12b). According to the analytical model, helical needles and bevel needles present similar force behavior at different ratios S . Helical needles have the potential to lower the tangential fracture forces for $S > 2$ and increase the perpendicular fracture forces for $S > 0.5$. This force model helps to predict the value of the fracture forces (Section 3.1.5), but it also presents several limitations. For instance, it is extremely challenging to correctly evaluate the length of the contact (w) between the needle and soft tissue when fracture occurs. Further, the dynamic friction coefficients (μ_d), and the tissue strain energy release rate (R), are considered to be constant at different needle rotation/translation ratios (S), (Han et al., 2013a), since the main emphasis of this research is to determine the impact of 3D needle geometries on the cutting forces. The cutting speed might have an impact on the friction coefficient, while its effect on the tissue strain energy release rate (R), is not relevant (Wang et al., 2014).

3.2 Manufacturing Process for Helical Needles

Helical needles were obtained from a 14-gauge 304 stainless cannula, which is commonly used for hypodermic needles. A vertical machining center (VF-2 model, Haas Automation Inc.,

Oxnard, CA) was used to generate the helical needle tip (Fig. 3.13). The 3D geometry of the helical needles was imported into Unigraphics NX (Siemens PLM Software, Plano, TX), a Computer-Aided Manufacturing software (CAM) to generate the toolpath. This machining center allows the rotation of the tool, its translation in the vertical direction (Z) and the translation of the needle in two orthogonal directions (X, Y) to generate helical needle tips.

The resolution of the translational axes is 0.002 mm. The tool used was a carbide ball mill with a diameter of 1.588 mm. The 14-gauge cannulas were set in an ER8 collet, which was located on a vice positioned on the table of the machining center.

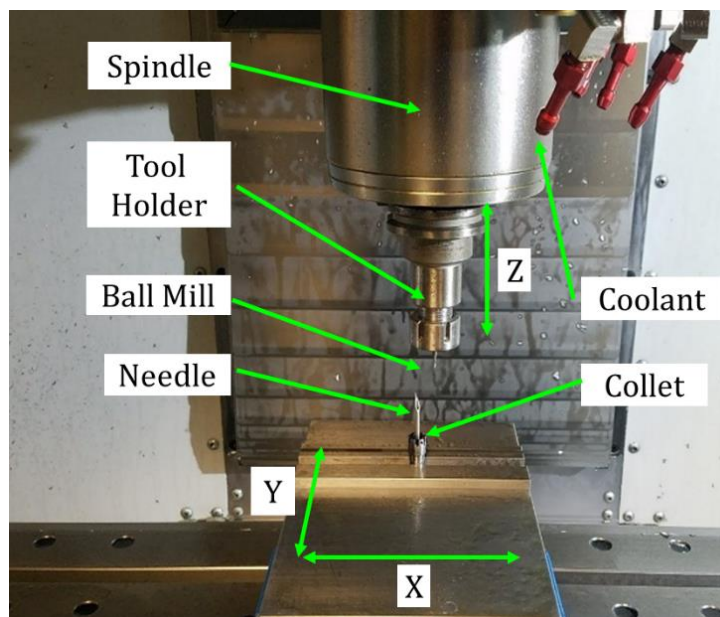


Figure 3.13. VF-2 Haas vertical machining center with the motion axes (X, Y, Z) and the main components of the manufacturing setup highlighted.

During the milling operations, the needle was moving in the X and Y directions, while the tool was rotating at 10,000 rpm and progressively shaping the needle at a feed rate of 0.08 mm/min. After machining, the needle tips were manually deburred and cleaned by a Branson

ultrasonic bath (Branson Ultrasonics Corp., Danbury, CT). In addition, a Dremel Multipro rotary tool (Dremel, Mount Prospect, IL) was used to polish the rake face of the needle with a felt polishing wheel. The 3D profile was measured with a surface measurement system (ALICONA InfiniteFocus) and compared to the CAD model.

3.3 Impact of Helical Needles on Experimental Cutting Forces

Helical needle geometry was validated by performing several cutting tests on the custom-built testbed (Section 2.3.2). The cannula was inserted into phantom tissue composed of the 8116SS plastic with the 4116S plastic softener S/P ratio equal to 0.25 (as described in Section 2.3.3). The fundamental objective was to understand: (i) the effect of the needle tip configuration on the cutting forces (Section 3.3.1), and (ii) the behavior of the fracture forces at different rotation/translation ratios ($S = v_r/v_a$).

3.3.1 Helical Needle`s Impact on Cutting Forces

Needle fracture forces were measured for a helical needle ($p_h = 100$ mm, $\psi = 10^\circ$, $\varphi = 13.5^\circ$) and a one-plane bevel needle ($\xi = 14.5^\circ$), both with the same length of the cutting edge (l_c). The tests were performed on phantom tissue (Section 2.3.2) for translational and rotational insertions. In the first scenario, the needles were inserted without the addition of any rotation ($v_r = 0$ mm/s), at a translational speed (v_t) of 1 mm/s (Dimaio et al., 2003). During rotational insertions ($v_r = 2$ mm/s), the needles were rotated counterclockwise, while they were advanced into the tissue, as it takes place during core biopsies. The ratio between the rotational and translational speeds was maintained at 2, which is the suggested value to decrease the insertion forces (Han et al., 2013a). During each insertion, the needle was translated for 23 mm in the axial

direction, and each experiment was repeated six times. Figure 3.14 displays the cutting forces for translational and rotational insertions. The tangential force is not shown for translation insertions since it is equal to zero (Fig. 3.14b).

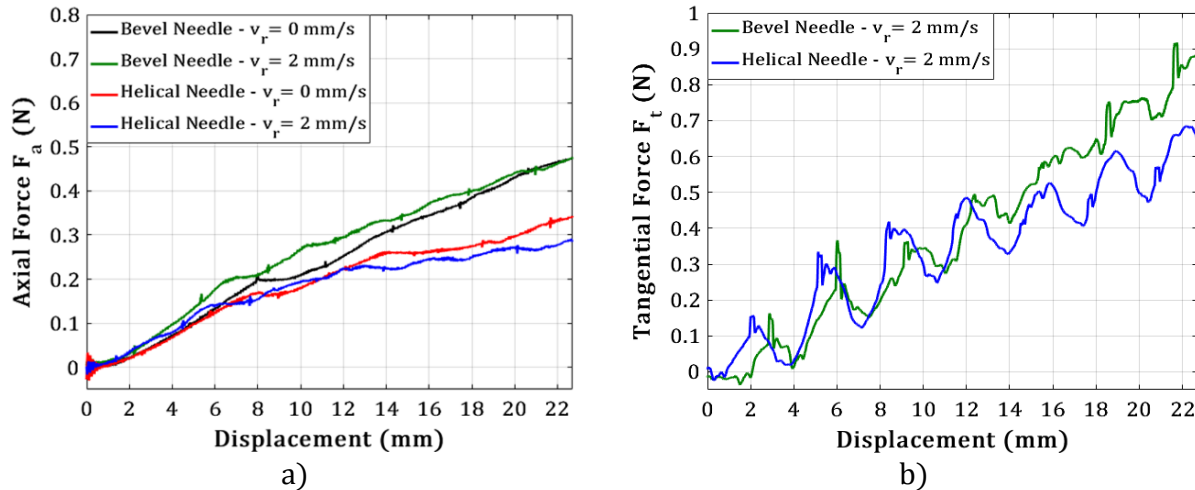


Figure 3.14. (a) Cutting force behavior in the axial (F_a) and (b) tangential direction (F_t) for helical and bevel needles.

From the plots (Fig. 3.14), it is evident that the helical needle tip configuration exhibits a consistent decrease of the axial and tangential force during rotational ($v_r = 2$ mm/s) and translational insertions ($v_r = 0$ mm/s). For instance, the helical needle force profile represented in the plot (Fig. 3.14a) is characterized by an axial force (at 23 mm), which is 38.3% lower than the axial force observed during bevel needle penetration.

An unpaired one-tailed test was performed to analyze the statistical implications related to the axial and tangential force measurements for helical and bevel needles (Table 3.3). The test was performed with a significance level (α) equal to 0.05, while the variances between the samples were considered unequal. The test compared the force values measured at a needle displacement of 23 mm. For rotating insertions performed with a helical needle, the axial

force ($\mu = 0.341$ N, $\sigma = 0.0243$ N) is 20.1% lower (p-value = 9.52×10^{-4}) than the axial force observed with a bevel needle ($\mu = 0.427$ N, $\sigma = 0.029$ N); a similar trend was observed when comparing the tangential forces (Table 3.3). Also, translational insertions performed with the helical needle led to lower axial forces than the insertions performed with the bevel needle. For both rotating and translational insertions, the force variation (ΔF) was calculated between the means (μ) of the tangential and axial forces ($\Delta F_V = \frac{F_{a_bevel} - F_{a_helical}}{F_{a_bevel}} 100\%$). The statistical results are summarized in Table 3.3.

Table 3.3. The mean value (μ), standard deviation (σ), p-value, and force variation (ΔF) for helical and bevel needles. The p-value is not reported for bevel needle insertions since they represent the term of comparison.

Force	v_r (mm/s)	μ (N)	σ (N)	p-Value	ΔF (%)
F_{a_bevel}	0	0.446	0.023	-	-
$F_{a_helical}$	0	0.354	0.036	1.3×10^{-3}	-20.53
F_{a_bevel}	2	0.427	0.029	-	-
$F_{a_helical}$	2	0.341	0.024	9.5×10^{-4}	-20.07
F_{t_bevel}	2	0.824	0.047	-	-
$F_{t_helical}$	2	0.686	0.065	8.4×10^{-3}	-16.70

These trends confirm the indications obtained from the analytical models, where helical needle geometry improved cutting angles (λ, θ, α) compared to bevel needles.

3.3.2 Helical Needle`s Impact at Different Slice/Push Ratios

In the previous section, it was observed that helical needles lead to a reduction in tangential and axial forces during rotational cutting. In this section, the effect of the cutting parameters on the fracture forces is investigated. The fundamental goal is to understand the optimal needle

rotation/translation ratio ($S = v_r/v_a$) that can lead to lower fracture forces. In the cutting tests, the helical needle described in Section 3.1, was inserted into the phantom tissue while it was steadily rotated.

The needle's axial speed (v_a) was set to 1 mm/s and the rotation/translation ratio, S , was set to 0.25, 0.5, 1, 1.5, 2, and 3. The needle was inserted five times for each value of S . The values of the axial (F_a) and tangential force at fracture (F_t) (Fig. 3.14a) were recorded by the piezoelectric dynamometer and torque sensor described in Section 2.3.2. The value of F_t was determined by dividing the torque at fracture by the needle's radius. The experimental fracture force, \mathbf{F}_{exp} , is composed of forces F_a and F_t — $\mathbf{F}_{exp} = \left[\frac{F_t}{2} \quad \frac{F_t}{2} \quad F_a \right]$ —where the force F_t was split equally between the x - and y -axes. The analytical values of the fracture forces F_{\perp} and F_{\parallel} computed in Section 3.1.5 (Eq. (3.19)-(3.20)) were projected in the direction of the needle's z -axis and in the x - and y -directions related to the torque sensor. The experimental values of the fracture forces were then compared to the values from the analytical model for each rotation/translation ratio (Fig. 3.15). Each mark in Fig. 3.15 identifies the mean value of five insertions executed for each value of S . From the experimental values in Fig. 3.15, it is evident that the axial force at fracture (F_a) tends to decrease with increasing S ratios while the tangential force at fracture (F_t), tends to only slightly increase for $S > 0$. According to these experimental results, a rotation/translation ratio higher than 1.5 ($S > 1.5$) is suggested to lower the fracture forces for helical needles. The application of the rotational motion during needle insertion causes an increase of stresses in the portion of tissue in contact with the needle tip and reduces the axial force necessary to fracture the material (Abolhassani et al., 2007b; Han et al., 2012). The analytical model predicts the behavior of the experimental values quite accurately. The

discrepancies between the experimental and the analytical values are due to the fact that at different values of S , the contact length (w) between the needle and soft tissue tends to vary, while in the analytical model it is assumed to be constant.

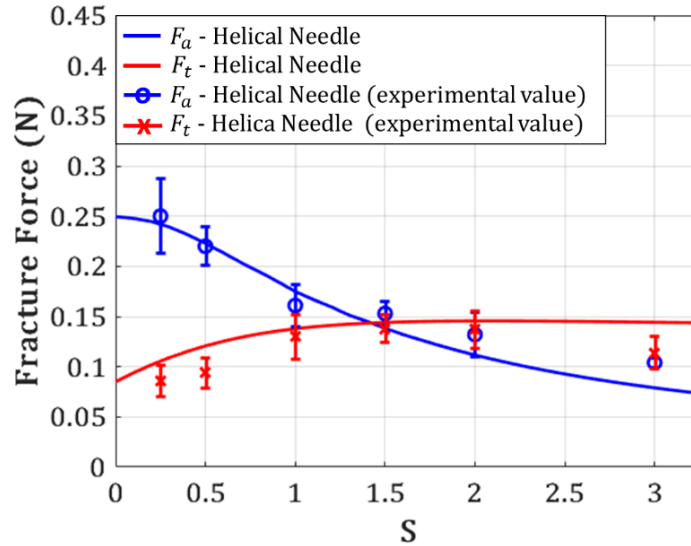


Figure 3.15. The mean value, error bar, and analytical values of fracture forces.

3.4 Optimization of Helical Geometry

In the previous sections, the choice of the helical needle parameters (Section 3.1) was performed to compare helical needles with one-plane needles characterized by an identical length of the cutting edge (l_c). Then, for each needle configuration the mathematical models were resolved to compute the main cutting angles. However, the relationship between the helical needle geometry (angles ψ , φ) and the resulting main cutting angles (λ , θ , α) was not explored. In this section, a Gaussian process model will be adopted to estimate the resulting cutting angles for a given combination of input angles. First, a review of the Gaussian process (GP) modeling will be provided (Section 3.4.1), then a GP model and an objective function will be formulated to

identify the optimal combinations of input parameters to create a helical needle geometry characterized by the desired cutting angles (Section 3.4.2).

3.4.1 Review on Gaussian Process Modeling

Since the rise of simulation-based science and engineering, surrogate modeling has become a promising tool that can replace expensive computer simulations. Even real experiments can be replaced with fast and accurate surrogate models. Of particular interest has been the use of Gaussian processes (GP's), proposed by Sacks et al. (Sacks et al., 1989) as surrogates. GP models can interpolate the data by viewing the response surface as a realization of a Gaussian random process. They also have a natural mechanism to model noisy data (i.e., to avoid interpolation) and have been widely used in a variety of applications, such as determining the response sensitivities to inputs, (Hassaninia et al., 2017; Tao et al., 2017), microstructure reconstruction (Bostanabad et al., 2016a, 2016b, 2018b), and enabling tractable and efficient Bayesian calibration and bias correction (Bostanabad et al., 2018a; Zhang et al., 2019).

In this work, the GP emulators (aka surrogates, metamodels, or models) were adopted to replace a computer simulator and, therefore, to estimate the outputs, which are represented by the length of the needle's cutting edge (l_c) and the minimum and maximum values of the cutting angles (λ, θ, α). The outputs and inputs of the computer simulator are denoted by y and by the d dimensional vector $\mathbf{x} = [x_{(1)}, x_{(2)}, \dots, x_{(d)}]^T$ where $\mathbf{x} \in \mathbb{R}^d$ that represents the input angles of the helical geometry (ψ, φ).

The input-output relation is assumed to be a realization of the random process $y(\mathbf{x})$:

$$y(\mathbf{x}) = \sum_{i=1}^h \beta_{(i)} f_i(\mathbf{x}) + \xi_0(\mathbf{x}) \quad (3.24)$$

where $f_i(\mathbf{x})$'s are some pre-determined sets of basis functions, $\boldsymbol{\beta} = [\beta_{(1)}, \dots, \beta_{(h)}]^T$ are unknown weights, and $\xi_\theta(\mathbf{x})$ is a zero-mean GP characterized with its parametric covariance function, $c(\cdot, \cdot)$ as:

$$\text{cov}(\xi(\mathbf{x}), \xi(\mathbf{x}')) = c(\mathbf{x}, \mathbf{x}') = \sigma_v^2 r(\mathbf{x}, \mathbf{x}') \quad (3.25)$$

where $r(\cdot)$ is the correlation function having the property $r(\mathbf{x}, \mathbf{x}) = 1$ and σ_v^2 is the process variance.

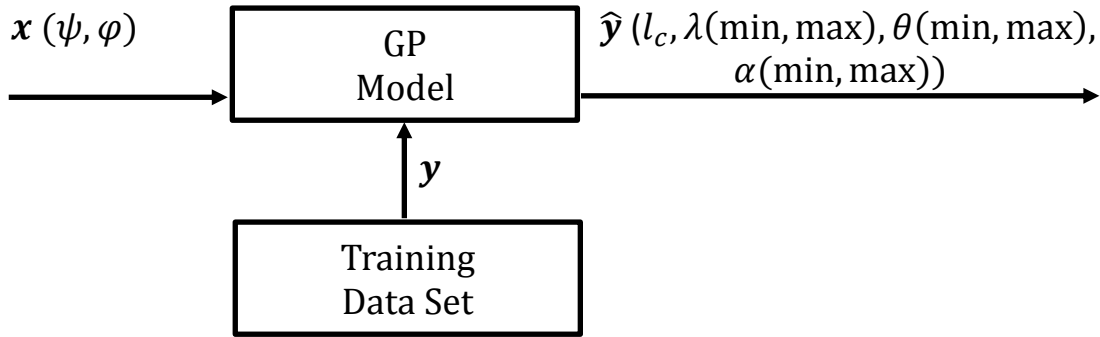


Figure 3.16. GP model scheme for the optimization of the helical needle geometry.

Various correlation functions have been developed in the literature, with the most widely used one being the Gaussian correlation function:

$$r(\mathbf{x}, \mathbf{x}') = \exp\{-(\mathbf{x} - \mathbf{x}')^T \boldsymbol{\Omega} (\mathbf{x} - \mathbf{x}')\} \quad (3.26)$$

where $\boldsymbol{\Omega} = \text{diag}(\mathbf{1}\boldsymbol{\omega})$ and $\boldsymbol{\omega} = [\omega_{(1)}, \omega_{(2)}, \dots, \omega_{(d)}]^T$, $-\infty < \omega_i < \infty$ are the roughness or scale parameters. The collection of σ^2 and $\boldsymbol{\omega}$ are called the hyperparameters.

With the formulation in Eq. (3.24) and given n training pairs of (\mathbf{x}_i, y_i) , GP modeling requires finding a point estimate for $\boldsymbol{\beta}$, $\boldsymbol{\omega}$, and σ^2 via either maximum likelihood estimation (MLE) or cross-validation (CV). Here, an MLE and constant process mean (i.e., $\sum_{i=1}^h \beta_i f_i(\mathbf{x}) = \beta$) were

adopted. These choices are widely practiced because high predictive power is provided while computational costs are minimized (Bostanabad et al., 2018a; Gramacy & Apley, 2015; MacDonald et al., 2013).

MLE requires maximizing the multivariate Gaussian likelihood function, or equivalently:

$$[\hat{\boldsymbol{\beta}}, \hat{\sigma}_v^2, \hat{\boldsymbol{\omega}}] = \underset{\boldsymbol{\beta}, \sigma^2, \boldsymbol{\omega}}{\operatorname{argmin}} \left(\frac{n}{2} \log(\sigma^2) + \frac{1}{2} \log(|\mathbf{C}|) + \frac{1}{2\sigma^2} (\mathbf{y} - \mathbf{1}\boldsymbol{\beta})^T \mathbf{C}^{-1} (\mathbf{y} - \mathbf{1}\boldsymbol{\beta}) \right) \quad (3.27)$$

where $\log(\cdot)$ is the natural logarithm, $\mathbf{1}$ is an $n \times 1$ vector of ones, and \mathbf{C} is the $n \times n$ correlation matrix with its $(i, j)^{th}$ element $C_{ij} = r(\mathbf{x}_i, \mathbf{x}_j)$ for $i, j = 1, \dots, n$. Setting the partial derivatives with respect to $\boldsymbol{\beta}$ and σ^2 to zero yields:

$$\hat{\boldsymbol{\beta}} = [\mathbf{1}^T \mathbf{R}^{-1} \mathbf{1}]^{-1} \mathbf{1}^T \mathbf{C}^{-1} \mathbf{y} \quad (3.28)$$

$$\hat{\sigma}_v^2 = \frac{1}{n} (\mathbf{y} - \mathbf{1}\hat{\boldsymbol{\beta}})^T \mathbf{C}^{-1} (\mathbf{y} - \mathbf{1}\hat{\boldsymbol{\beta}}) \quad (3.29)$$

Substituting these values into Eq. (3.27) and eliminating the constants:

$$\hat{\boldsymbol{\omega}} = \underset{\boldsymbol{\omega}}{\operatorname{argmin}} n \log(\hat{\sigma}_v^2) + \log(|\mathbf{C}|) = \underset{\boldsymbol{\omega}}{\operatorname{argmin}} L \quad (3.30)$$

By numerically minimizing L in Eq. (3.30) one can find $\hat{\boldsymbol{\omega}}$. Many global optimization methods such as pattern searches (Audet & Dennis, 2002), and particle swarm optimization (Toal et al., 2011) have been employed to solve for $\hat{\boldsymbol{\omega}}$ in Eq. (3.30) (Bessa et al., 2017; Hassaninia et al., 2017). To guarantee global optimality in this case, the optimization is done numerous times with different initial guesses. It is noted that, in practice, the search space of ω_i is generally limited to $[-20, 5]$ rather than $(-\infty, \infty)$ since the correlation exponentially changes as a function of ω_i .

Upon completion of MLE, the following closed-form formula can be used to predict the response at any \mathbf{x}^* :

$$\hat{y}(\mathbf{x}^*) = \hat{\boldsymbol{\beta}} + \mathbf{g}^T(\mathbf{x}^*)\mathbf{V}^{-1}(\mathbf{y} - \mathbf{1}\hat{\boldsymbol{\beta}}) \quad (3.31)$$

where $\mathbf{g}(\mathbf{x}^*)$ is an $n \times 1$ vector with its i^{th} element $c(\mathbf{x}_i, \mathbf{x}^*) = \hat{\sigma}_v^2 r(\mathbf{x}_i, \mathbf{x}^*)$, \mathbf{V} is the covariance matrix with its $(i, j)^{th}$ element $\hat{\sigma}^2 r(\mathbf{x}_i, \mathbf{x}_j)$, and $\mathbf{y} = [y_1, \dots, y_n]^T$ are the responses in the training dataset, which is built by computing outputs \mathbf{y} , for n helical needle configurations. The posterior covariance between the responses at the two inputs \mathbf{x}^* and \mathbf{x}' reads:

$$cov(\mathbf{y}^*, \mathbf{y}') = c(\mathbf{x}^*, \mathbf{x}') - \mathbf{g}^T(\mathbf{x}^*)\mathbf{V}^{-1}\mathbf{g}(\mathbf{x}') + \mathbf{h}^T(\mathbf{1}^T\mathbf{V}^{-1}\mathbf{1})^{-1}\mathbf{h} \quad (3.32)$$

where $\mathbf{h} = (\mathbf{1} - \mathbf{1}^T\mathbf{V}^{-1}\mathbf{g}(\mathbf{x}'))$.

If the training dataset has multiple outputs, such as in the current scenario, one may fit either a single-response GP emulator to each response or a multi-response GP to all the responses. The procedure from Conti et al. (Conti et al., 2009) was adopted, and the above formulations were extended to simulators with q responses by placing a constant mean for each response (i.e., $\boldsymbol{\beta} = [\beta_{(1)}, \dots, \beta_{(q)}]^T$) and employing the separable covariance function:

$$cov(\xi(\mathbf{x}), \xi(\mathbf{x}')) = c(\mathbf{x}, \mathbf{x}') = \boldsymbol{\Sigma} \otimes r(\mathbf{x}, \mathbf{x}') \quad (3.33)$$

where \otimes denotes the Kronecker product and $\boldsymbol{\Sigma}$ is the $q \times q$ process covariance matrix with its off-diagonal elements representing the covariance between the corresponding responses at any fixed \mathbf{x} . The MLE approach described above can also be applied to multi-response datasets in which case σ will be replaced with $\boldsymbol{\Sigma}$ (Bayarri et al., 2007; Conti & O'hagan, 2010).

Finally, GPs can address noise and smooth the data (i.e., avoid interpolation) via the so-called nugget or jitter parameter, δ , in which case \mathbf{C} is replaced with $\mathbf{C}_\delta = \mathbf{C} + \delta\mathbf{I}_{n \times n}$. If δ is used, the estimated (stationary) noise variance in the data would be $\delta\hat{\sigma}_v^2$ (Bostanabad et al., 2018a).

3.4.2 GP Application to Helical Needle Geometry

The Gaussian Process model will be adopted to estimate the resulting cutting angles for given angles of the helical needles. The model is characterized by 2 inputs, which include the cone angle of the conical helix (ψ) and the inclination angle of the needle (φ), and 7 outputs, which include the length of the needle's cutting edge (l_c) and the minimum and maximum values of the cutting angles (λ, θ, α). This model was formulated by adopting a training data set composed of 25 helical needle configurations. For each needle configuration, which was obtained from a different combination of the inputs values, the 7 outputs were computed by following the same procedure described in Section (3.1). The resulting closed-form formula (Eq. (3.31)) allows the prediction of the response \hat{y} at any input \mathbf{x}^* , within a 95% confidence interval. The following plots (Fig. 3.17) show the value of one of the predicted outputs, such as the cutting length l_c , at each combination of the inputs. Further, it is possible to adopt Eq. (3.31) to formulate the objective function and calculate the input angles depending on the desired goal. For instance, it is possible to choose an objective function in order to design a helical needle characterized by a minimal cutting length. In this scenario, the objective function will be equal to one of the outputs, such as the cutting length (3.34). By minimizing the objective function, it is possible to obtain the inputs which allow for the design of the desired geometry.

$$\min(F) = Y(l_c) \quad (3.34)$$

In a similar way, it is possible to create an objective function with the goal of identifying a helical needle geometry, characterized by a minimum included angle, θ , and a maximum inclination angle, λ :

$$\min(F) = \frac{Y(\theta)}{Y(\lambda)} \quad (3.35)$$

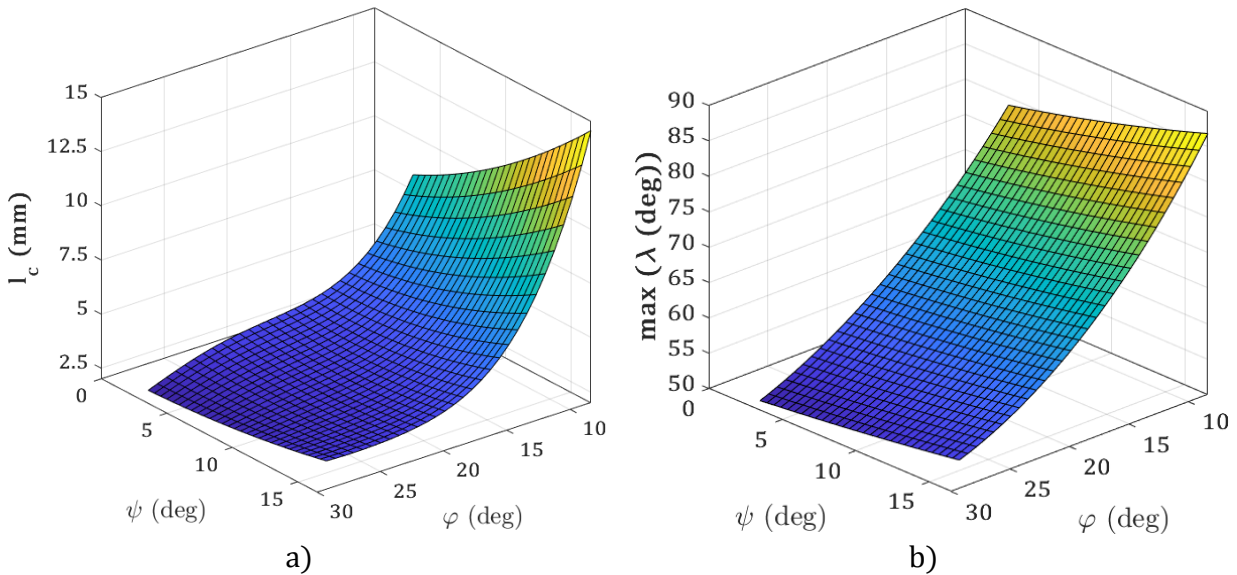


Figure 3.17. (a) Cutting length (l_c) and (b) the maximum value of the inclination angle (λ) for different combinations of inputs, as predicted by the GP model.

The following table (Table 3.4) shows the different values of the inputs, depending on the objective function that was formulated.

Table 3.4. Objective function F , with the computed values for the input angles (ψ, φ).

Objective Function (F)	ψ	φ
$\min(\theta)$ AND $\max(\lambda)$	9.57	16.55
$\min(l_c)$ AND $\max(\lambda)$	20.65	11
$\min(l_c)$ AND $\min(\theta)$	13.32	8.95

Therefore, it is possible to determine the optimal helical geometry, depending on the composition of the objective function.

3.5 Conclusions on Helical Needles

For the first time, a biopsy needle characterized by a three-dimensional cutting edge was conceived and demonstrated by developing a helical geometry. The fundamental objective of this study was to provide the framework for biomedical engineers to develop needles characterized by any 3D shape and better understand their geometry and effectiveness.

The helical geometry was applied to a 14-gauge cannula, which is usually adopted in breast biopsies. The mathematical models were resolved to compute the main cutting angles and the fracture forces related to helical needles. The proposed methodologies can be applied to virtually any needle geometry. The analytical results were compared with the ones related to one-plane bevel needles, which represent the most common geometry in practice. Furthermore, a helical geometry was manufactured and tested on phantom tissue for translational and rotational insertions. The measurement of the cutting forces demonstrates that the helical geometry leads to a 20% decrease of the axial and translational forces. Moreover, several cutting tests were performed at different rotational/translational ratios, and they show a reduction of the perpendicular and tangential fracture forces for $S > 1.5$. The experimental results were mostly aligned with the analytical estimation of the fracture forces that were obtained from the formulated model for the helical geometry.

In addition, a physics-informed Gaussian process metamodel was adopted to investigate the sensitivity of needle cutting length and main cutting angles ψ and φ . The results show that it is possible to predict the main helical needle cutting angles, for any combination of the inputs, and, therefore, optimize the helical geometry by formulating a proper objective function.

Further research is needed to develop novel 3D shapes for the needle's cutting edge. Optimization of the helical geometry—to lower the cutting forces by considering parameters

such as the pitch of the helix, p_h — is worth exploring as well. The optimization of the helical shape requires a separate investigation to assess how different combinations of these three parameters (ψ , φ , and p_h) affect the resulting rake face and needle cutting edge geometry.

The results of this study can be utilized to improve breast and bone marrow biopsies, and they can be extended to different biopsy examinations where a hollow needle is adopted to collect tissue samples.

4 Soft Tissue Characterization

This chapter reports on the characterization of polyvinyl chloride (PVC) tissue, which is commonly used to mimic human skin. This phantom material is commonly adopted in biomedical studies to investigate the behavior of medical devices such as biopsy needles and surgical scalpels for various diagnostic and therapeutic procedures. The correct assessment of the mechanical properties of this phantom tissue is crucial in order to properly mimic the biological tissue and foster the studies in this field.

Specifically, this phantom material has been adopted by Podder et al. (Podder et al., 2005a), who used polyvinylchloride (PVC) – a liquid plasticizer as phantom material. In their work, they utilized PVC tissue to analyze the impact of the geometry of brachytherapy needles on their insertion accuracy. Moore et al. (2011) also used a similar material in their studies. They investigated the impact of the blade's inclination and rake angles on the cutting force in hollow needle tissue cutting.

Despite the wide-ranging adoption of this material in previous literature, very few studies have been directed towards the experimental characterization of its mechanical behavior and its correlation with computational and experimental measurements when this phantom tissue is in use. In this study, we perform the characterization of phantom tissue by uniaxial tests, and we proceed to the formulation of a FEM model in order to predict the insertion forces for hollow biopsy needle insertions.

The phantom tissue used is composed of 8116SS plastic (P) mixed with 4116S Plastic Softener (S) in different ratios, S/P , equal to 0, 0.25, 0.5, 1. Uniaxial tests were performed on a universal material testing machine, and a 3D digital image correlation (DIC) system was used to

detect the strain in the tissue specimen. Data coming from the tissue characterization was used to calibrate a 3D FEM model to predict the cutting force during the insertion of core biopsy needles. The phantom tissue was modeled as a hyperelastic material using several constitutive models, and experimental tests were performed to assess the reliability of the proposed tissue characterization method. This chapter has benefited from several discussions with Newell Moser.

4.1 Experimental Methods for Uniaxial Tests

4.1.1 Tension Test

Tension tests were performed on the produced phantom tissue since soft solids tend to fail under critical tensile stresses (Reyssat et al., 2012). The tests were conducted on a universal testing machine MTS Sintech 20/G, which was equipped with a 150 g capacity load cell (Fig. 4.1). The crosshead of the machine was moved at 1 mm/s, which approximately corresponds to the strain rates that characterize tissue deformation during needle insertion. The specimens were prepared according to ASTM D-412 C. The 3D digital image correlation (DIC) method was used to measure large strains. To this end, a random speckle pattern was created on the surface of the specimen by applying a thin coating of white and black spray paint. A high-resolution CCD camera (CMLN-13S2M-CS, Point Grey Research) and a 35 mm compact fixed focal length lens (Techspec series, Edmund Optics) were used to capture images of the deforming specimens. An example of a deformed gel phantom specimen at the beginning of a tension test and prior to tensile fracture is shown in Fig. 4.1.

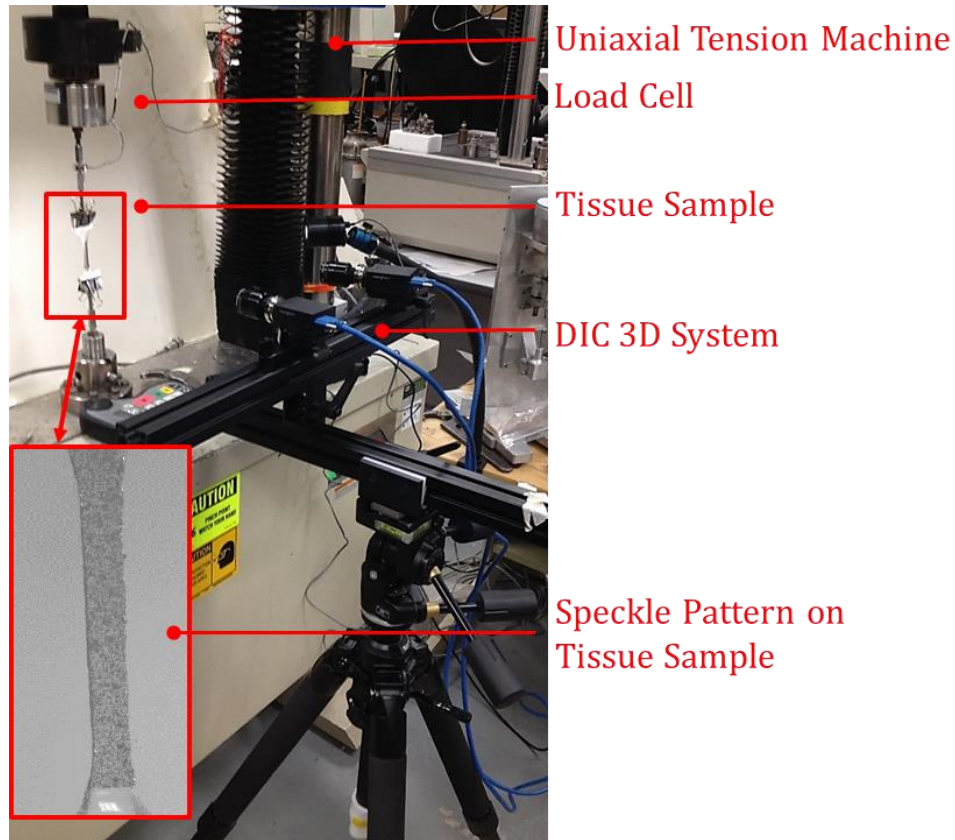


Figure 4.1. Uniaxial tension testbed with the DIC 3D System.

The strain was analyzed using the VIC software tool DIC-3D (provided by Correlated Solutions, Inc.) (Mguil-Touchal et al., 1997).

4.1.2 Compression Test

Compression tests were run on the same machine (MTS Sintech 20/G) as the tension tests. The specimens with a diameter of 38 mm and a length of 30 mm were prepared by using a cylindrical mold (Fig. 4.2). Nylon sheets were positioned between the top and the bottom surfaces of the specimen and the uniaxial machine crossheads to reduce friction in the contact zone.

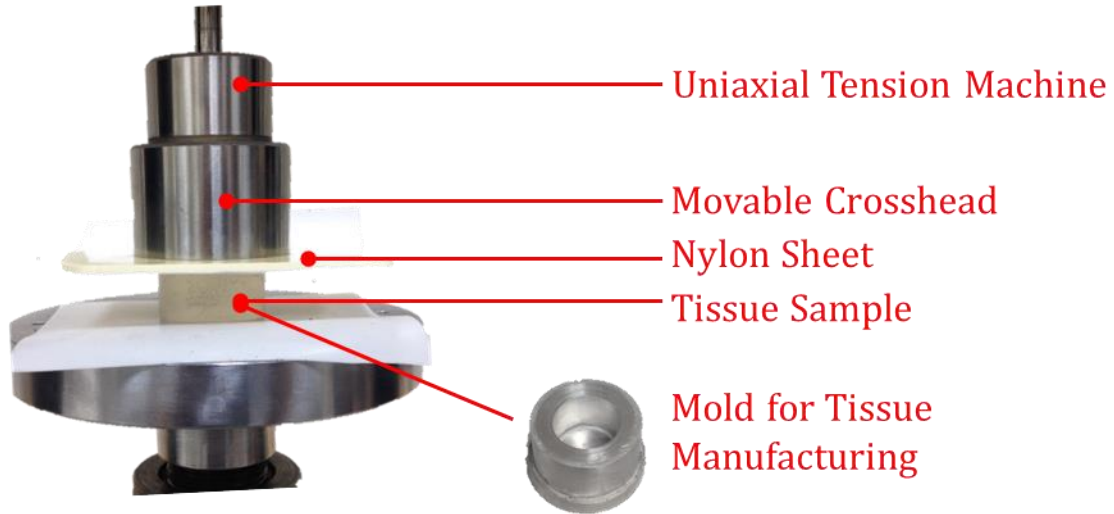


Figure 4.2. Setup for the compression test and related mold.

The crosshead compressed the tissue at the same speed as the tension tests (1mm/s) until an engineering strain of 70% was reached or the specimen fractured. The plots of the stress and strain curves obtained from the tension and compression tests will be shown and discussed in Section 4.2.3.

4.2 Soft Tissue Constitutive Models

During medical procedures, soft tissues usually experience large deformations and displacements before fracture initiates. For this reason, their mechanical behavior is often modeled by adopting hyperelastic models, where the stresses (σ_{ij}) are expressed as a function of the strain energy density function (U), and the material is considered incompressible. The Cauchy stress can be calculated as (Bower, 2010):

$$\sigma_{ij} = 2 \left[\left(\frac{\partial U}{\partial I_1} + I_1 \frac{\partial U}{\partial I_2} \right) B_{ij} - \left(I_1 \frac{\partial U}{\partial I_1} + 2I_2 \frac{\partial U}{\partial I_2} \right) \frac{\delta_{ij}}{3} - \frac{\partial U}{\partial I_2} B_{ik} B_{kj} \right] + p \delta_{ij} \quad (4.1)$$

where p is the hydrostatic stress, B is the Left Cauchy-Green deformation tensor and I_1 and I_2 are its first and second invariants. Since material characterization is performed by means of uniaxial tests, the experimental data are available as engineering stress (P_{11}) and strain (e_{11}), which can be converted to Cauchy stresses (σ_{11}) and stretches (λ_{11}) (Reddy, 2008):

$$\sigma_{11} = P_{11}(e_{11} + 1) \quad (4.2)$$

$$\lambda_{11} = e_{11} + 1 \quad (4.3)$$

During uniaxial tests, the deformation tensor F is:

$$\mathbf{F} = \begin{bmatrix} \lambda_{11} & 0 & 0 \\ 0 & \frac{1}{\sqrt{\lambda_{11}}} & 0 \\ 0 & 0 & \frac{1}{\sqrt{\lambda_{11}}} \end{bmatrix} \quad (4.4)$$

while the Left Cauchy-Green deformation tensor is obtained as (Reddy, 2008):

$$\mathbf{B} = \mathbf{F} \cdot \mathbf{F}^T \quad (4.5)$$

During uniaxial tests, the stresses σ_{22} and σ_{33} are equal to zero, which allows the calculation of the hydrostatic stress p (Eq. (4.6)) as:

$$p = -2 \left[\left(\frac{\partial U}{\partial I_1} + I_1 \frac{\partial U}{\partial I_2} \right) B_{33} - \left(I_1 \frac{\partial U}{\partial I_1} + 2I_2 \frac{\partial U}{\partial I_2} \right) \frac{1}{3} - \frac{\partial U}{\partial I_2} B_{3k} B_{k3} \right] \quad (4.6)$$

The strain energy density function (U) is defined in a different way for each material model. In this study, the following popular hyperelastic models will be considered: (i) Arruda-Boyce model, and (ii) Ogden model. For each material model, the formula to calculate the Cauchy stress in the axial direction (σ_{11}) will be identified to allow the determination of the material constants by fitting the results to the experimental data points obtained from the uniaxial tests (Section 4.2.3).

4.2.1 Arruda-Boyce Model

The Arruda-Boyce model is a hyperelastic constitutive model that is based on the statistical representation of a material—usually rubber—characterized by a cubic volume element with eight chains along the diagonal direction. Its strain energy density function can be expressed by using the first five terms of the inverse Langevin function (Bower, 2010):

$$\bar{U} = \mu \left(\sum_{i=1}^5 \frac{C_i}{\lambda^{2i-2}} (I_1^i - 3^i) \right) + \frac{1}{D} \left(\frac{J^2 - 1}{2} - \ln(J) \right) \quad (4.7)$$

where μ and D are material parameters and the constants C_i are equal to:

$$C_1 = \frac{1}{2}, C_2 = \frac{1}{20}, C_3 = \frac{11}{1050}, C_4 = \frac{19}{7000}, C_5 = \frac{519}{673750} \quad (4.8)$$

For incompressible materials, J is equal to 1, so Eq. (4.7) becomes:

$$U = \mu \left(\sum_{i=1}^5 \frac{C_i}{\lambda^{2i-2}} (I_1^i - 3^i) \right) \quad (4.9)$$

The derivatives of U can now be defined as:

$$\frac{\partial U}{\partial I_1} = \mu \left(\sum_{i=1}^5 \frac{(i-1)C_i}{\lambda^{2i-2}} I_1^{i-1} \right) \quad (4.10)$$

$$\frac{\partial U}{\partial I_2} = 0 \quad (4.11)$$

The hydrostatic stress (Eq. (4.6)) can then be written as:

$$p = -2 \left[\left(\frac{\partial U}{\partial I_1} \right) B_{33} - \frac{1}{3} \left(I_1 \frac{\partial U}{\partial I_1} \right) \right] \quad (4.12)$$

The Cauchy stress (Eq.(4.2)) in the axial direction (σ_{11}) is:

$$\sigma_{11} = 2 \frac{\partial U}{\partial I_1} [B_{11} - B_{33}] \quad (4.13)$$

4.2.2 Ogden Model

The Ogden model is a hyperelastic constitutive model where the strain energy density function is directly expressed as a function of the principal stretches (“Abaqus 6.13 Online Documentation,” 2013; Ogden, 1972):

$$U = \sum_{i=1}^N \frac{2\mu_i}{\alpha_i^2} (\lambda_1^{\alpha_i} + \lambda_2^{\alpha_i} + \lambda_3^{\alpha_i} - 3) + \sum_{i=1}^N \frac{1}{D_i} (J - 1)^{2i} \quad (4.14)$$

where N , μ_i , α_i and D_i are material properties. For incompressible materials, J is equal to 1, and the Cauchy stress can be obtained from:

$$\sigma_i = \lambda_i \frac{\partial U}{\partial \lambda_i} - p \quad (4.15)$$

During uniaxial tests the principal stresses σ_2 and σ_3 are equal to zero, while the principal stretches are equal to: $\lambda_2 = \lambda_3 = \lambda_1^{-\frac{1}{2}}$. The hydrostatic stress p can be calculated as:

$$p = \lambda_3 \frac{\partial U}{\partial \lambda_3} = \sum_{i=1}^N \frac{2\mu_i}{\alpha_i} \left(\lambda_1^{-\frac{1}{2}\alpha_i} \right) \quad (4.16)$$

The Cauchy stress in the axial direction (σ_1) can then be written as:

$$\sigma_1 = \sum_{i=1}^N \frac{2\mu_i}{\alpha_i} \left(\lambda_1^{\alpha_i} - \lambda_1^{-\frac{1}{2}\alpha_i} \right) \quad (4.17)$$

4.2.3 Identification of Material Constants

For each PVC phantom tissue, each one characterized by a different mixture ratio (Section 2.3.3), the experimental data from the uniaxial tests were fitted with the material models (described in the previous section) by using the least squares method. For each material model, the material constants, the correlation coefficient R^2 and the root mean square deviation

(*RMSE*) were determined. Figure 4.3 shows the uniaxial test curves obtained from the samples adopted for the tension and compression tests.

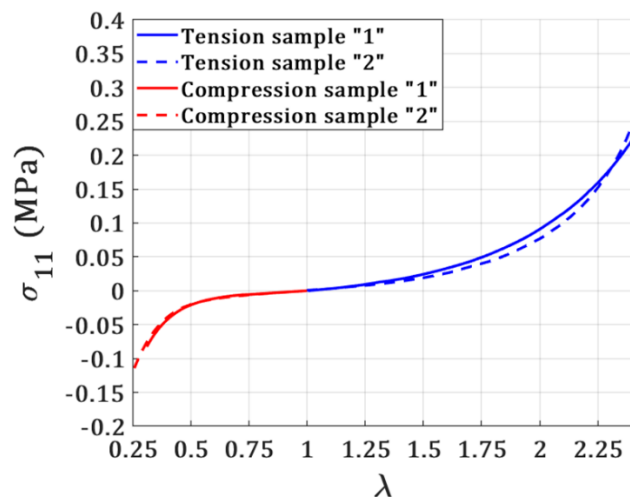


Figure 4.3. True Cauchy stress (σ_{11}) vs. stretches (λ_1) in the axial direction for a mixture with an *S/P* ratio equal to 0, coming from different samples.

Figure 4.4 shows the uniaxial test curves with the fitted material model for one of the phantom tissue mixtures.

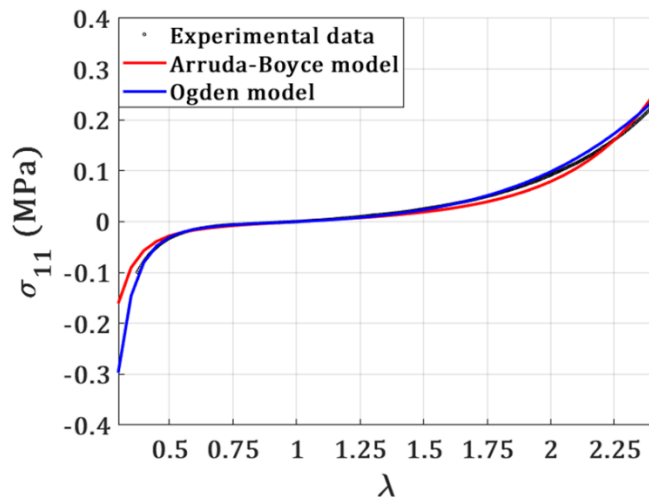


Figure 4.4. True Cauchy stress (σ_{11}) vs. stretches (λ_1) in the axial direction for a mixture with an *S/P* ratio equal to 0.

The material constants and the fitting coefficients are presented in Table 4.1 for one of the phantom tissue mixtures, while the other plots and tables are given in Appendix A. The Arruda-Boyce model fits the experimental data better, and its material parameters will be adopted later for the elaboration of analytical models and FEM simulations.

Table 4.1. Material constants and fitting coefficients for each material model for a mixture with an S/P ratio equal to 0.

Model	Material Constants	R ²	RMSE
<i>Arruda – Boyce</i>	$\mu = 0.00418$ $\lambda = 1.15$	0.967	0.0298
<i>Ogden</i>	$\mu_1 = -0.0255$ $\alpha_1 = -3.91$ $\mu_2 = 0.0088$ $\alpha_2 = 4.74$ $\mu_3 = 0.0249$ $\alpha_3 = -4.09$	0.9606	0.0328

4.3 Analytical Force

In this section, the soft tissue constitutive models will be verified by estimating the value of the cutting forces from an analytical standpoint. The material parameters obtained in Section 4.2 will be adopted to calculate the force values when the needle is inserted, both with and without rotation. The results will be compared with experimental results obtained by using the testbed introduced in Section 2.3.2.

4.3.1 Needle Insertion without Rotation

During Phase I (Section 2.2), the needle is first subjected to an axial force due to the elastic tissue deformation (F_{Vel}), which can be calculated as:

$$F_{Vel} = \sigma_1 A_t \quad (4.18)$$

where σ_1 represents the Cauchy stress in the axial direction and A_t represents the area of the tissue that is subjected to the elastic deformation. In this scenario, the overall tissue deformation is approximated with the deformation of a tissue column characterized by a radius (r_t), which is approximately equal to 2~3 times ($\beta = 2\sim 3$) the internal radius of the needle (Fig. 2.1):

$$A_t = \pi r_t^2 = \pi \left(\beta \frac{d_i}{2} \right)^2 = \pi \beta^2 \frac{d_i^2}{4} \quad (4.19)$$

The Cauchy stress in the axial direction (σ_1) can be obtained from the Arruda-Boyce model by adopting Eqs. (4.13), (4.10), (4.5):

$$\sigma_{11} = 2\mu \left(\sum_{i=1}^5 \frac{(i-1)C_i}{\lambda^{2i-2}} I_1^{i-1} \right) \left[\frac{\lambda^3 - 1}{\lambda} \right] \quad (4.20)$$

where the stretches are calculated as the ratio between the final length of the compressed tissue column (l_{fin}) and the original length (l_{init}). Further, the final length of the compressed tissue column (l_{fin}) can be expressed as the difference between the initial length of the tissue (l_{init}), and the distance covered from the needle tip in the axial direction (represented by the coordinate x):

$$\lambda = \frac{l_{fin}}{l_{init}} = \frac{l_{init} - x}{l_{init}} \quad (4.21)$$

By adopting Eqs. (4.18)-(4.20), the axial force (F_{Vel}) can be calculated as:

$$F_{Vel} = 2\mu \left(\sum_{i=1}^5 \frac{(i-1)C_i}{\lambda^{2i-2}} I_1^{i-1} \right) \left[\frac{\lambda^3 - 1}{\lambda} \right] \left(\pi \beta^2 \frac{d_i^2}{4} \right) \quad (4.22)$$

Figure 4.5 shows the comparison between the experimental insertion force profiles and the ones computed by adopting Eq. (4.22). The behavior of the axial force is similar to the one observed in the experiments, although the analytical formulation simplifies the final

configuration of the deformed tissue, by approximating it to the deformation of a tissue column. For this reason, the deformation of the tissue will be further investigated in Section 4.4 by 3D FEM simulations.

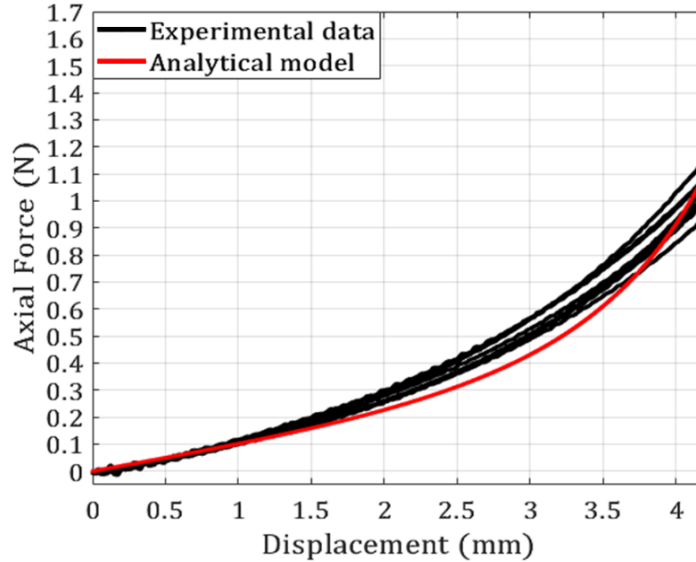


Figure 4.5. Comparison of axial forces obtained from the analytical model with the experimental measurements performed on the testbed (Section 2.3.2). The cannula was moving at the same axial speed as during the material testing (1 mm/s).

4.3.2 Needle Insertion with Rotation

When the slicing motion is applied to the biopsy needle, the targeted tissue is subjected to compression and torsion. The material equilibrium configuration (Lai et al., 2010) when considering a spherical coordinate system, can be written as:

$$r_{sph} = \lambda_1 R_{sph} \quad \theta_{sph} = \Theta_{sph} + KZ_{sph} \quad z_{sph} = \lambda_3 Z_{sph} \quad (4.23)$$

where K represents the amount of shear, while $r_{sph}, \theta_{sph}, z_{sph}$ represent the spatial coordinates and $R_{sph}, \Theta_{sph}, Z_{sph}$ represent the material coordinates. The axial (F_{vel}) and tangential forces

(F_{Hel}) due to the elastic deformation of the tissue can be calculated from its state of stress, where the tensors \mathbf{F} and \mathbf{B} can be expressed as (Lai et al., 2010):

$$\mathbf{F} = \begin{bmatrix} \lambda_1 & 0 & 0 \\ 0 & \lambda_1 & r_{sph}K \\ 0 & 0 & \lambda_3 \end{bmatrix} \quad (4.24)$$

$$\mathbf{B} = \begin{bmatrix} \lambda_1^2 & 0 & 0 \\ 0 & \lambda_1^2 + r_{sph}^2 K^2 & r_{sph}K\lambda_3 \\ 0 & r_{sph}K\lambda_3 & \lambda_3^2 \end{bmatrix} \quad (4.25)$$

Since the material is considered as incompressible, the principal stretches are equal to: $\lambda_1 = \lambda_2 = \lambda_3^{-\frac{1}{2}}$. The Cauchy stresses can be obtained by adopting Eq. (4.1) and Eq. (4.11):

$$\sigma_{ij} = 2 \left[\frac{\partial U}{\partial I_1} B_{ij} - \left(I_1 \frac{\partial U}{\partial I_1} \right) \frac{\delta_{ij}}{3} \right] + p \delta_{ij} \quad (4.26)$$

where the value of p , can be simplified in the equations, by considering the following equilibrium equations (Lai et al., 2010):

$$\frac{\partial \sigma_{rr}}{\partial r} + \frac{\sigma_{rr} - \sigma_{\theta\theta}}{r_{sph}} = 0, \quad \frac{\partial \sigma_{\theta\theta}}{\partial \theta_{sph}} = 0, \quad \frac{\partial \sigma_{zz}}{\partial z_{sph}} = 0 \quad (4.27)$$

which allows the determination of the following stresses:

$$\sigma_{zz} = \frac{\partial U}{\partial I_1} (2\lambda_3^2 - 2\lambda_1^2 - r_{sph}^2 K^2) \quad (4.28)$$

$$\sigma_{\theta z} = 2 \left(\frac{\partial U}{\partial I_1} \right) r_{sph} K \lambda_3 \quad (4.29)$$

These equations can be used to calculate the axial force (F_{Vel}) and the twisting torque (T_{el}):

$$F_{Vel} = \int_0^{r_t} \sigma_{zz} 2\pi r_{sph} dr_{sph} \quad (4.30)$$

$$T_{el} = \int_0^{r_t} r_{sph} \sigma_{\theta z} 2\pi r_{sph} dr_{sph} \quad (4.31)$$

which can be simplified as:

$$F_{Vel} = \pi\mu \left(\sum_{i=1}^5 \frac{(i-1)C_i}{\lambda^{2i-2}} I_1^{i-1} \right) \left(2\lambda_3^2 r_t^2 - 2\lambda_1^2 r_t^2 - \frac{r_t^4 K^2}{2} \right) \quad (4.32)$$

$$T_{el} = \pi\mu K \left(\sum_{i=1}^5 \frac{(i-1)C_i}{\lambda^{2i-2}} I_1^{i-1} \right) \lambda_3 r_t^4 \quad (4.33)$$

The tangential force (F_{Hel}) can be obtained by dividing T_{el} by the radius of the tissue that is deformed. However, it is difficult to estimate the amount of shear K , since this deformation takes place in the tangential direction. For this reason, F_{Hel} can be approximated by multiplying the axial force F_{Vel} by the Coulomb friction coefficient μ_d :

$$F_{Hel} = F_{Vel} \mu_d \quad (4.34)$$

Figure 4.6 shows the comparison between the experimental and the analytical forces when the Arruda Boyce Model is used.

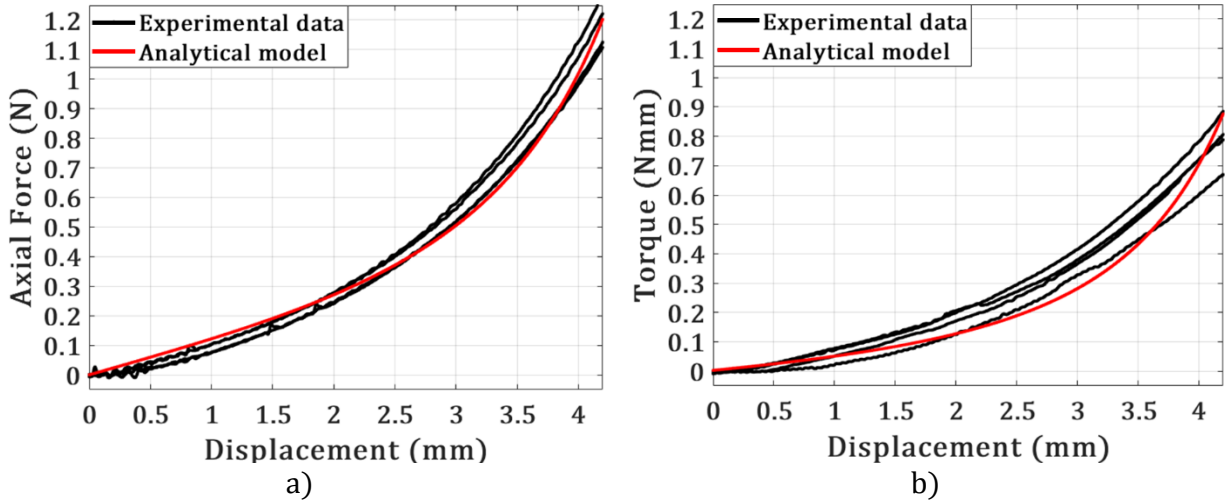


Figure 4.6. (a) Comparison of axial and (b) tangential forces obtained from the analytical model with the experimental measurements performed on the testbed (Section 2.3.2). The cannula was moving at the same axial speed as during the material testing (1 mm/s).

The behavior of the axial force obtained from the analytical model is similar to the one observed in the experiments. On the other hand, the behavior of the tangential force presents some discrepancies with respect to the analytical formulation, although it is able to capture the overall trend. For this reason, the deformation of the tissue, when slicing motion is applied, will be further investigated in Section 4.4 by adopting 3D FEM simulations.

4.4 Finite Element Model Validation for Hollow Needles

In this section, the soft tissue constitutive models will be verified by performing several computational studies related to the insertion of hollow needles into soft tissue. The material parameters obtained in Section 4.2 will be adopted to formulate the finite element simulations, and the results will be compared with experimental results obtained by using the testbed introduced in Section 2.3.2.

4.4.1 Hollow Needle Insertion without Rotation

4.4.1.1 3D Finite Element Model

In this section, a 3D finite element model is formulated with ABAQUS to simulate the interaction between a hollow needle and soft tissue, while it is pressed against the tissue, without any rotation (an example of the input file is given in Appendix B1). In this computational study, the axial reaction force computed at the needle will be compared with the one experimentally measured.

The hollow needle was described as a discrete rigid body. Its geometry was characterized by an outside diameter of 2.4 mm (d_e), an inside diameter of 2 mm (d_i), a bevel length of 0.6 mm (l), a tip radius of 15 μm and an included angle (θ) of 13° at the cutting edge (Fig. 4.7).

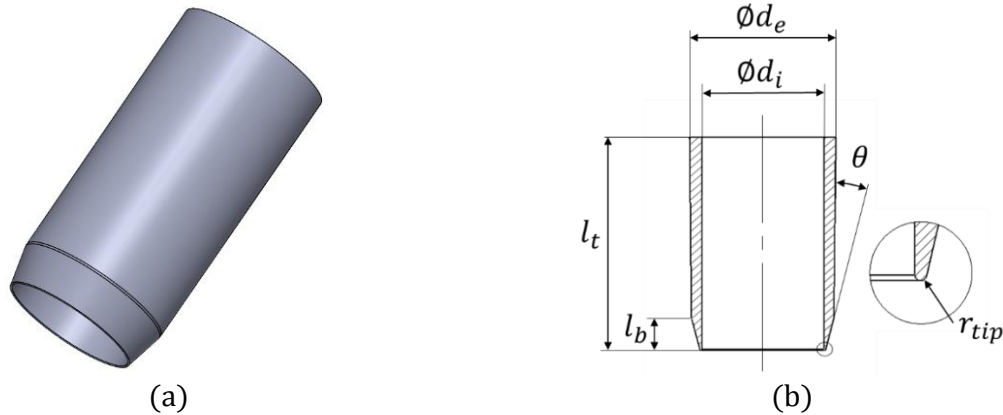


Figure 4.7. Schematics of a BP (or hollow needle) tip: (a) CAD model and (b) cross-section showing the inner diameter (d_i), outer diameter (d_e), total length (l_t), bevel length (l_b), cutting tip radius (r_{tip}) and included angle (θ).

A translational motion was applied to the cannula that moves parallel to the thickness of the tissue, and it is constrained with respect to the remaining translational and rotational motions. The mesh of the hollow needle was composed of three dimensional triangular (R3D3) and quadrilateral (R3D4) elements. Specifically, the finite element mesh of the commercial BP mesh was realized with HyperMesh, and it was built with 37,255 nodes, 37,105 R3D4 elements, and 24 R3D3 elements. The soft tissue block was considered as a deformable body, and it was represented by a cylinder with a radius of 10 mm and a thickness of 7.5 mm. Since the model is symmetric with respect to the xz - and yz -planes, a quarter of the cylinder with symmetric boundary conditions was used in the simulations (Fig. 4.8) as the soft tissue. The base of the tissue was completely constrained, while the external cylindrical surface was assumed to be free.

The mesh was built by adopting three-dimensional eight-node hexahedral elements (C3D8) and three-dimensional six-node wedge elements (C3D6).

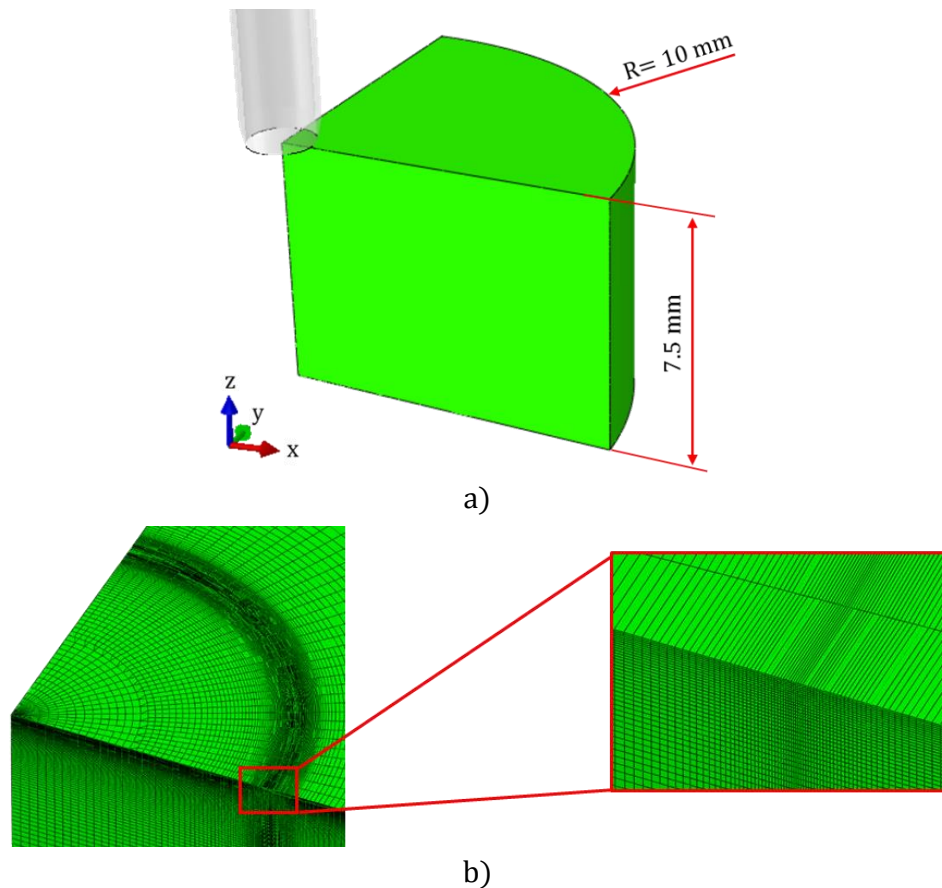


Figure 4.8. 3D Finite element model of hollow needle insertion. The geometry of the cannula and of the soft tissue is shown in the 3D view (a). The mesh is refined in the proximity of the cutting-edge area (b).

The finite element mesh consisted of 920,345 nodes, 882,900 C3D8 elements and 5,400 C3D6 elements. The mesh consisted of 325 elements along the radius, 36 elements around the circular edge, and 151 elements through the thickness of the block. In the proximity of the cutting area, which interacts with the hollow needle, the number of elements has been consistently increased. In fact, to define the stress gradient in the tissue being cut by a cannula with a radius at the tip of

15 μm , the mesh of the tissue was composed of approximately 1 μm elements in the tissue-cutting edge interaction zone (Fig. 4.8b).

The tissue was modeled by hyperelastic constitutive models and, in particular, the Arruda-Boyce model, where the material constants c_1 , λ_m , and D_1 are equal to 0.00418, 1.15, and 2.14, respectively (Table 4.1). The material constant D_1 can be obtained from the Poisson's ratio of the material, η . For incompressible materials, η can be considered equal to 0.5. However, in Abaqus/Explicit, this constraint must be relaxed for calculation purposes, so a Poisson's ratio equal to 0.495 was considered. Because of the large number of elements, the simulations were performed using the explicit algorithm, which is commonly used to simulate dynamic processes. The insertion process studied in this section can be considered a quasi-static process, given the slow speed at which the needle is moving (1~5 mm/s). In this scenario, specific considerations are required when explicit dynamics is used to model quasi-static events. In fact, it would be computationally very expensive to model this process in its natural time scale, since that would require an excessive number of time increments. To counteract this effect, the needle insertion speed was increased by 60 times, and the tissue mass was increased by 200 times, allowing a consistent increase of the time step. These approximations can be implemented as long as the kinetic energy of the tissue is consistently lower than its internal energy. By doing so, the simulation could be completed in 75 hours with 48 CPUs.

During the simulation, the cutting edge of the hollow needle was pushed towards the tissue for 5 mm. Since soft solids can fail under critical tensile stresses (Reyssat et al., 2012), the contour plots related to the 1st principal stresses in the tissue contact zone were observed (Fig. 4.9). Figure 4.9 shows the contour plots of the maximum principal stress when the hollow needle reaches a penetration depth of 1 mm and 5 mm. The stresses are highly localized in the cutting

edge-tissue contact zone, and they are higher at a higher depth. The maximum principal stress is found to assume positive (tensile) values at the higher penetration depth (Fig. 4.9), and it is probably the primary reason for a fracture in soft materials. (Reyssat et al., 2012).

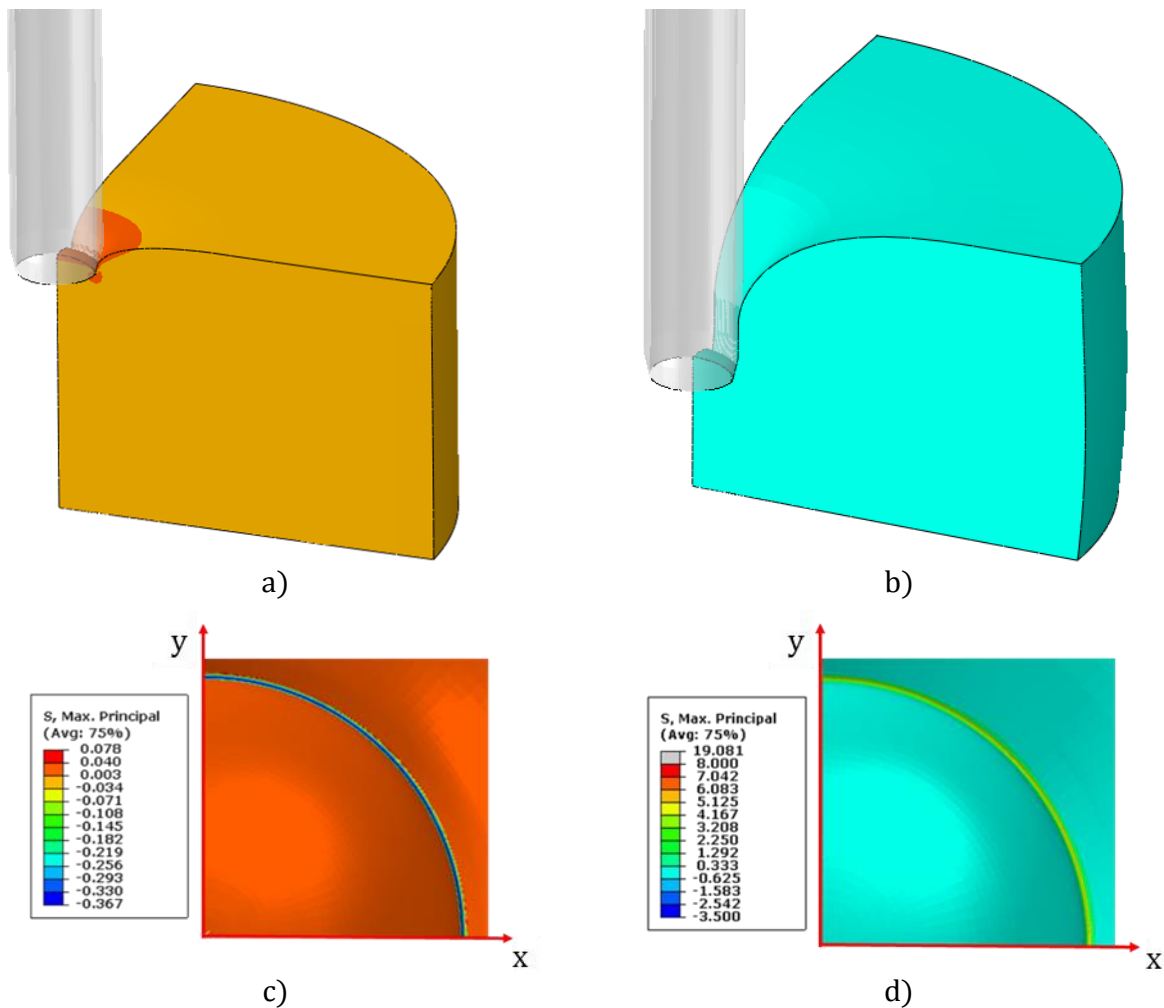


Figure 4.9. (a, c) Contour plots of the maximum principal stress for a cannula inserted to a penetration depth of 1 mm and (b, d) of 5 mm.

Figure 4.10 shows the comparison between the experimental insertion force profiles and the ones computed by finite element simulations. The behavior of the axial force is similar to the one observed in the experiments, although the force values are approximately 20% lower than the

average values obtained from the five experimental force measurements. This discrepancy is due to some of the approximations made to simulate the phenomena. For instance, the material could not be considered perfectly incompressible in the FEM model, while the speed of the needle and the mass of the tissue were significantly increased. Because of the high computational cost of this 3D simulation, a 2D simulation was built, and it will be presented in the next section.

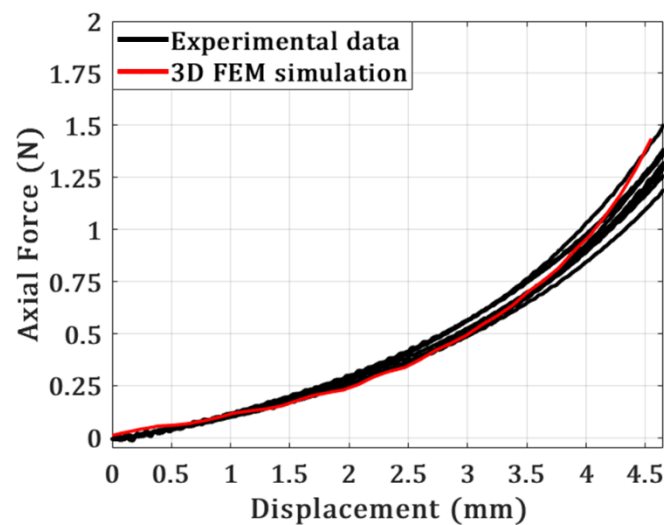


Figure 4.10. Comparison of axial forces obtained from the 3D FEM simulation with the experimental measurements performed on the testbed. The cannula was moving at the same axial speed adopted during the material testing (1 mm/s).

4.4.1.2 2D Finite Element Model

In this section, a 2D finite element model (Fig. 4.11) was formulated with ABAQUS/standard to simulate the interaction between a hollow needle and soft tissue (an example of the input file is given in Appendix B2). The goal is to simulate the same insertion as in Section 4.4.1.1 but using a fraction of the computational cost. The hollow needle was modeled as a rigid analytical surface and, therefore, did not require a mesh. Its geometry and motion were set to be equal to the

geometry of the hollow conical needle used in the experiments and in the previous simulation (Fig.4.7).

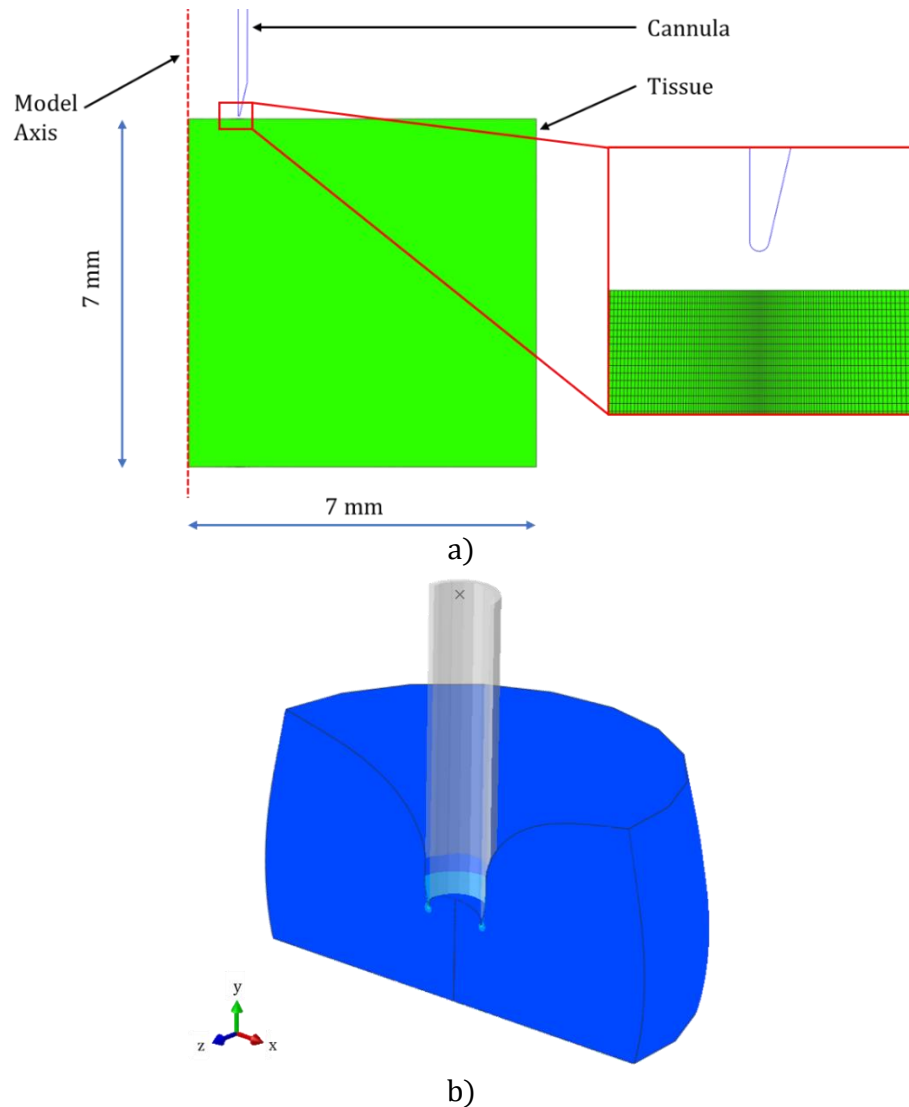


Figure 4.11. 2D Finite element model of hollow needle insertion. The mesh and geometry of the soft tissue are shown in the side view (a). The elements were swept around the simulation axis to provide a 3D view of the simulation (b).

The soft tissue block was considered as a deformable body, and it was represented by a 2D cross-section with a radius of 7 mm and a thickness of 7 mm. The base of the tissue was

completely constrained, while the other surfaces were assumed to be free. The mesh was built by adopting two-dimensional four-node axisymmetric elements (CAX4R). The finite element mesh consisted of 54,540 nodes and 54,058 CAX4R elements. The mesh consisted of 302 elements along the radius and 179 elements through the thickness of the block. The mesh has been designed to be denser where the hollow needle enters in contact with the soft tissue, where the elements have a 2 μm length (Fig. 4.11a). In the simulation, the same material parameters, as in the previous 3D simulation, were used. The Poisson's ratio, η , was considered equal to 0.475, which helps the convergence of the simulation. By adopting a 2D model, the simulation could be completed in only two hours while using 24 CPUs, which is 72 times quicker than the 3D simulation.

Figure 4.12 shows the comparison between contour plots of the maximum principal stress in the region of contact for 3D (Fig. 4.12a) and 2D (Fig. 4.12b) simulations when the hollow needle reaches a penetration depth of approximately 5 mm.

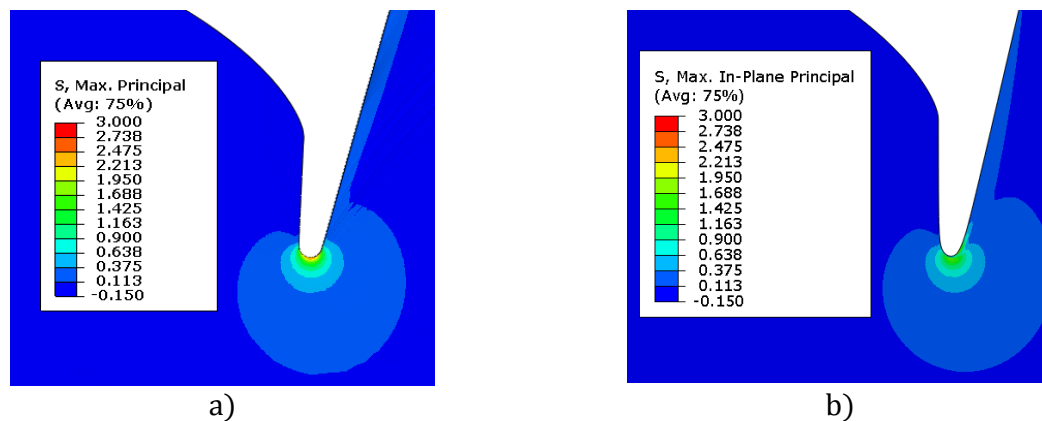


Figure 4.12. Contour plot of the maximum principal stress at the contact zone between the cannula and soft tissue for (a) 3D and (b) 2D FEM model (b).

A further confirmation that the 2D axisymmetric simulation and 3D FEM simulation, presented in Section 4.4.1.1, can provide similar results can be obtained by the comparison between the axial forces at the cannula for the two simulations (Fig. 4.13). Figure 4.13 shows how the 2D FEM simulation provides a force prediction of the cannula axial force, which is approximately 17% lower than the force prediction obtained from the 3D FEM simulation, but for a fraction of the computational cost.

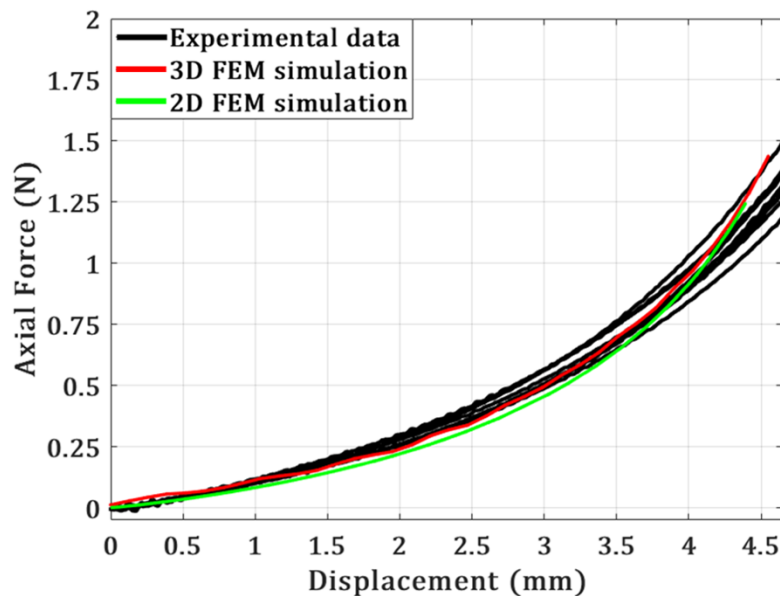


Figure 4.13. Comparison of axial forces obtained from the experimental measurements and from the 2D and 3D finite element simulation. The cannula was moving at the same axial speed adopted during the material testing (1 mm/s), without any rotation.

Despite the fact that the 2D and 3D FEM simulations do not analyze the crack initiation in soft tissue, they provide a good prediction of the cannula's axial force. However, both the models presented in Section 4.4.1, cannot be adopted in order to simulate the rotation of the cannula, while it is moving towards the tissue. In fact, in the 3D model (Section 4.4.1.1), the deformation of the tissue, in the direction of the cannula rotation, would lead to the collapse of one element

into another, while the 2D model (Section 4.4.1.2) does not provide the third spatial dimension to account for the deformation of the elements outside the plane. For these reasons, a different 3D model will be presented in Section 4.4.2.

4.4.2 Hollow Needle Insertion with Slicing Motion

An additional 3D finite element model was formulated (Fig. 4.14) to simulate the rotation of the hollow needles while penetrating the tissue (an example of the input file is given in Appendix B3). In this scenario, the previous 3D and 2D simulations are not adequate to capture this phenomenon, because of the consistent deformation of the elements in the plane perpendicular to the one in which the needle is moving. For this reason, a new computational model, similar to the one adopted by Han (Han, 2014) was built where the soft tissue was approximated as a single slice of a tissue, characterized by a radius of 10 mm, a depth of 7.5mm and an in-plane degree span equal to 5°.

The hollow needle was described as a discrete rigid body. Its geometry was set equal to the one defined in Section 4.4.1 (Fig. 4.7). Translational and rotational motions were applied to the cannula that moves parallel to the thickness of the tissue, and it is constrained with respect to the remaining motions. The mesh of the hollow needle was performed in an identical manner, as in the 3D FEM simulation presented in Section 4.4.1.1.

The geometry and motion of the cannula allow one to build an axisymmetric model, where the tissue is represented by a cylindrical sector, and periodic boundary conditions can be applied to the lateral linear surfaces of the sector to simulate the full cylinder. The radius, thickness, and azimuth angle of the cylindrical sector were equal to 10 mm, 7.5 mm, and 5 degrees, respectively (Fig. 4.14). The base of the tissue was completely constrained, while the external cylindrical

surface was assumed to be free. The mesh was built with three-dimensional eight-node hexahedral elements (C3D8) and three-dimensional six-node wedge elements (C3D6). The finite element mesh consisted of 53,001 nodes, 26,250 linear hexahedral elements of type C3D8RH, and 150 linear wedge elements of type C3D6H. The mesh consisted of 350 elements along the radius, 1 element around the circular edge, and 151 elements through the thickness of the block. In the proximity of the cutting area, which interacts with the hollow needle, the number of elements has been consistently increased. In fact, to define the stress gradient in the tissue being cut by a cannula with a radius at the tip of $15\ \mu\text{m}$, the mesh of the tissue was composed of $0.8\ \mu\text{m}$ elements in the tissue-cutting edge interaction zone (Fig. 4.14).

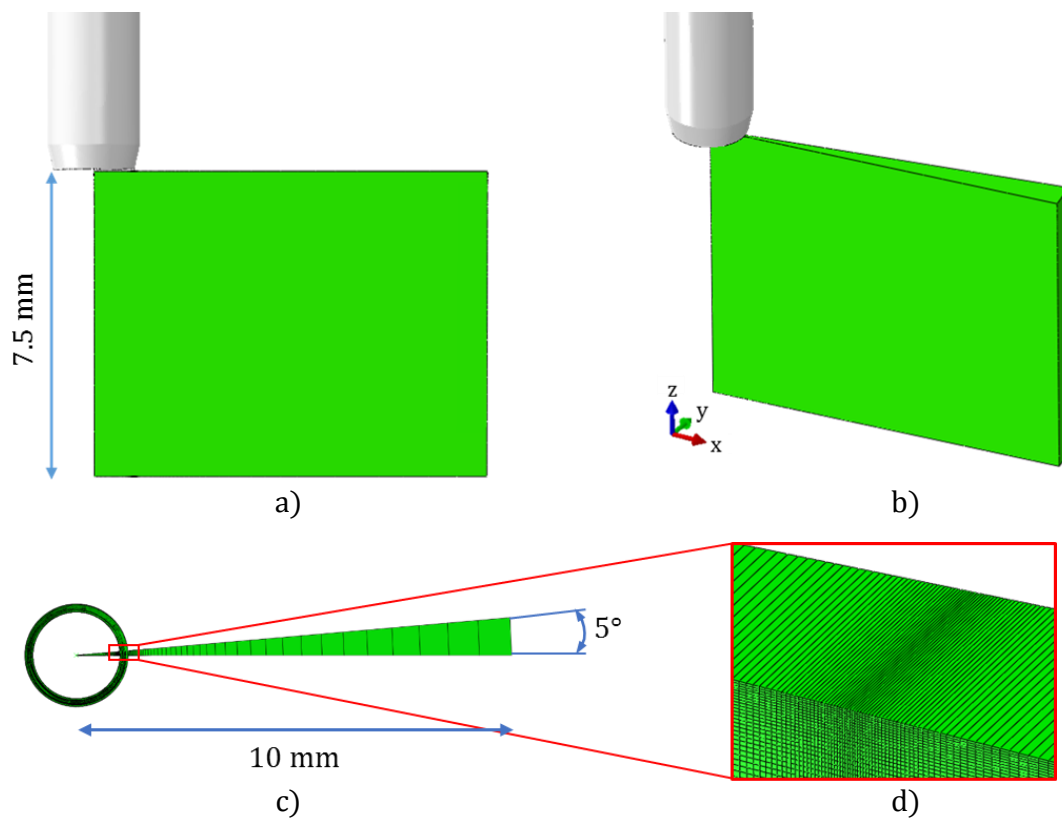


Figure 4.14. 3D Finite element model of hollow needle insertion. The mesh of the BP and of the soft tissue is shown: (a) in the side view, (b) 3D view, and (c) top view. (d) The mesh is refined in the proximity of the cutting-edge.

In the simulation, the same material parameters as those for the previous 3D simulations were used. The insertion process studied in this section can be considered a static process because of the slow speed at which the needle is moving (1 mm/s). The results from this FEM model were first compared with the ones obtained from the previous 3D model (Section 4.4.1.1) for cannula insertion without rotation. Figure 4.15 shows the configuration for deformed soft tissue in the current model and in the one presented in Section 4.4.1.1.

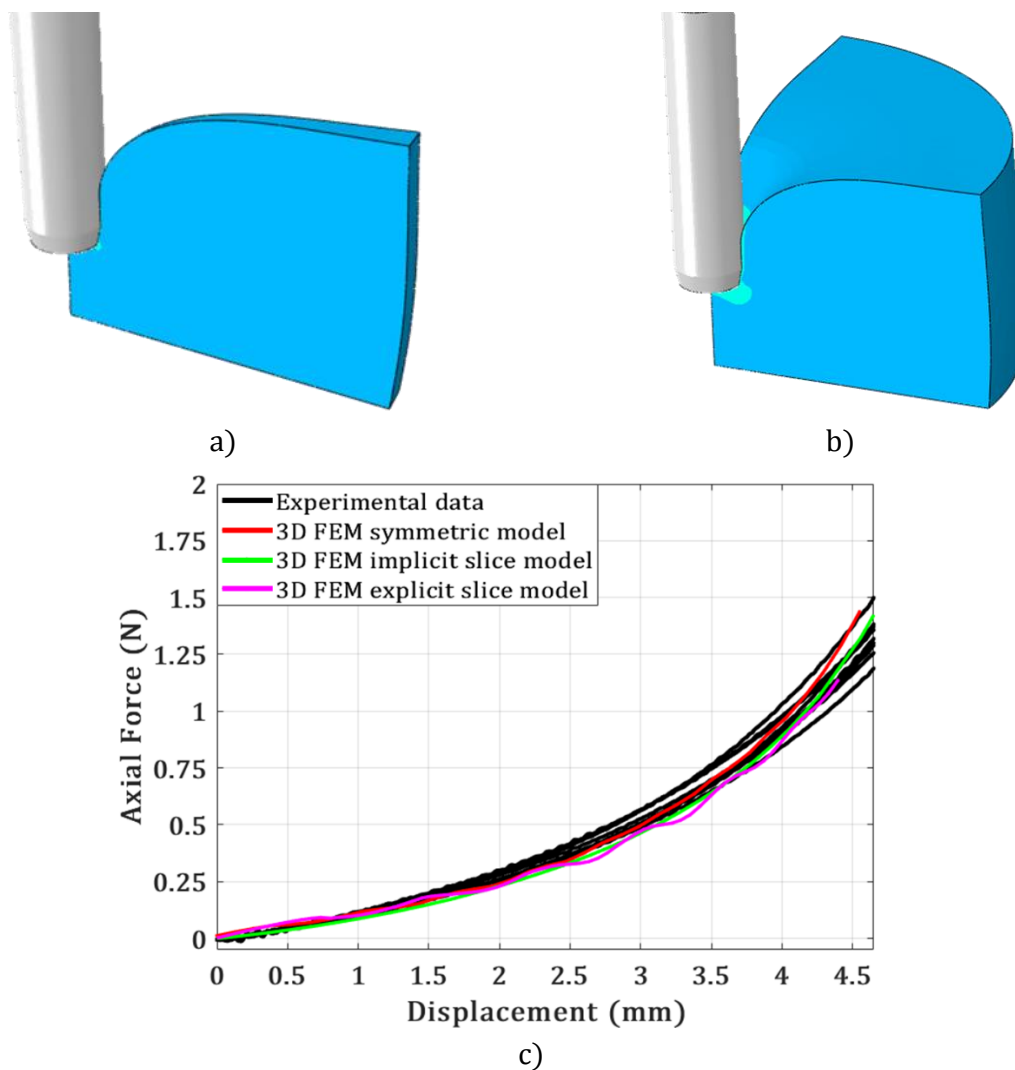


Figure 4.15. (a,b) Configuration of the soft tissue during deformation for the different 3D FEM models and (c) experimental and computational values of the axial force.

Figure 4.15c shows that the computational values of the axial force provided by the current model (“Slice Model”) are aligned with the values obtained in the 3D model presented in the previous section (“Symm. Model”). Furthermore, the current model, which considers only a slice of soft tissue, was implemented by using both an implicit and an explicit algorithm. For this 3D model, the implicit algorithm proved to be more efficient than the explicit one and allowed the simulation to complete in only 4 hours while using 48 CPUs. Since the current FEM model (“Slice Model”), lead to accurate results, the same model was adopted to simulate tissue deformation, when the cannula is entering the soft material while it is rotating (Fig. 4.16).

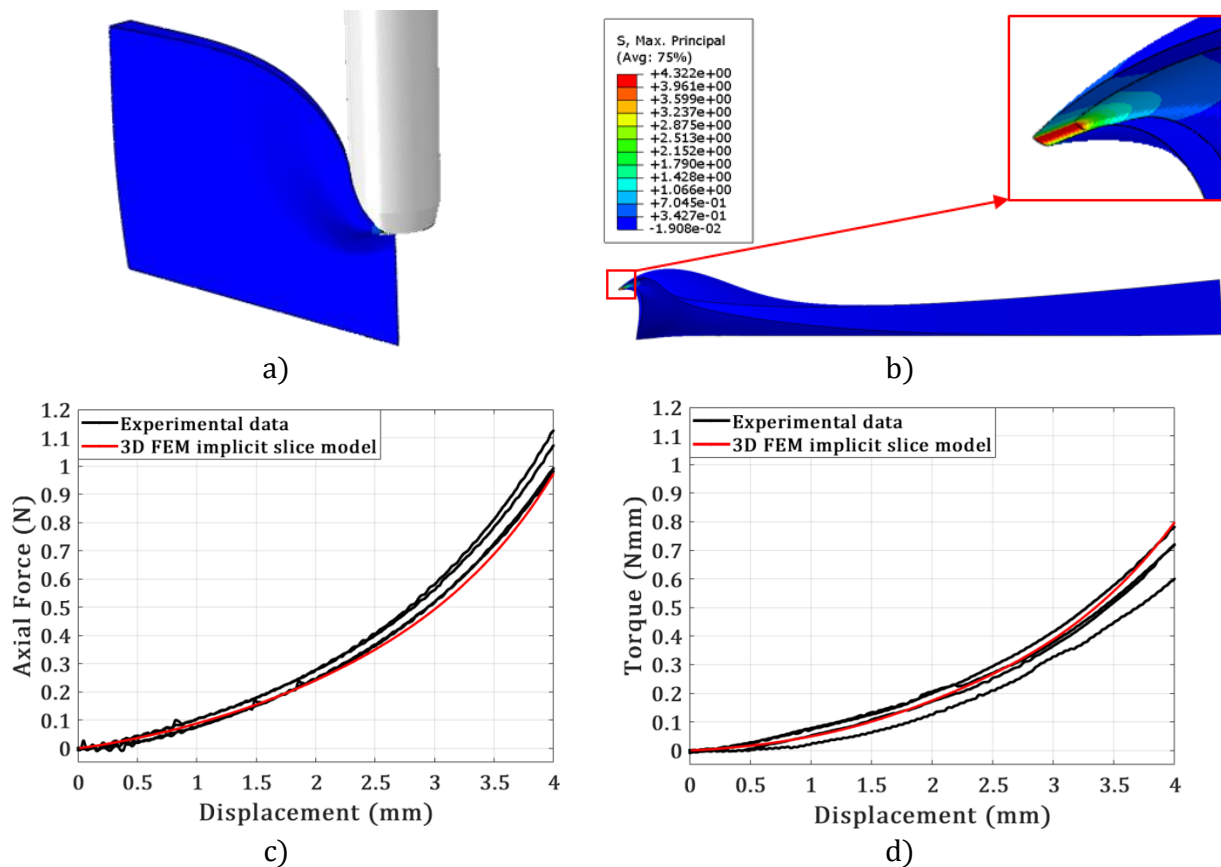


Figure 4.16. (a, b) Contour plot of maximum principal stress for the insertion of a cannula and experimental and computational values of the (c) axial force and (d) torque. The cannula axial speed was equal to 1 mm/s with a slice/push ratio, k , equal to 0.5.

Figure 4.16 shows how the maximum principal stresses are highly localized in the cutting edge-tissue contact zone, and they achieve higher values (4 MPa) with respect to the values obtained when the cannula is not rotating (Fig. 4.9). The reaction torque, due to the tangential force, F_H , applied to the cutting edge of the needle (Fig. 2.5, Chapter 2), was compared with the experimental values obtained from the torques sensor in the testbed (Section 2.3.2).

The predicted values of the axial force are approximately 18% lower than the average experimental axial force (Fig. 4.16c) while the computational values related to the torque are 10% lower than the minimum experimental torque values (Fig. 4.16d). Despite the discrepancies with the experimental data, the 3D FEM model was able to provide meaningful results and proved the correctness of the material constants adopted in the constitutive model.

4.4.3 Estimation of the Friction Coefficient in Tissue Cutting

In order to predict the axial and tangential force during tissue cutting, it is important to estimate the friction forces that arise from the contact between tissue and the cannula, especially when a slicing motion is applied. In fact, the rotation of the cannula determines the relative motion of the tissue on the cylindrical needle surface. From Chapter 2 (Section 2.2.2), the friction force in the axial (F_{Vfr}) and tangential direction (F_{Hfr}) can be determined by using the following equations:

$$F_{Vfr} = \mu_{da} \frac{\pi(r_{ni} + r_{no})E}{(1 + \eta)} x \quad (4.35)$$

$$F_{Hfr} = \mu_{dr} \frac{\pi(r_{ni} + r_{no})E}{(1 + \eta)} x \quad (4.36)$$

The values of the friction forces and of the friction coefficients (μ_{da}, μ_{dr}) were calculated from the experimental measurements, (Sections 2.5), for the same phantom tissue adopted in the finite element models (Sections 4.4.1- 4.4.2).

Table 4.2. Polynomial regression equation with related R^2 and RMSE for the dynamic friction coefficients as a function of the slice/push ratio (k).

Coefficient	Polynomial Regression Equation	R^2	RMSE
$\mu_{da}(k)$	$0.00087 k^2 - 0.0194k + 0.328$	0.823	0.018
$\mu_{dr}(k)$	$-0.03382 k^2 + 0.2726 k + 0.1243$	0.99	0.022

Figure 4.17a shows the behavior of the friction forces per unit displacement (f_{Vfr}, f_{Hfr}) and the values of the friction coefficients at different slice/push ratios (Fig. 4.17b). The axial (f_{Vfr}) and tangential friction forces (f_{Hfr}) show a similar trend with respect to the plot in Section 2.5.1, which is related to a softer phantom tissue ($S/P = 0.5$).

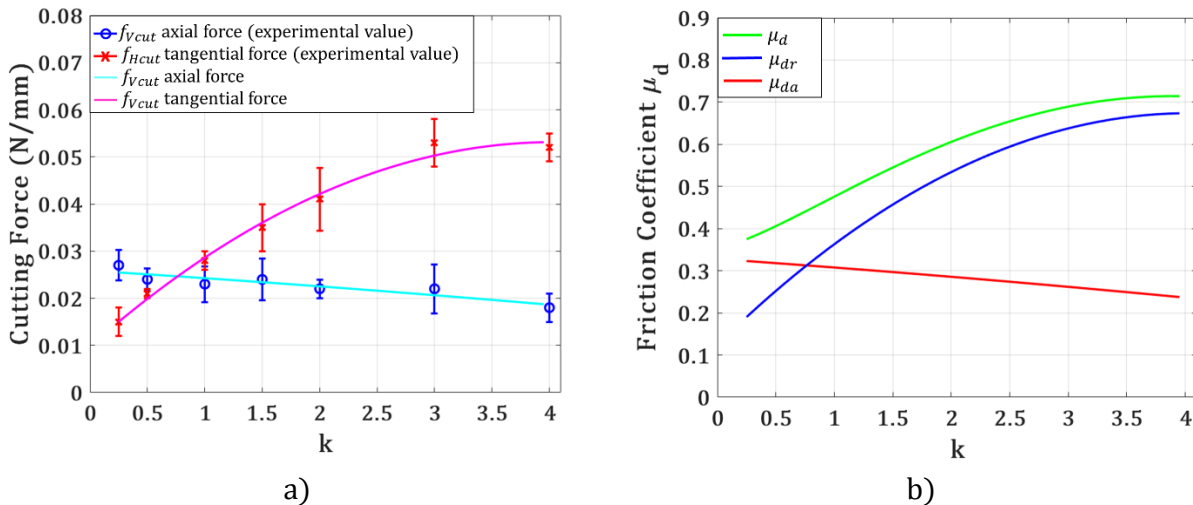


Figure 4.17. (a) Mean values and error bars of the cutting forces (f_{Vcut}, f_{Hcut}) the analytical model curves (Eqs. (4.35)-(4.36), Table 4.2), and (b) the related friction coefficients.

The value of the friction coefficient (μ_d) for a slice/push ratio equal of 0.5, is equal to 0.4 ($\mu_d = 0.4$), and it was adopted during the simulations related to hollow needle insertions with slicing motions (Section 4.4.2). Figure 4.18 shows the experimental and computational values of the axial force and torque for different values of the friction coefficient, μ_d . The friction coefficient mainly affects the tissue deformation force in the tangential direction (shown in Fig. 4.18b by plotting torque); this is because the relative motion between the cannula and the tissue causes the material to slide across the needle cutting edge. From Fig. 4.18b, it is apparent that the adoption of a friction coefficient ranging from 0.35 to 0.4, allows for a better approximation of the experimental behavior of the torque, as it was expected from the previous findings (Fig. 4.17).

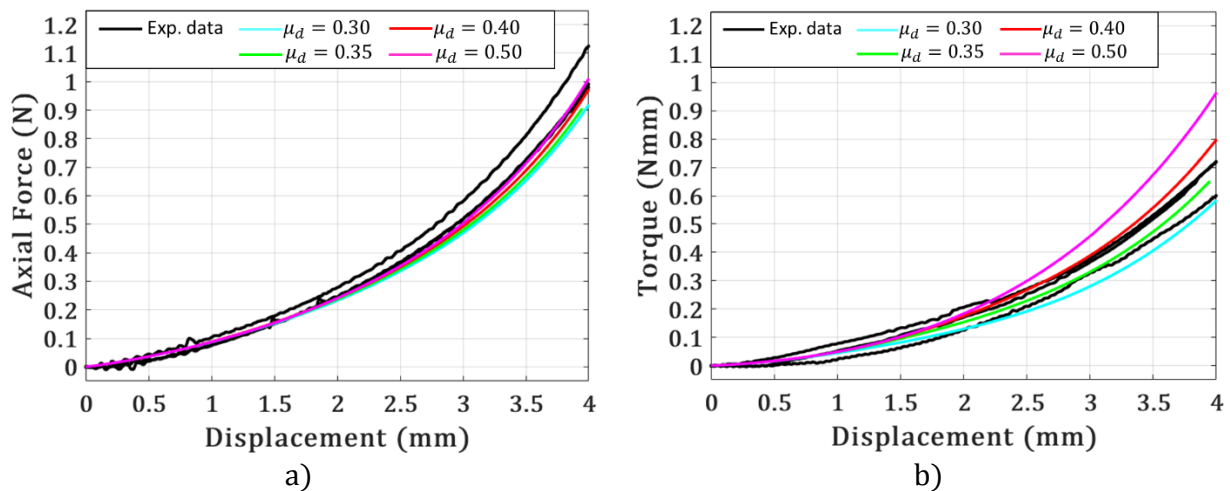


Figure 4.18. Experimental and computational values of the (a) axial force and (b) torque for different values of the friction coefficient (μ_d). The cannula axial speed is equal to 1 mm/s with a slice/push ratio, k , equal to 0.5.

4.5 Conclusions on Tissue Characterization

In this chapter, an experimental and computational study related to the characterization of phantom tissue was performed. The fundamental objective was to provide an experimental method to determine the mechanical properties of soft tissue, which can be adopted to predict its deformation using computational models.

The study was performed on polyvinyl chloride (PVC) tissue, which is commonly used to mimic human skin. Uniaxial tests were performed on a universal material testing machine, and a 3D digital image correlation (DIC) system was used to detect the strain on the tissue specimen. The material constants for several hyperelastic models were determined. The Arruda-Boyce and Ogden models allowed for a better approximation of the experimental behavior of soft tissue and, consequently, their material parameters were used in several computational models to predict the needle cutting force and torque. Two scenarios were simulated where: (i) the cannula is pushed towards the tissue without the addition of any rotation, and (ii) the cannula is rotated while pushed toward the tissue.

The results show that 2D axisymmetric finite element models provide an accurate prediction of the needle insertion force when the cannula is solely pushed towards the tissue. In fact, the computational values of the axial force obtained from the 2D FEM model are aligned both with the experimental results and with the values obtained from the 3D FEM model. These computational values for axial forces are approximately 20% lower than the values recorded from the experimental measurements

In addition, a 3D FEM model was developed to efficiently simulate the rotation of the cannula while it is moving towards the tissue. Comparisons between experimental data and FEM simulations show good correspondence, with a prediction error of the axial force below 20%,

and prove the accuracy of the characterization process. Moreover, the computational models confirmed that the maximum principal stress in the cutting area assumes higher values when the slicing motion is imposed on the cannula.

Additional investigations are needed by performing computational models which: (i) consider the strain rate sensitivity of soft material, and (ii) consider the process of crack initiation in soft tissue.

5 Micro-Texturing of Hollow Needles for Skin Biopsies

In the current chapter, the cutting-edge geometry of biopsy punches (BP), commonly adopted in skin biopsy, is analyzed in detail. As mentioned in Section 1.1, during skin biopsy, hollow needles, also referred to as biopsy punches (BP), are pressed down into the skin to extract a tissue sample to diagnose skin diseases, such as skin cancer. In this context, the cutting efficiency of these medical tools plays a crucial role in improving the extraction of optimal quality and quantity of tissue samples. In this section, we explore how soft tissue cutting may be improved by imparting micro-textures—inspired by nature, especially by mosquitos—on the tip of biopsy punches. In fact, the mosquito’s maxilla has numerous micro-teeth, which enhance its penetration into the skin and diminish nerve stimulation during puncture. Few research studies have focused on the impact of micro-serrations—similar to ones on a mosquito’s proboscis—on insertion forces, and their potential role in medical devices such as biopsy punches (Section 1.3.2). The ultimate goal is to expand the results from previous studies and explore the application of micro-serrations in biopsy punches. Commercial and micro-serrated BPs are investigated with the aim of clarifying the influence of micro-serrations on tissue cutting forces. First, the experimental setup for the manufacturing of BPs is explained. Second, the performance of commercial and serrated BPs is studied through BP penetrations into phantom tissue. Finally, 3D and 2D FEM simulations are performed to provide additional insights into stress generation in the cutting area. The experimental results will prove that significant reductions in the puncture force of BPs are achievable. This chapter is based on Giovannini et al. (Giovannini et al., 2017).

5.1 Experimental Setup for Micro-Serrated Biopsy Punches

5.1.1 Laser Ablation Process

To generate micro-features on the tip of commercial biopsy punches (BP), a picosecond laser with a wavelength of 532 nm was used. This laser (Giovannini et al., 2015) was coupled with a 5-axis motion system and a controller with a resolution of 0.01 μm . The system facilitates the rotation and translation of the needle (or workpiece) during the laser ablation process (Han, 2014). The setup is displayed in Fig. 5.1. The main components are (i) needle fixtures, and (ii) focusing and vision subsystem.

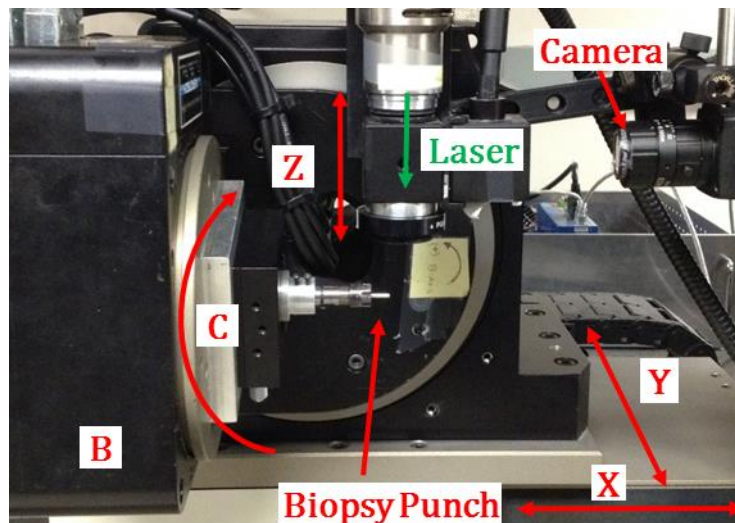


Figure 5.1. The axes of the motion system (X , Y , Z , B , C) and the main components of the laser setup are highlighted.

The needle fixture subsystem consists of a micro-adjuster, an adapter, an ER8 collet, and a shaft. The ER8 collet holds the biopsy punch during the laser machining process, and it is mounted on a shaft, which is connected to the laser's stage through a micro-adjuster. The

focusing and vision subsystem consists of a polarizing beam splitter, a polarization-insensitive beam splitter, a laser focusing lens, a fiber optical illuminator, a CCD camera, a camera lens, and a notch filter. The CCD camera captures magnified images of the workpiece, and its focal position is aligned with the laser focus (Han et al., 2013b).

5.1.2 Micro Serration Design

Micro-serrations were generated on a commercial BP with a circular cutting edge. This BP is characterized by the same cannula geometry presented in Section 4.4 (Fig. 4.7), and the micro-features were generated on its cutting edge by adopting laser ablation. The laser power was set to 0.75 W and the frequency of laser pulses to 100 kHz. The serrated profile is defined by its radius at the tip (r_s), the arc radius (r_c) and the angle between two consecutive serrations (ρ). Figure 5.2 shows the laser path used to generate the micro-features on the BP cannula.

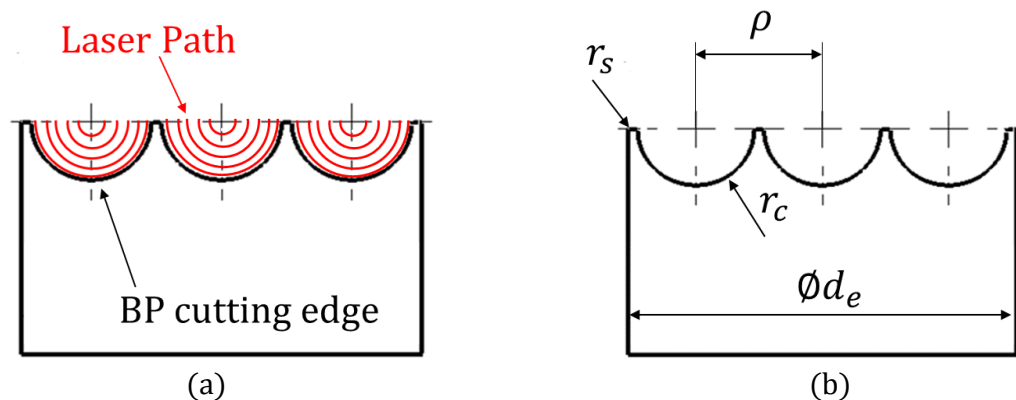


Figure 5.2. (a) Laser path for generating serrations on BP's cutting edge and (b) the geometry of the micro-serrations.

In this work, the laser followed an offset path, shown in red in Fig. 5.2a, with respect to the ultimate shape. The laser trajectory used an overlap of 90%. It progressively ablated the

material, eventually leading to the generation of the desired features along the cutting edge of the biopsy punch (an example of the code for laser ablation is given in Appendix C).

Several micro-serration patterns were designed, manufactured, and tested on different BP cutting edges. Each pattern had a circular profile (Fig. 5.2) with different arc radii (r_c) that ranged from 50 μm to 600 μm (Table 5.1). The radius at the serration edges (r_s), after laser processing, was approximately equal to 15 μm for all micro-serrated BPs, while the radius at the cutting edge (r_{tip}) was not affected by the ablation process (Fig. 5.2).

The minimal arc radius for the BP serrations (r_c) was set to 50 μm . Micro-serrations with a serration radius (r_c) smaller than 50 μm , does not significantly impact the original geometry of the BP's cutting edge. In fact, the tip radius (r_{tip}) of the BP cutting edge is equal to 15 μm (Fig. 4.7) and any serrations with a serration radius (r_c) of the same order as the tip radius (r_{tip}), would not lead to any effective change in the cutting edge geometry. The serration configurations are presented in Table 5.1.

Table 5.1. Serration configurations. Each configuration is identified by a different micro-serration radius (r_c) (Fig. 5.2).

ID	r_c (μm)
C_1	50
C_2	150
C_3	250
C_4	400
C_5	600

Following the laser ablation process, the geometry of each BP's cutting edge was verified by using a 3D profilometer (Fig. 5.3).

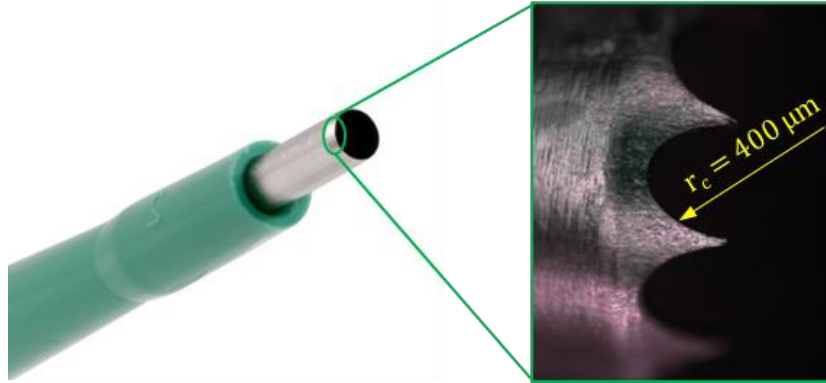


Figure 5.3. Optical image of micro-serrations generated on BP's cutting tip. The external diameter is equal to 2.4 mm, internal diameter to 2 mm, while the arc radius of the BP's micro-serrations is equal to 400 μm .

5.2 Fracture Mechanics Approach

During the insertion of the biopsy punch, the puncture force can be analyzed by studying the fracture mechanics related to the BP insertion. According to the J integral method (Ryu et al., 2011), a crack will propagate inside the tissue when the energy generated by the insertion is equal or greater than the energy needed to extend the crack (R), i.e.:

$$J_e \geq R \quad (5.1)$$

where R is defined as the strain energy release rate that represents the energy required to propagate the crack. The nonlinear energy release rate (J_e) is equal to the derivative with respect to the contact area (A_{co}) of the difference between the strain energy of the tissue (U) and the external work applied by the punch (W_N) (Anderson, 2005; Atkins et al., 2004):

$$J_e = \frac{d(U - W_N)}{dA_{co}} \quad (5.2)$$

When tissue fracture occurs at the end of Phase I (Fig. 5.5b), the punch is stationary and its work (W_N) during crack propagation is equal to zero, so J_e accounts only for the strain energy:

$$J_e = \frac{dU}{dA_{co}} \quad (5.3)$$

In this scenario, it is extremely challenging to calculate U , because of the complexity of the crack geometry. Further, the strain energy can be derived from the stress by adopting the constitutive equations of the tissue. According to Mahvash et al. (Mahvash & Dupont, 2009), it can be assumed that the pressure (p_n) over the contact area (A_{co}) between the punch and the tissue is constant and that the resulting stresses in the soft tissue are proportional to the contact pressure. In light of these considerations, it is possible to establish a proportional relationship between J_e and the contact pressure (p_n) which also includes a crack intensification factor, K_i , (Atkins & Mai, 1985) and a coefficient, m , which accounts for the nonlinearity of the material as:

$$J_e \propto K_i p_n^m \quad (5.4)$$

Since the contact pressure (p_n) is equal to the ratio between the axial force (F_V) that pushes the BP and the contact area (A), Eq. (5.4) can be rearranged as (Mahvash et al., 2009):

$$F_V \propto \sqrt[m]{\frac{R}{K_i}} A_{co} \quad (5.5)$$

According to Eq. (5.5), the axial force at puncture is proportional to the contact area between the BP and soft tissue (Mahvash et al., 2009). During insertions performed with micro-serrated BPs the contact area (A_{SEERR}) is lower than the contact area (A_{STAND}) during insertions performed with standard BPs. In fact, micro-serrated edges exert the cutting force over reduced contact areas, i.e.:

$$A_{SEERR} < A_{STAND} \quad (5.6)$$

$$\sqrt[m]{\frac{R}{K_i}} A_{SEERR} < \sqrt[m]{\frac{R}{K_i}} A_{STAND} \quad (5.7)$$

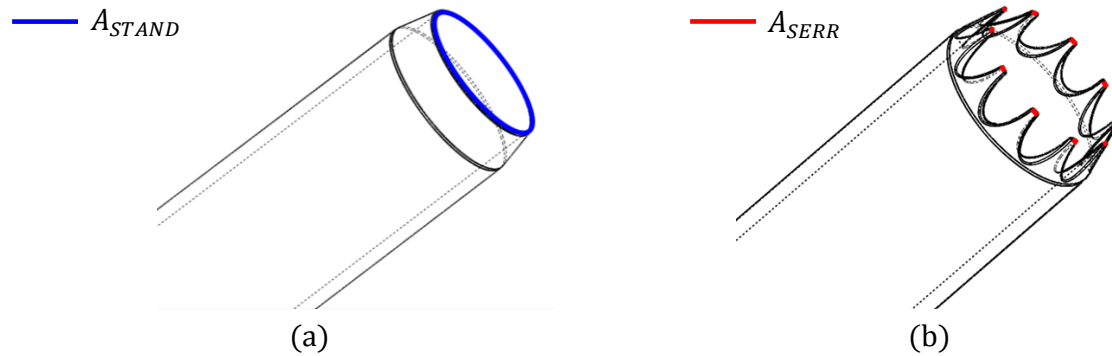


Figure 5.4. 3D geometric model of (a) standard and (b) micro-serrated BP. The contact area at the BP tip is highlighted.

The effects of the reduced contact area lead to the decrease of the puncture force during insertions with micro-serrated BPs, and to an increase in the localized stresses in the soft tissue to be further discussed in Section 5.3. Since this phenomenon is due to the presence of the 3D texture (Fig. 5.4) at the micro-scale level, it is difficult to analyze it from an analytical perspective, and it will be further investigated in Section 5.4 by adopting 3D FEM simulations.

5.3 Experimental Cutting Forces of Micro-Serrated Biopsy Punches

In this section, the outcomes of experimental insertions will be studied with the purpose of investigating the influence of micro-features (Section 5.3.1) on the cutting performance of biopsy punches. In addition, the impact of micro-serrations of different sizes on the resulting cutting force will be ascertained (Section 5.3.2).

5.3.1 Insertion of Micro-Serrated BPs

The mosquito's maxilla represents an optimal model for efficient penetration with a low insertion force and efficient penetration (Izumi et al., 2008). Imitating its jagged outer shape can potentially lead to significant benefits. Commercial and micro-serrated biopsy punches were inserted at an axial speed of 0.25 mm/s, by adopting the same testbed that was introduced in Section 2.3.2, (Fig. 5.5a).

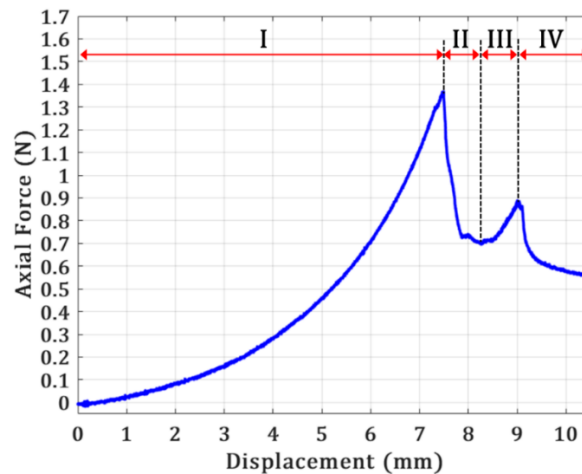
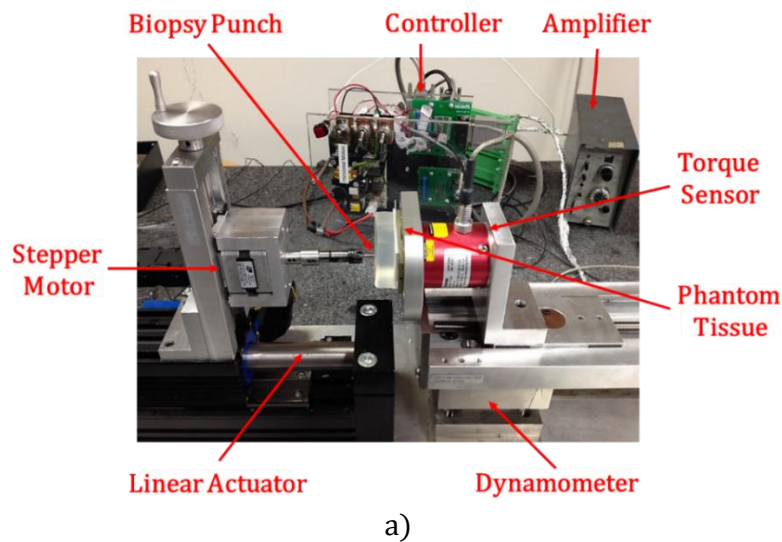


Figure 5.5. (a) Testbed for the measurement of cutting forces of biopsy punches and (b) axial force behavior for a commercial BP highlighting the different penetration phases.

The penetration depth was set to 9 mm, and five cuts were executed for each biopsy punch. In this scenario, the biopsy punch cutting force was measured by a 3D piezoelectric dynamometer. During the penetration of the punch, different phases can be observed reflecting a behavior similar to what has already been established for solid needle insertions (Fig. 5.5b).

In the first phase, Phase (I), deformation, begins when the needle touches the phantom tissue and ends when the first crack initiates. In this phase, the biopsy punch deforms the soft tissue without cutting, and the axial force increases until a peak force is reached. This force is defined as the puncture force and determines the initial fracture of the soft tissue and the beginning of penetration. This study is mainly focused on investigating the effect of micro-serrations on the puncture force. In Phase II, the soft tissue is subjected to a temporary relaxation that follows the fracture event. This phase, referred to as the relaxation phase, is characterized by a reduction of the axial force. During Phase III, the cutting phase, the biopsy punch is advancing into the soft tissue while it is steadily cutting it. In this phase, the increase of the force is mostly due to the proportional increase of the friction force between the BP surface and the soft tissue. The last phase, Phase IV, sees a decrease in the measured force due to the extraction of the punch.

In this study, insertions with commercial and micro-serrated biopsy punches were performed to observe the effectiveness of the technique and highlight the advantages of micro-serrations (Fig. 5.6). By comparing the force profiles for biopsy punches with and without micro-serrations, it is evident that the forces at puncture are substantially different.

Figure 5.6 shows the axial force for a commercial and a micro-serrated BP with a “C₄” texture (Table 5.1). The presence of micro-serrations on BP’s cutting tip leads to a reduction of the puncture force from 1.19 N to 0.75 N.

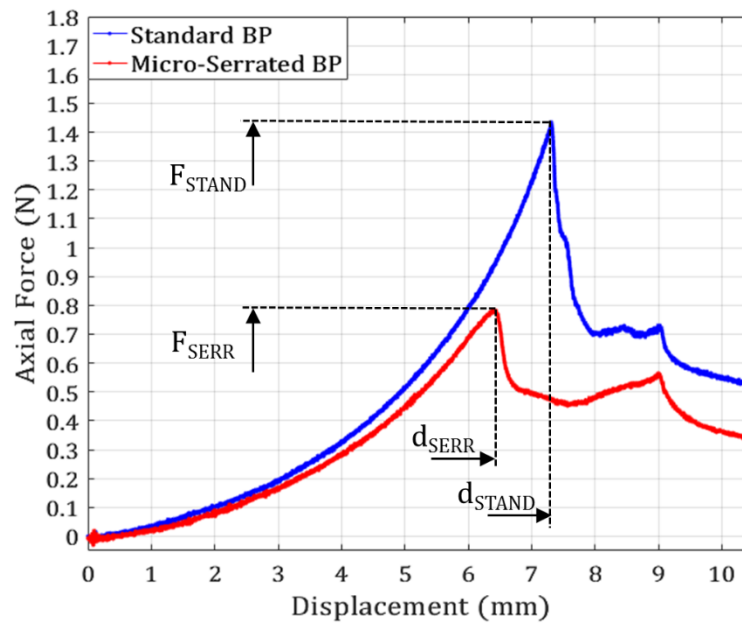


Figure 5.6. Axial force at puncture for a standard biopsy punch BP with and without “C₄” micro-serrations (Table 5.1) at an insertion speed of 0.25 mm/s.

An unpaired t-test, which assumes unequal variances between samples, was performed by using the force data measured during commercial and micro-serrated BP insertions. For micro-serrated BP with a “C₄” texture (Fig. 5.7), the axial force ($\mu = 0.87$, $\sigma = 0.1$) proved to be 22.5% lower (p-value = 0.016) than the axial force measured during insertions with commercial BPs ($\mu = 1.12$, $\sigma = 0.04$). This phenomenon can be explained by the concentration of higher localized stresses (Section 5.2) in the contact area between the micro-serrations and soft tissue that provokes its earlier fracture. In fact, the application of micro-serrations also leads to a reduction of the tissue’s initial displacement (Fig. 5.6) at fracture from 6.6 mm (d_{STAND}) to 6.05 mm (d_{SERR}).

5.3.2 Texture Depth Effect in Micro-Serrated BP Insertion

To better understand the influence of micro-serrations, similar experiments were conducted using BPs with different texture sizes (Table 5.1). The measured cutting forces were approximately between 0.8 N and 1.15 N for all tested punches. Micro-serrations with larger texture depths (Fig. 5.7), lead to lower cutting forces and consequently to higher variations in the axial force ($\Delta F = \frac{F_{SERR} - F_{STAND}}{F_{SERR}} 100\%$). Unpaired two tailed-tests (significance level, α , equal to 0.05) were run by comparing the forces measured during insertions of commercial and micro-serrated BPs (Table 5.2). The results show that micro-serrated biopsy punches lead to a reduction of the BP axial force between 7 % and 30%.

The fact that deeper textures lead to lower cutting forces is mainly due to the manner in which micro-serrations engage with soft tissue during BP penetration. For instance, insertions performed with BPs with a texture radius of 400 μm present a smaller contact area between the BP and tissue than insertions performed with BPs with a texture radius of 150 μm (Fig. 5.7).

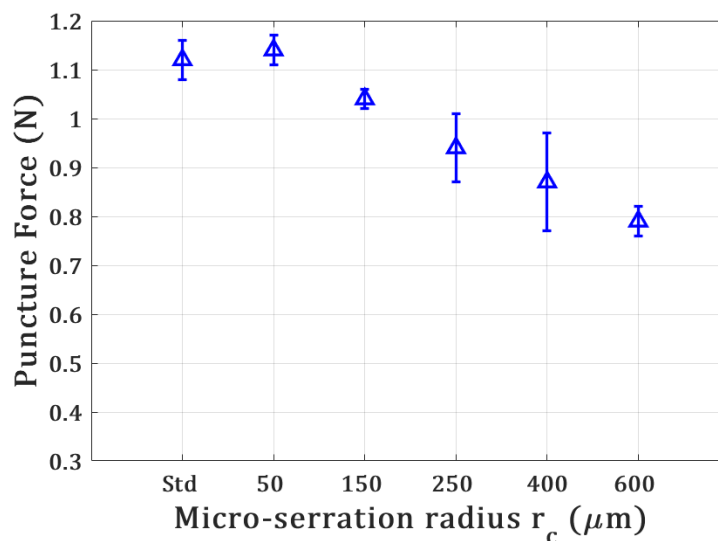


Figure 5.7. Mean value and error bar of puncture force for standard and textured BPs with different micro-serration radius, r_c (Fig. 5.2).

The presence of larger micro-serrations on the BP likely determines higher localized stresses in soft tissue, since the contact area is smaller. This will also be observed in the following computational study (Section 5.4).

Table 5.2. The mean value (μ), standard deviation (σ), p-value and force variation value presented for each serration configuration.

ID	μ	σ	p – value	ΔF (%)
C ₁	1.14	0.030	0.004	2.03
C ₂	1.04	0.017	0.016	–7.24
C ₃	0.92	0.064	0.001	–17.59
C ₄	0.84	0.009	0.001	–22.55
C ₅	0.79	0.027	3.14E – 06	–29.90

The reduction in the cutting force is not consistent ($\Delta F = 2\%$, Fig. 5.7) for micro-serrated punches with a texture radius of 50 μm . This is due to the fact that this texture radius is comparable to the tip radius at BP’s cutting edge ($r_{tip} = 15 \mu\text{m}$) and it does not dramatically alter the geometry of the cutting edge.

5.4 Computational Study of BP Insertion

In this section, computational studies related to the insertion of micro-serrated biopsy punches will be performed. In Section 5.4.1, a comparison between a standard and a micro-serrated BP will be presented by adopting 3D FEM simulations aimed at studying the stresses induced in the contact area by the micro-serrated profiles. In Section 5.4.2, the impact of the micro-serration radius on the cutting performance of BPs will be evaluated through 2D FEM simulations. This choice is dictated by the high computational cost of 3D FEM simulations for

modeling serrated cutting edges and the possibility of adopting a plane stress condition for this case.

5.4.1 Computational Study of Micro-Serrated BPs

To provide additional insights into the efficacy of micro-serrations, a FEM model was formulated (Fig. 5.8) in ABAQUS, while the mesh for the biopsy punch and the soft tissue was realized with HyperMesh (an example of the input file is given in Appendix B4). In this computational study, two different cases were analyzed where the same tissue block was indented by a commercial BP in the first scenario and by a micro-serrated BP (ii), with a texture depth of 600 μm in the second scenario.

The BP was described as a discrete rigid body. Its geometry was set to be equal to the geometry of the BPs adopted during the experiments (Fig. 4.7). A translational motion parallel to the thickness of the tissue was applied to the BP, and it was constrained with respect to the remaining translational and rotational motions. The mesh of the BPs consisted of three dimensional triangular (R3D3) and quadrilateral (R3D4) elements. Specifically, the finite element mesh of the commercial BP mesh was built with 37,255 nodes, 37,105 R3D4 elements, and 24 R3D3 elements. More elements were used to mesh the micro-serrated BP to have a better definition of the serrated edges. The mesh of the micro-serrated BP was built with 148,637 nodes, 146,689 R3D4 elements, and 3,896 R3D3 elements.

The soft tissue block was considered to be a deformable body, and it was represented by a cylinder with an external radius of 1.5 mm and an internal radius of 0.5 mm and a thickness of 2.5 mm. Since the model is symmetric with respect to the xz - and yz -planes, a quarter of the cylinder with symmetric boundary conditions was used in the simulations (Fig. 5.8) as the soft

tissue. The base of the tissue was completely constrained, while the external cylindrical surface was assumed to be free. The mesh was built by adopting three-dimensional eight-node hexahedral elements (C3D8) and three-dimensional six-node wedge elements (C3D6).

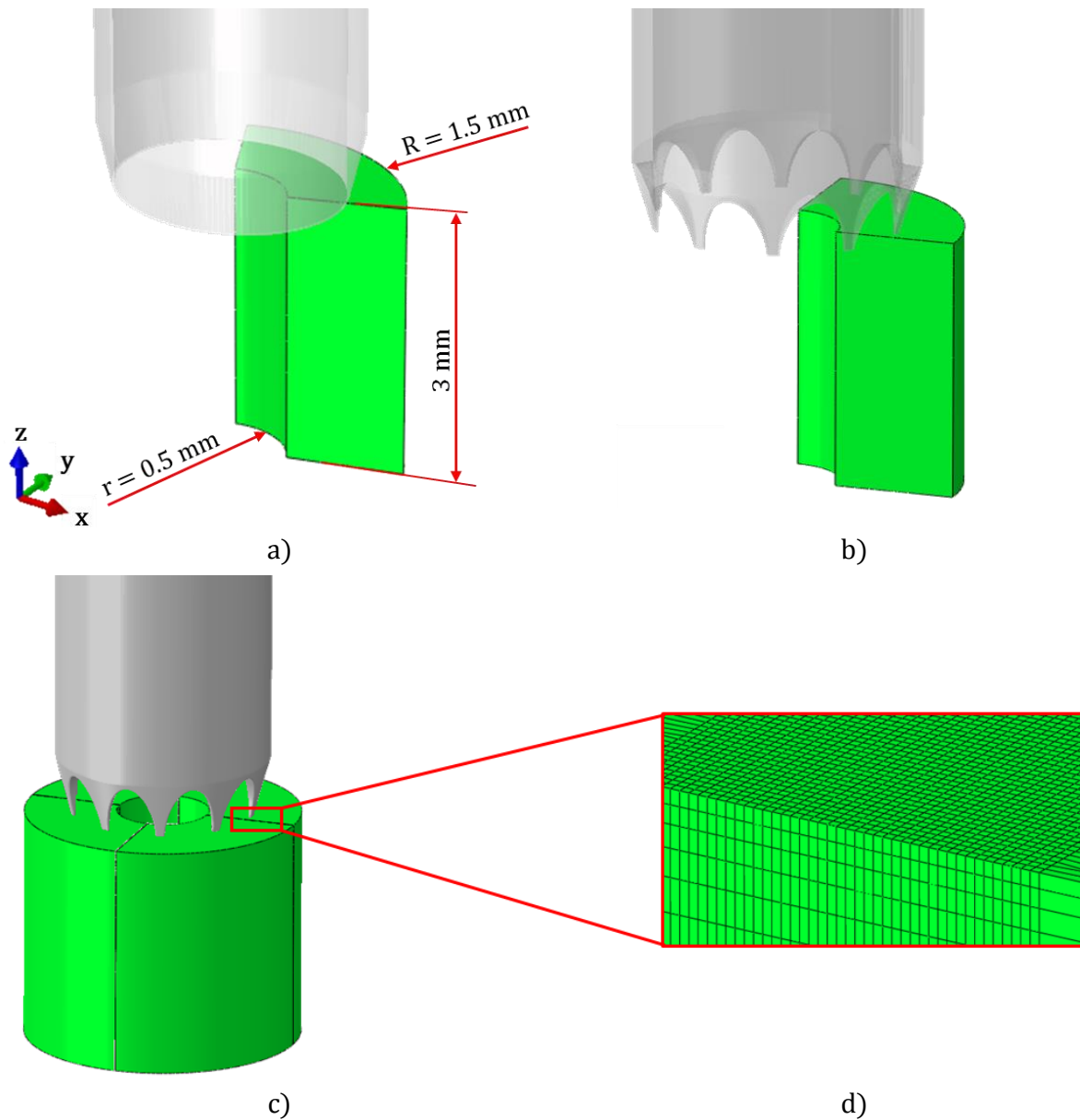
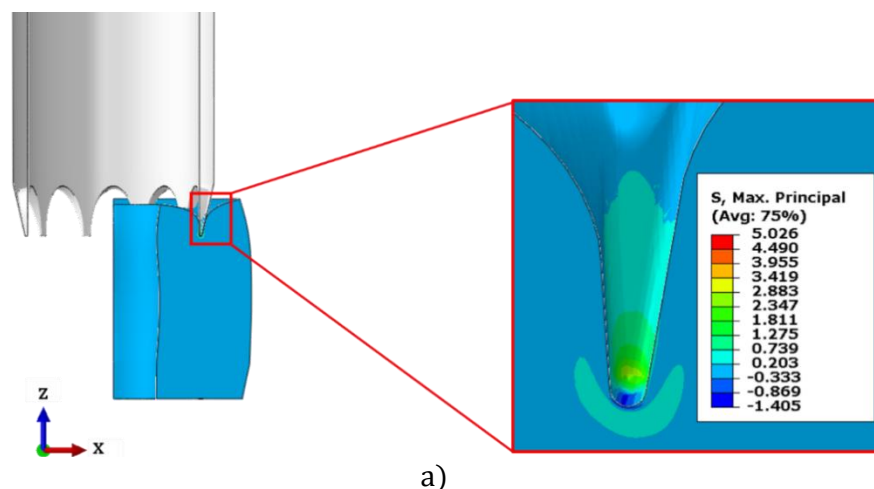


Figure 5.8. 3D Finite element model for insertion with (a) standard and (b) and micro-serrated. The mesh is refined in the proximity of the micro-serrations (c, d).

The finite element mesh consisted of 2,499,690 nodes, 2,371,968 C3D8 elements and 78,300 C3D6 elements. The soft tissue mesh consisted of 90 elements along the radius, 29 elements through the thickness of the block, and 5 to 80 elements around the circular edge. This distribution of the elements was necessary to define the stress gradient in the tissue since the cannula radius at the tip is equal to 15 μm . The resulting mesh was characterized by 1 μm elements in the tissue-cutting edge interaction zone (Fig. 5.8d). The tissue was modeled by adopting hyperelastic constitutive models (Arruda-Boyce model), where the material constants c_1 , λ_m , and D_1 are respectively equal to 0.0238, 2.024, and 0.705 (S/P ratio equal to 0.25, Appendix A).

During the simulation, the cutting edge of the BP was pushed towards the tissue. The stresses generated in the contact zone during cutting with the commercial BP and with the micro-serrated BP were compared. All the model parameters were kept identical in the two simulations, including the mesh, boundary conditions, and constitutive model of the soft tissue. Since soft solids can fail under critical tensile stresses (Reyssat et al., 2012), the 1st principal stresses in the tissue contact zone were investigated.



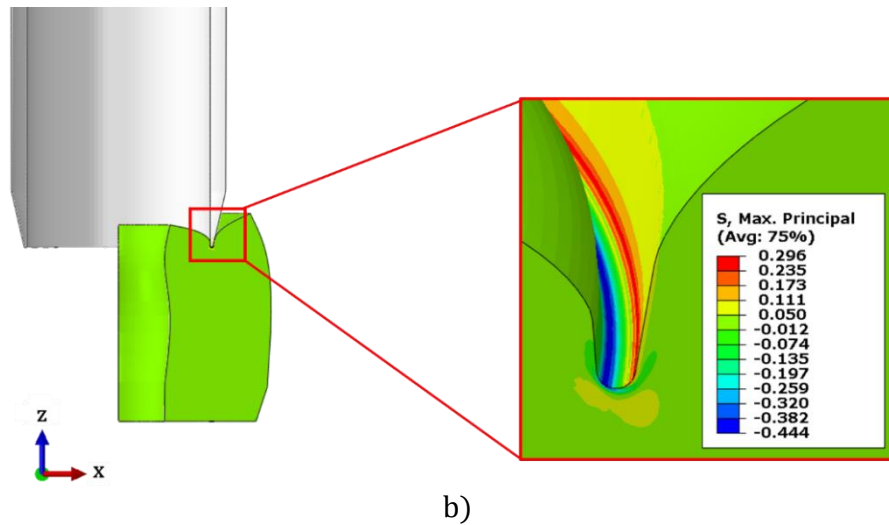


Figure 5.9. Contour plot of maximum principal stress for the insertion of (a) micro-serrated and (b) standard BP. In the zoomed area, the BP cutting edge is hidden in order to show the stress distribution in the contact area.

Figure 5.9 shows the contour plot of the maximum principal stress when commercial BP reaches a penetration depth of 500 μm . The stresses are highly localized in the cutting edge-tissue contact zone. The maximum tensile stress is found to be distributed at the external side of the cutting edge-tissue contact zone, and it is approximately equal to 5 MPa (Fig. 5.9a). The tensile stress results from the stretching of the tissue surface, while the internal side of the cutting edge-tissue contact zone is characterized by negative values of the principal stress. For insertions performed with micro-serrated BPs (Fig. 5.9a), the simulations show that for the same BP penetration depth (500 μm), the stresses are exclusively localized at the corner of the micro-serrations, and they are approximately one order of magnitude higher than the maximum principal stresses recorded for indentations with commercial BPs.

The presence of micro-features along the tip of the BP cannula leads to a rapid rise of the stresses in localized areas, which favors the initiation of fracture and the consequent cutting of

the soft tissue. Figure 5.10 shows the comparison between the experimental insertion force profiles and the ones computed by finite element simulations for commercial and serrated BPs.

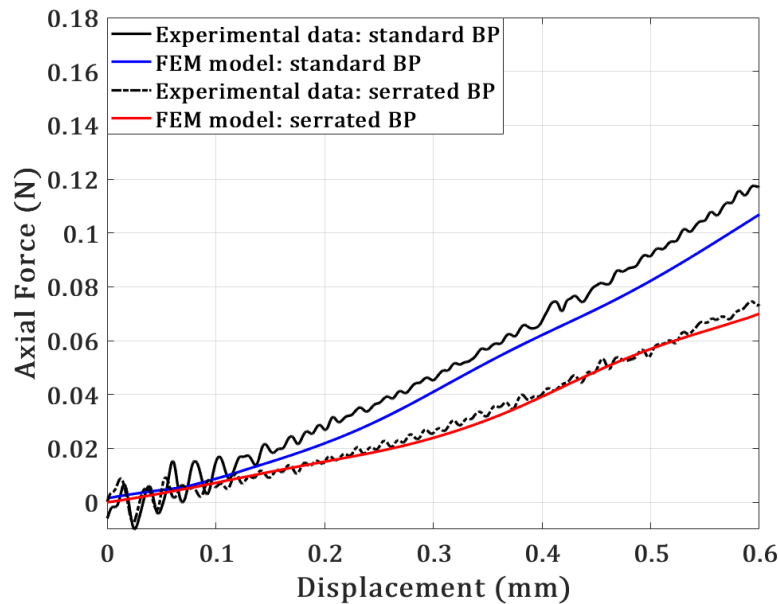


Figure 5.10. Comparison of axial forces obtained from the experimental measurements and from the finite element simulation for standard and serrated BPs.

The behavior of the axial force is similar to the one observed in the experiments, although the force values are slightly lower due to several approximations in the finite element model. For instance, the needle insertion speed was increased by 4 times, and the tissue density was increased by 200 times, in order to increase the time step of the simulation. Also, the BP penetration was set to be equal to 600 μm in the effort to limit the computational cost of the simulation.

Despite the fact that these simulations do not analyze the crack initiation in soft tissue, they provide a framework to understand the reasons why micro-serrations on devices are more effective in soft tissue cutting. The serrated profile causes an earlier rise in the contact forces,

which then leads to an earlier fracture of the tissue, and lower cutting forces in comparison to plain edge profiles.

5.4.2 Computational Study of Different Micro-Serrations

To further investigate the impact of the micro-serration size on cutting efficiency, a finite element analysis was performed (Fig. 5.11) with ABAQUS standard (an example of the input file is given in Appendix B5). Two scenarios were considered where the same tissue block was indented by micro-serrated BPs with a texture radius of 50 μm in the first scenario, and by a texture radius of 400 μm in the second scenario. A 2D finite element model, rather than a 3D one, was built for each scenario. In fact, in the first model, the BP is characterized by a fine micro-texture radius (50 μm), that would require a high computational cost if implemented in a FEM 3D model.

The micro-serrated biopsy punch was defined as a rigid body. The BP geometry was approximated by a rectangular blade 2.75 mm wide and 2 mm thick. In the simulations, the BP indented the tissue for 0.5 mm, and it was constrained in the other directions.

The size of the tissue slab cross-section is equal to 10 mm in width and 4 mm in thickness. A plane stress assumption was made in the model to describe micron-scale deformations without excessively impacting the computational costs of the simulation. The base of the tissue was completely constrained, while the other sides were set free of loads. The mesh of the tissue consisted of 94,996 linear quadrilateral elements of type CPS4R. The minimum size of the elements is equal to 10 μm in the cutting zone. As in the previous FEM simulations, the tissue was modeled by the Arruda-Boyce model.

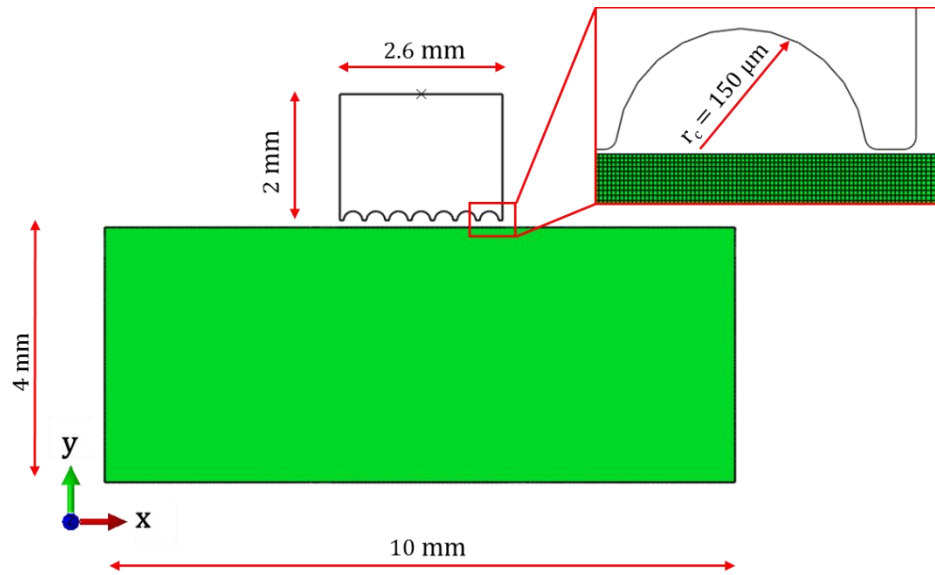
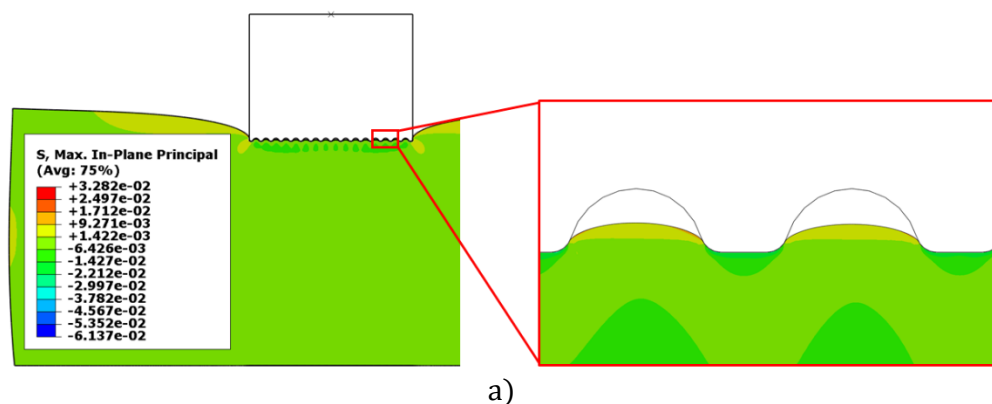


Figure 5.11. 2D Finite element model of biopsy punch insertion. The mesh and geometrical dimensions of the model are highlighted.

One simulation for each micro-serrated BP insertion was performed. By comparing the contour plots related to the maximum penetration depth reached by the BP (Fig. 5.12), it can be noticed that the contact area is smaller for micro-serrated BPs with a larger textured depth ($r_c = 400 \mu\text{m}$), as it was described in Section 5.2. This leads to higher localized stresses in soft tissue. For a cutting depth of 0.5mm, a BP with $400 \mu\text{m}$ serrations induced maximum principal stress (in soft tissue) that was two times higher than the one induced by a BP with $50 \mu\text{m}$ serrations.



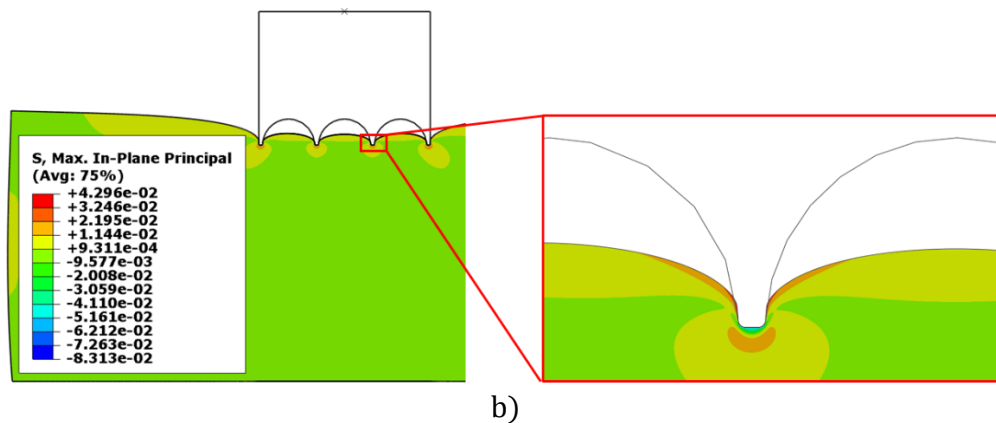


Figure 5.12. Contour plot of the maximum principal stress related to the insertion of a biopsy punch with a micro-serration radius of (a) 50 μm and (b) 600 μm .

Even though the values of the maximum principal stress (Fig. 5.12) are much lower than the values found during 3D simulations (Section 5.4.1), they explain how serrations with different sizes have a different impact on soft tissue cutting. Micro-serrations with a larger texture depth lead to an earlier rise of tensile stresses, causing its earlier fracture and a decrease in the cutting force, as was indicated in the experimental results (Fig. 5.6).

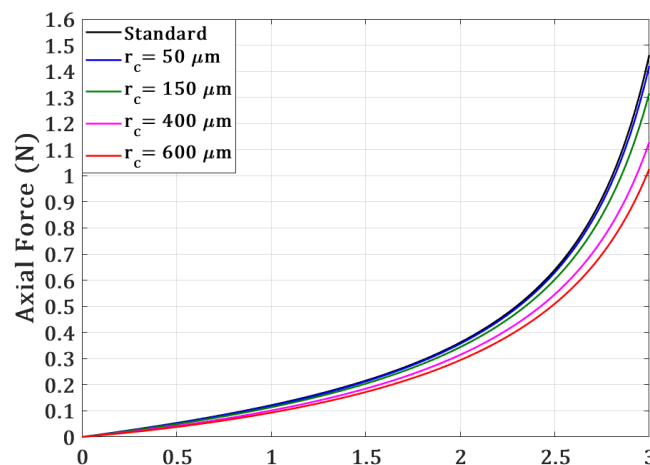


Figure 5.13. Comparison of axial forces obtained from the 2D FEM simulations related to insertions performed with a standard biopsy punch and with biopsy punches, characterized by micro-serration radii ranging from 50 μm to 600 μm .

5.5 Conclusions on Micro-Serrated Biopsy Punch Insertion

In this chapter, the effects of serrated biopsy punches on soft tissue cutting were investigated. A setup for laser ablation of BP cutting edges was implemented, and micro-features were manufactured on their cutting edges. Insertion tests were performed with the aim to investigate the influence of BP micro-serrations on the cutting force. 3D finite element simulations were performed regarding the deformation of hyperelastic soft tissue undergoing large deformations. This computational study was able to capture the micro- and macro-scale aspects of the cutting phenomena before the fracture of the hyperelastic soft tissue.

The results show that micro-serrations on the cutting tip of the BP cannula, lead to significant reductions of the cutting forces and potentially to less pain during soft tissue cutting. The 2D finite element simulations provide insights related to the comparison between the performances of BPs, characterized by micro-serrations of different sizes.

In the future, additional computational studies related to micro-scale modeling and soft tissue cutting should be performed. To this end, it is crucial to develop FEM models to predict the cracking of the tissue and the evolution of the insertion forces over a wider range of displacements. The rise of stresses in localized tissue areas, due to the presence of BP micro-serrations, should be further investigated to analyze possible implications in terms of tissue damage and consequences on surface integrity.

The manufacturing of micro-serrations on BPs with different geometries and dimensions should be considered. According to this study, the presence of micro-serrations increases the BP cutting efficiency but may also make BP's cutting edge more fragile and prone to breakage. Therefore in the future, an optimum balance should be identified to obtain efficient and resilient micro-serration geometries.

6 Conclusions and Future Work

6.1 Conclusions

Hollow medical needles are frequently used in minimally invasive procedures, mainly aimed at the extraction of tissue, the delivery of medical fluids for common operations like regional anesthesia, and special treatments such as skin biopsy, breast biopsy, and bone marrow biopsy. Although the above medical procedures have been widely practiced, the problems related to the optimal cutting of soft tissue have not been completely addressed. In this research, the focus was placed on various metrics related to the cutting performance of hollow needles. The work presented in this thesis aimed to enhance the fundamental understanding of tissue cutting by investigating: (i) the geometry, and (ii) the cutting motions of medical needles. The main outcomes of this dissertation can be summarized as:

- An analytical and experimental study related to the impact of rotational motions during core biopsy procedures was performed. Needles with low included angles and high inclination angles lead to lower cutting forces, as suggested by the analytical models. Two- and three-plane bevel needles with an included angle of 15° , or lower, represent the optimal tip geometries for soft tissue cutting. The analysis of the cutting motions at different slice/push ratios shows that the application of rotational motion leads to (i) consistent decrease of the axial fracture forces, up to 80%, especially for a slice/push ratio that is less than 2, and (ii) a consistent increase of the tangential cutting forces after fracture is initiated. For this reason, it is recommended to adopt a slice/push ratio of at least 1 before rupture of the soft tissue occurs and of no more than 1.5, once the needle is penetrating. Moreover, the application of

rotational motions is more critical for: (i) axial speeds ranging from 0.5 to 2 mm/s, which are the most common in a clinical environment, and for (ii) soft materials characterized by Young's modulus equal or higher than 13 kPa.

- Core biopsy needles characterized by a three-dimensional cutting edge were conceived and demonstrated by developing a helical geometry. The helical geometry was applied to a 14-gauge cannula, which is usually adopted to perform breast biopsies. The mathematical models were resolved to compute the main cutting angles and the fracture forces related to helical needles. The proposed methodologies can be applied to virtually any needle geometry. Furthermore, a helical geometry was manufactured and tested on phantom tissue for translational and rotational insertions. The measurement of the cutting forces demonstrates that the application of the helical geometry leads to a 20% decrease of the axial and translational forces. Moreover, cutting tests performed at different rotational/translational ratios have shown a reduction of the perpendicular and tangential fracture forces for ratio larger than 1.5. The experimental results were mostly aligned with the analytical estimates of the fracture forces obtained from the formulated model for the helical geometry. Finally, a physics-informed Gaussian process metamodel was adopted to statistically investigate the sensitivity of the needle's cutting length and of its main cutting angles to the helix angle and to the rotation angle of the cannula. The results show that it is possible to predict the main helical needle cutting angles for any combination of the input angles, and therefore optimize the helical geometry by formulating a proper objective function.
- An experimental and computational study related to the characterization of phantom tissue was performed. The fundamental objective was to provide an experimental method to

determine the mechanical properties of PVC soft tissue, which can be adopted to predict its deformation. Uniaxial tests were performed on a universal material testing machine, and a 3D digital image correlation (DIC) system was used to detect the strain on the tissue specimen. The material constants for several hyperelastic models were determined. Two scenarios were studied in which: (i) the cannula is pushed towards the tissue without the addition of any rotation, and (ii) the cannula is rotated while pushed toward the tissue. The results show that analytical models can predict the overall behavior of cutting forces, while FEM studies can provide more accurate results. To this end: (i) 2D axisymmetric finite element models were developed to predict the needle insertion force when the cannula is solely pushed towards the tissue, and (ii) 3D FEM models were developed to efficiently simulate the rotation of the cannula while it is moving towards the tissue. Comparisons between experimental data and FEM simulations show good correspondence and prove the accuracy of the characterization process. Moreover, the computational models confirmed that the maximum principal stress in the cutting area assumes higher values when a slicing motion is imposed on the cannula.

- A setup for laser ablation of BP cutting edges was implemented, and micro-features were manufactured on their cutting edges. Insertion tests were performed with the aim to investigate the influence of BP micro-serrations on the cutting force. 3D finite element simulations have been performed regarding the deformation of hyperelastic soft tissue undergoing large deformations. The results show that micro-serrations on the cutting tip of the BP cannula, lead to significant reductions of the cutting forces and potentially to less pain during soft tissue cutting. The 2D finite element simulations provide insights related to the

comparison between the performances of BPs, characterized by micro-serrations of different sizes.

6.2 Future Work

The work presented in this thesis has shown evidence that the application of rotational cutting motions and novel 3D cutting edge geometries have the potential to affect the performances of core-biopsy needles positively. Additional investigations can be performed by:

- Executing cutting tests on heterogeneous anisotropic phantom tissues, which are aimed to model a specific part of the human body, such as the skin or bone marrow, depending on the biopsy procedure under investigation. In fact, biological tissue is characterized by a fibrous structure, which varies from organ to organ, and can be artificially reproduced to obtain a better assessment of the needle geometry under study;
- Executing cutting tests on biological tissues: first on animal tissue and, during later stages, on patients, by fostering the collaboration with medical schools. In fact, some biopsy procedures, such as breast biopsy, can be performed with semi-automated devices, (e.g., Mammotome), which can be equipped with force sensors to test different needle geometries in real clinical settings;
- Developing alternative 3D shapes for the needle's cutting edge and further optimizing the helical geometry in order to lower the cutting forces. Further, the development of each 3D geometry can be tailored to the tissue that will be targeted by the procedure (breast tissue, skin tissue) and to the specific characteristics of the patients, such as age or clinical conditions;

- Developing additional methods for the manufacturing of 3D needle geometries. Additional manufacturing methods can be considered to manufacture novel 3D geometries including Laser-Induced Plasma Machining (LIPMM) and freeform grinding methods, which can generate the desired geometry more efficiently;
- Formulating computational models which: (i) consider the strain rate sensitivity of soft materials, (ii) considering the process of crack initiation in soft tissue, especially when slicing motions are applied. The 3D simulation of the fracture process in soft materials is largely unexplored and can bring new insights that could lead to the optimization of the cutting process;
- Optimization of micro-serration geometry. Alternative micro-serration designs, characterized by different geometries and dimensions, can be considered in future studies. Further, the presence of micro-serrations increases the biopsy punch cutting efficiency but may also make the biopsy punch's cutting edge more fragile and prone to breakage. Therefore in the future, an optimum balance should be identified to obtain efficient and resilient micro-serration geometries.

References

- Abaqus 6.13 Online Documentation. (2013). Dassault Systèmes.
- Abolhassani, N., & Patel, R. (2006a). Deflection of a flexible needle during insertion into soft tissue. In *2006 International Conference of the IEEE Engineering in Medicine and Biology Society* (pp. 3858–3861). New York, NY, USA: IEEE.
- Abolhassani, N., Patel, R., & Ayazi, F. (2007a). Effects of different insertion methods on reducing needle deflection. In *29th Annual International Conference of the IEEE Engineering in Medicine and Biology Society* (pp. 491–494). Lyon, France: IEEE.
- Abolhassani, N., Patel, R., & Moallem, M. (2004). Trajectory generation for robotic needle insertion in soft tissue. In *The 26th Annual International Conference of the IEEE Engineering in Medicine and Biology Society* (Vol. 3, pp. 2730–2733). San Francisco, CA, USA: IEEE.
- Abolhassani, N., Patel, R., & Moallem, M. (2006b). Control of soft tissue deformation during robotic needle insertion. *Minimally Invasive Therapy & Allied Technologies*, 15(3), 165–176.
- Abolhassani, N., Rajni Patel, & Farzam Ayazi. (2007b). Needle control along desired tracks in robotic prostate brachytherapy. In *IEEE International Conference on Systems, Man and Cybernetics* (pp. 3361–3366). Montreal, Canada: IEEE.
- American Cancer Society. (2017). *Cancer Facts & Figures 2017*.
- Anderson, T. L. (2005). *Fracture mechanics : fundamentals and applications* (3rd ed.). Boca Raton, FL, USA: CRC Press.
- Aoyagi, S., Izumi, H., & Fukuda, M. (2008). Biodegradable polymer needle with various tip angles and consideration on insertion mechanism of mosquito's proboscis. *Sensors and Actuators A*, 143(1), 20–28.
- Aoyagi, S., Takaoki, Y., Takayanagi, H., Huang, C., Tanaka, T., Suzuki, M., ... Matsumoto, T. (2012). Equivalent negative stiffness mechanism using three bundled needles inspired by mosquito for achieving easy insertion. In *2012 IEEE/RSJ International Conference on Intelligent Robots and Systems* (pp. 2295–2300). Vilamoura, Portugal: IEEE.
- Atkins, A. G. (2009). *The Science and Engineering of Cutting: The Mechanics and Processes of Separating, Scratching and Puncturing Biomaterials, Metals and Non-Metals* (1st ed.). Oxford, UK: Butterworth-Heinemann.
- Atkins, A. G., & Mai, Y. W. (1985). *Elastic and plastic fracture : metals, polymers, ceramics*,

composites, biological materials. Chichester, UK: Ellis Horwood.

- Atkins, A. G., Xu, X., & Jeronimidis, G. (2004). Cutting, by “pressing and slicing,” of thin floppy slices of materials illustrated by experiments on cheddar cheese and salami. *Journal of Materials Science*, *39*(8), 2761–2766.
- Audet, C., & Dennis, J. E. (2002). Analysis of generalized pattern searches. *SIAM Journal on Optimization*, *13*(3), 889–903.
- Ayvali, E., Liang, C.-P., Ho, M., Chen, Y., & Desai, J. P. (2012). Towards a discretely actuated steerable cannula for diagnostic and therapeutic procedures. *The International Journal of Robotics Research*, *31*(5), 588–603.
- Badaan, S., Petrisor, D., Kim, C., Mozer, P., Mazilu, D., Gruionu, L., ... Stoianovici, D. (2011). Does needle rotation improve lesion targeting? *International Journal of Medical Robotics and Computer Assisted Surgery*, *7*(2), 138–147.
- Bagwell, R. B., Clement, R. S., Meehan, A. J., Scruggs, C. A., Sheehan, R. M., & Mulvihill, M. L. (2014). *U.S. Patent No. 10219832*. U.S. Patent and Trademark Office.
- Barnhill, R. E., & Kersey, S. N. (1990). A marching method for parametric surface/surface intersection. *Computer Aided Geometric Design*, *7*(1–4), 257–280.
- Bayarri, M. J., Berger, J. O., Cafeo, J., Garcia-Donato, G., Liu, F., Palomo, J., ... Walsh, D. (2007). Computer model validation with functional output, *35*(5), 1874–1906.
- Begg, N. D. M., & Slocum, A. H. (2014). Audible frequency vibration of puncture-access medical devices. *Medical Engineering and Physics*, *36*(3), 371–377.
- Bessa, M. A., Bostanabad, R., Liu, Z., Hu, A., Apley, D. W., Brinson, C., ... Liu, W. K. (2017). A framework for data-driven analysis of materials under uncertainty: Countering the curse of dimensionality. *Computer Methods in Applied Mechanics and Engineering*, *320*, 633–667.
- Boothroyd, G., & Knight, W. A. (2005). *Fundamentals of machining and machine tools*. Boca Raton, FL, USA: CRC Press.
- Bostanabad, R., Bui, A. T., Xie, W., Apley, D. W., & Chen, W. (2016a). Stochastic microstructure characterization and reconstruction via supervised learning. *Acta Materialia*, *103*, 89–102.
- Bostanabad, R., Chen, W., & Apley, D. W. (2016b). Characterization and reconstruction of 3D stochastic microstructures via supervised learning. *Journal of Microscopy*, *264*(3), 282–297.
- Bostanabad, R., Kearney, T., Tao, S., Apley, D. W., & Chen, W. (2018a). Leveraging the nugget

- parameter for efficient Gaussian process modeling. *International Journal for Numerical Methods in Engineering*, 114(5), 501–516.
- Bostanabad, R., Zhang, Y., Li, X., Kearney, T., Brinson, L. C., Apley, D. W., ... Chen, W. (2018b). Computational microstructure characterization and reconstruction: Review of the state-of-the-art techniques. *Progress in Materials Science*, 95, 1–41.
- Bower, A. F. B. (2010). *Applied Mechanics of Solids*. Boca Raton, FL, USA: CRC Press.
- Che, D., Guo, P., & Ehmann, K. F. (2012). Design and analysis of helical needle tip grinding process. In *ASME 2012 International Manufacturing Science and Engineering Conference Collocated with the 40th North American Manufacturing Research Conference and in Participation with the Int. Conf., MSEC 2012* (pp. 33–42). Notre Dame, IN, USA.
- Chen, P.-Y., Mckittrick, J., & Meyers, M. A. (2012). Biological materials: functional adaptations and bioinspired designs. *Progress in Materials Science*, 57(8), 1492–1704.
- Chen, Z., Lin, Y., Lee, W., Ren, L., Liu, B., Liang, L., ... Jiang, L. (2018). Additive Manufacturing of Honeybee-Inspired Microneedle for Easy Skin Insertion and Difficult Removal. *ACS Appl. Mater. Interfaces*, 10(35), 29338–29346.
- Cho, W. K., Ankrum, J. A., Guo, D., Chester, S. A., Yun Yang, S., Kashyap, A., ... Karp, J. M. (2012). Microstructured barbs on the North American porcupine quill enable easy tissue penetration and difficult removal. *Proc Natl Acad Sci U S A*, 109(52), 21289–21294.
- Conti, S., Gosling, J. P., Oakley, J. E., & O'hagan, A. (2009). Gaussian process emulation of dynamic computer codes. *Biometrika*, 96(3), 663–676.
- Conti, S., & O'hagan, A. (2010). Bayesian emulation of complex multi-output and dynamic computer models. *Journal of Statistical Planning and Inference*, 140(3), 640–651.
- David A. Stephenson, J. S. A. (2016). *Metal Cutting Theory and Practice* (3rd ed.). Boca Raton, FL, USA: CRC Press.
- Dimaio, S. P., & Salcudean, S. E. (2003). Needle insertion modelling and simulation. In *Proceedings 2002 IEEE International Conference on Robotics and Automation (Cat. No.02CH37292)* (pp. 2098–2105 vol.2). Washington, DC, USA.
- Ehmann, K., & Malukhin, K. (2012). A Generalized analytical model of the cutting angles of a biopsy needle tip. *Journal of Manufacturing Science and Engineering*, 134(6), 061001.
- Gefen, A., & Dilmoney, B. (2007). Mechanics of the normal woman's breast. *Technology and Health Care: Official Journal of the European Society for Engineering and Medicine*, 15(4), 259–271.

- Giovannini, M., Cao, J., & Ehmann, K. (2019). Design and models of helical needle geometries for core biopsies. *Journal of the Mechanical Behavior of Biomedical Materials*, 90, 113–124.
- Giovannini, M., Moser, N., & Ehmann, K. (2015). Experimental and analytical study of micro-serrations on surgical blades. In *ASME 2015 International Technical Conference and Exhibition on Packaging and Integration of Electronic and Photonic Microsystems, InterPACK 2015, collocated with the ASME 2015 13th International Conference on Nanochannels, Microchannels, and Minichannels* (Vol. 3). San Francisco, CA, USA.
- Giovannini, M., Ren, H., Cao, J., & Ehmann, K. (2018a). Study on design and cutting parameters of rotating needles for core biopsy. *Journal of the Mechanical Behavior of Biomedical Materials*, 86, 43–54.
- Giovannini, M., Ren, H., Wang, X., & Ehmann, K. (2017). Tissue Cutting with Microserrated Biopsy Punches. *Journal of Micro and Nano-Manufacturing*, 5(4), 041004.
- Giovannini, M., Wang, X., Cao, J., & Ehmann, K. (2018b). Vibration-assisted slicing of soft tissue for biopsy procedures. *Journal of Medical Devices, Transactions of the ASME*, 12(3), 031006.
- Gramacy, R. B., & Apley, D. W. (2015). Local gaussian process approximation for large computer experiments. *Journal of Computational and Graphical Statistics*, 24(2), 561–578.
- Han, P. (2014). *Mechanics of Soft Tissue Cutting in Needle Insertion*. Northwestern University.
- Han, P., Che, D., Pallav, K., & Ehmann, K. (2012). Models of the cutting edge geometry of medical needles with applications to needle design. *International Journal of Mechanical Sciences*, 65(1), 157–167.
- Han, P., & Ehmann, K. (2013a). Study of the effect of cannula rotation on tissue cutting for needle biopsy. *Medical Engineering and Physics*, 35(11), 1584–1590.
- Han, P., Kim, J., Ehmann, K. F., & Cao, J. (2013b). Laser surface texturing of medical needles for friction control. *International Journal of Mechatronics and Manufacturing Systems*, 6(3), 215–228.
- Hartmann, E. (2003). *Geometry and Algorithms for COMPUTER AIDED DESIGN. Lectures notes, Department of Mathematics, Darmstadt University of Technology*.
- Hassaninia, I., Bostanabad, R., Chen, W., & Mohseni, H. (2017). Characterization of the Optical Properties of Turbid Media by Supervised Learning of Scattering Patterns. *Scientific Reports*, 7(1), 15259.

- Heverly, M., Dupont, P., & Triedman, J. (2005). Trajectory Optimization for Dynamic Needle Insertion. In *Proceedings of the 2005 IEEE International Conference on Robotics and Automation* (pp. 1646–1651). Barcelona, Spain: IEEE.
- Hing, J. T., Brooks, A. D., & Desai, J. P. (2006). Reality-based needle insertion simulation for haptic feedback in prostate brachytherapy. In *Proceedings of the 2006 IEEE International Conference on Robotics and Automation* (pp. 619–624). Orlando, FL, USA.
- Izumi, H., Suzuki, M., Aoyagi, S., & Kanzaki, T. (2011). Realistic imitation of mosquito's proboscis: Electrochemically etched sharp and jagged needles and their cooperative inserting motion. *Sensors and Actuators A*, *165*(1), 115–123.
- Izumi, H., Yajima, T., Aoyagi, S., Tagawa, N., Arai, Y., Hirata, M., & Yorifuji, S. (2008). Combined Harpoonlike Jagged Microneedles Imitating Mosquito's Proboscis and Its Insertion Experiment with Vibration. *IEEJ Transactions on Electrical and Electronic Engineering*, *3*(4), 425–431.
- Jaiswal, S., & Muthuswamy, S. (2015). Instability Analysis of Mosquito Fascicle under Compressive Load with Vibrations and Microneedle Design. *Journal of Bionic Engineering*, *12*(3), 443–452.
- Jansen, L. E., Birch, N. P., Schiffman, J. D., Crosby, A. J., & Peyton, S. R. (2015). Mechanics of intact bone marrow. *Journal of the Mechanical Behavior of Biomedical Materials*, *50*, 299–307.
- Kong, X. Q., & Wu, C. W. (2009). Measurement and Prediction of Insertion Force for the Mosquito Fascicle Penetrating into Human Skin. *Journal of Bionic Engineering*, *6*(2), 143–152.
- Kong, X. Q., & Wu, C. W. (2010). Mosquito proboscis: An elegant biomicroelectromechanical system. *Physical Review E - Statistical, Nonlinear, and Soft Matter Physics*, *82*(1), 011910.
- Krause, J. (1981). *Bone marrow biopsy*. New York, NY, USA: Churchill Livingstone.
- Lai, W. M., Rubin, D., & Krempl, E. (2010). *Introduction to continuum mechanics* (4th ed.). Burlington, MA, USA: Butterworth-Heinemann.
- Lenau, T. A., Hesselberg, T. ;, Drakidis, A. D., Silva, P. ;, & Gomes, S. (2017). Mosquito inspired medical needles. In *SPIE Conference on Bioinspiration, Biomimetics, and Bioreplication 2017* (Vol. 10162, pp. 1–13). Portland, OR, USA: APA.
- Li, W., Belmont, B., & Shih, A. (2015). Design and Manufacture of Polyvinyl Chloride (PVC) Tissue Mimicking Material for Needle Insertion. *Procedia Manufacturing*, *1*, 866–878.
- Lin, C., Kang, S. K., & Ehmann, K. F. (1995). Helical micro-drill point design and grinding.

Journal of Engineering for Industry, 117(3), 277–287.

- Ling, J., Jiang, L., Chen, K., Pan, C., Li, Y., Yuan, W., & Liang, L. (2016). Insertion and Pull Behavior of Worker Honeybee Stinger. *Journal of Bionic Engineering*, 13(2), 303–311.
- Ling, J., Song, Z., Wang, J., Chen, K., Li, J., Xu, S., ... Jiang, L. (2017). Effect of honeybee stinger and its microstructured barbs on insertion and pull force. *Journal of the Mechanical Behavior of Biomedical Materials*, 68, 173–179.
- Linos, E., Katz, K. A., & Colditz, G. A. (2016). Skin Cancer-The Importance of Prevention. *JAMA Internal Medicine*, 176(10), 1435–1436.
- Ma, G. J., Shi, L. T., & Wu, C. W. (2011). Biomechanical Property of a Natural Microneedle: The Caterpillar Spine. *Journal of Medical Devices*, 5(3), 034502.
- MacDonald, B., Ranjan, P., & Chipman, H. (2013). GPfit: An R package for Gaussian Process Model Fitting using a New Optimization Algorithm. *Journal of Statistical Software*, 64(12), 1–23.
- Mahvash, M., & Dupont, P. E. (2009). Mechanics of dynamic needle insertion into a biological material, 4(57), 934–943.
- Marsot, J., Claudon, L., & Jacqmin, M. (2007). Assessment of knife sharpness by means of a cutting force measuring system. *Applied Ergonomics*, 38(1), 83–89.
- Mccarthy, C. T., Annaidh, A. N., & Gilchrist, M. D. (2010). On the sharpness of straight edge blades in cutting soft solids: Part II – Analysis of blade geometry. *Engineering Fracture Mechanics*, 77(3), 437–451.
- Mcgorry, R. W., Dowd, P. C., & Dempsey, P. G. (2005). The effect of blade finish and blade edge angle on forces used in meat cutting operations. *Applied Ergonomics*, 36(1), 71–77.
- Meltsner, M. A., Ferrier, N. J., & Thomadsen, B. R. (2007). Observations on rotating needle insertions using a brachytherapy robot Related content Methods for prostate stabilization during transperineal LDR brachytherapy. *Physics in Medicine & Biology*, 52, 6027–6037.
- Meyers, M. A., Lin, A. Y. M., Lin, Y. S., Olevsky, E. A., & Georgalis, S. (2008). The cutting Edge: Sharp Biological Materials. *JOM*, 60, 19–24.
- Mguil-Touchal, S., Morestin, F., & Brunei, M. (1997). Various Experimental Applications of Digital Image Correlation Method. *Transactions on Modeling and Simulation*, 17, 14.
- Moore, J. Z., Malukhin, K., Shih, A. J., & Ehmann, K. F. (2011). Hollow needle tissue insertion force model. *CIRP Annals - Manufacturing Technology*, 60, 157–160.
- Moore, J. Z., McLaughlin, P. W., & Shih, A. J. (2012a). Novel needle cutting edge geometry for

- end-cut biopsy. *Medical Physics*, 39(1), 99–108.
- Moore, J. Z., Zhang, Q., McGill, C. S., Zheng, H., McLaughlin, P. W., & Shih, A. J. (2010). Modeling of the Plane Needle Cutting Edge Rake and Inclination Angles for Biopsy. *Journal of Manufacturing Science and Engineering*, 132(5), 0510051-1–8.
- Moore, J. Z., Zhang, Q., McGill, C. S., Zheng, H., McLaughlin, P. W., & Shih, A. J. (2012b). Modeling cutting edge geometry for plane and curved needle tips. *Proceedings of the Institution of Mechanical Engineers, Part B: Journal of Engineering Manufacture*, 226(5), 861–869.
- Ogden, R. W. (1972). Large deformation isotropic elasticity – on the correlation of theory and experiment for incompressible rubberlike solids. *Proceedings of the Royal Society of London*, 326, 565–584.
- Oka, K., Aoyagi, S., Arai, Y., Isono, Y., Hashiguchi, G., & Fujita, H. (2002). Fabrication of a micro needle for a trace blood test. *Sensors and Actuators A*, 97–98, 478–485.
- Oldfield, M. J., Leibinger, A., Seah, T. E. T., & Rodriguez Y Baena, F. (2015). Method to Reduce Target Motion Through Needle-Tissue Interactions. *Annals of Biomedical Engineering*, 43(11), 2794–2803.
- Podder, T. K., Clark, D. P., Sherman, J., Fuller, D., Messing, E. M., Rubens, D. J., ... Oncology, R. (2005a). Effects of tip geometry of surgical needles: an assesment of force and deflection. In *European Medical and Biological Engineering Conference* (Vol. 11, pp. 1–4). Prague, Czech Republic.
- Podder, T. K., Clark, D. P., Sherman, J., Fuller, D., Messing, E. M., Rubens, D. J., ... Yu, Y. (2005b). EFFECTS OF TIP GEOMETRY OF SURGICAL NEEDLES: AN ASSESSMENT OF FORCE AND DEFLECTION. In *The 3rd European Medical and Biological Engineering Conference*. Prague.
- Ramasubramanian, M. K., Barham, O. M., & Swaminathan, V. (2008). Mechanics of a mosquito bite with applications to microneedle design. *Bioinspiration & Biomimetics*, 3(4), 10.
- Reddy, J. N. (2008). *An Introduction to Continuum Mechanics*. New York, NY, USA: Cambridge University Press.
- Reyssat, E., Tallinen, T., Le Merrer, M., & Mahadevan, L. (2012). Slicing Softly with Shear. *Physical Review Letters*, 109(24), 244301.
- Ryu, S. C., Renaud, P., Black, R. J., Daniel, B. L., & Cutkosky, M. R. (2011). Feasibility Study of an Optically Actuated MR-compatible Active Needle. In *IEEE/RSJ International Conference on Intelligent Robots and Systems (IROS)* (pp. 2564–2569). San Francisco, CA, USA: IEEE.

- Sacks, J., Welch, W. J., Mitchell, T. J., & Wynn, H. P. (1989). Design and Analysis of Computer Experiments. *Statistical Science*, 4(4), 409–423.
- Sahlabadi, M., & Hutapea, P. (2018). Novel design of honeybee-inspired needles for percutaneous procedure. *Bioinspiration & Biomimetics*, 13(3), 036013.
- Shin, S. J. (2016). *A Comprehensive Guide to Core Needle Biopsies of the Breast*. Cham: Springer International Publishing.
- Shoffstall, A. J., Srinivasan, S., Willis, M., Stiller, A. M., Ecker, M., Voit, W. E., ... Capadona, J. R. (2018). A Mosquito Inspired Strategy to Implant Microprobes into the Brain. *Scientific Reports*, 8(122), 1–10.
- Slocum, A. (1992). *Precision Machine Design*. (S. of M. Engineers, Ed.). Dearborn, MI, USA: Society of Manufacturing Engineers.
- Suzuki, M., Takahashi, T., & Aoyagi, S. (2018). 3D laser lithographic fabrication of hollow microneedle mimicking mosquitos and its characterisation. *International Journal of Nanotechnology*, 15(1/2/3), 157–173.
- Tao, S., Shintani, K., Bostanabad, R., Chan, Y.-C., Yang, G., Meingast, H., & Chen, W. (2017). Enhanced Gaussian Process Metamodeling and Collaborative Optimization for Vehicle Suspension Design Optimization. In *Volume 2B: 43rd Design Automation Conference* (p. V02BT03A039). Cleveland, OH, USA: ASME.
- Toal, D. J. J., Bressloff, N. W., Keane, A. J., & Holden, C. M. E. (2011). The development of a hybridized particle swarm for kriging hyperparameter tuning. *Engineering Optimization*, 43(6), 675–699.
- Wan, G., Wei, Z., Gardi, L., Downey, D. B., & Fenster, A. (2005). Brachytherapy needle deflection evaluation and correction. *Medical Physics*, 32(4), 902–909.
- Wang, Y., Tai, B. L., Yu, H., & Shih, A. J. (2014). Silicone-Based Tissue-Mimicking Phantom for Needle Insertion Simulation. *Journal of Medical Devices*, 8(2), 021001.
- Zhang, W., Bostanabad, R., Liang, B., Su, X., Zeng, D., Bessa, M. A., ... Cao, J. (2019). A numerical Bayesian-calibrated characterization method for multiscale prepreg preforming simulations with tension-shear coupling. *Composites Science and Technology*, 170, 15–24.
- Zheng, H., Zhang, Q., Moore, J. Z., Schwartz, J., McGill, C., P.W., M., & Shih, A. J. (2008). Biopsy needle tissue cutting analysis. In *Proceedings of the 8th International Conference on frontiers of design and manufacturing* (pp. 23–26). Tianjin, China.
- Zuber, T. J. (2002). *Punch Biopsy of the Skin*. *American Family Physicians* (Vol. 65).

Zucker Karl A. (2001). *Surgical Laparoscopy*. (2nd, Ed.), *Surgical Laparoscopy*. Philadelphia, PA, USA: Lippincott Williams & Wilkins.

Appendix A: Soft Tissue PVC Parameters

A1. S/P ratio: 0.25

Table A1. Material constants and fitting coefficients for phantom tissue with an S/P ratio equal to 0.25.

Model	Material Constants	R ²	RMSE
<i>Arruda – Boyce</i>	$\mu = 0.238$ $\lambda = 2.024$	0.9776	0.0206
<i>Ogden</i>	$\mu_1 = -0.0136$ $\alpha_1 = 4.538$ $\mu_2 = 0.0143$ $\alpha_2 = 4.658$ $\mu_3 = 0.00053$ $\alpha_3 = -5.94$	0.9647	0.0206

A2. S/P ratio: 0.5

Table A2. Material constants and fitting coefficients for phantom tissue with an S/P ratio equal to 0.5.

Model	Material Constants	R ²	RMSE
<i>Arruda – Boyce</i>	$\mu = 0.0058$ $\lambda = 1.35$	0.984	0.0058
<i>Ogden</i>	$\mu_1 = -0.175$ $\alpha_1 = -1.58$ $\mu_2 = 0.0113$ $\alpha_2 = 3.798$ $\mu_3 = 0.165$ $\alpha_3 = -1.74$	0.998	0.0018

A3. S/P ratio: 1

Table A3. Material constants and fitting coefficients for phantom tissue with an S/P ratio equal to 1.

Model	Material Constants	R ²	RMSE
<i>Arruda – Boyce</i>	$\mu = 0.0008$ $\lambda = 1.198$	0.834	0.018
<i>Ogden</i>	$\mu_1 = -0.0255$ $\alpha_1 = -3.91$ $\mu_2 = 0.0088$ $\alpha_2 = 4.74$ $\mu_3 = 0.0249$ $\alpha_3 = -4.09$	0.997	0.002

Appendix B: Abaqus Input Files

B1. 3D FEM Model

```

*Heading
** Job name: jt3av50 Model name: 3D FEM Model
** Generated by: Abaqus/CAE 6.14-2
*Preprint, echo=NO, model=NO, history=NO, contact=NO
**
** PARTS
**
*Part, name=BP_mesh2
*Node
**37255 lines
*Element, type=R3D4
**37105 lines
*Element, type=R3D3
**24 lines
*Node
  37256, 0., 0., 6.
*Nset, nset=BP_mesh2-RefPt_, internal
37256,
*Nset, nset=Set-1
  37256,
*Element, type=MASS, elset=Set-1_Inertia-1_
37130, 37256
*Mass, elset=Set-1_Inertia-1_
0.5e-08,
*End Part
**
*Part, name=tis33
*Node
**920345 lines
*Element, type=C3D8R
**882900 lines
*Element, type=C3D6
**5400 lines
*Elset, elset=Set-1, generate
  7367, 895666, 1
** Region: (Section-3:Set-1), (Controls:EC-1)
*Elset, elset=_I1, internal
**55182 lines

```

```

** Section: Section-3
*Solid Section, elset=_I1, controls=EC-1, material=Tissue
,
** Region: (Section-3:Set-1), (Controls:Default)
*Elset, elset=_I2, internal
**338 lines
** Section: Section-3
*Solid Section, elset=_I2, material=Tissue
,
*End Part
**
**
** ASSEMBLY
**
*Assembly, name=Assembly
**
*Instance, name=BP_mesh2-1, part=BP_mesh2
    0.,    0.,    15.85
    0.,    0.,    15.85,    1.,    0.,    15.85,    180.
*End Instance
**
*Instance, name=tis33-1, part=tis33
*End Instance
**
*Nset, nset=Set-5, instance=BP_mesh2-1, generate
    1, 37255,    1
*Nset, nset=Set-6, instance=BP_mesh2-1, generate
    1, 37255,    1
*Nset, nset=Set-7, instance=BP_mesh2-1
    37256,
*Nset, nset=Set-9, instance=BP_mesh2-1
    37256,
*Nset, nset=Set-10, instance=tis33-1
**1633 lines
*Nset, nset=Set-11, instance=tis33-1
**1633 lines
*Nset, nset=Set-12, instance=tis33-1
**381 lines
*Elset, elset=TissueDef, instance=tis33-1, generate
    7367, 895666,    1
*Elset, elset=b_Set-7, instance=BP_mesh2-1, generate
    1, 37129,    1
*Elset, elset=b_Set-10, instance=BP_mesh2-1, generate
    1, 37129,    1
*Nset, nset=_PickedSet49, internal, instance=BP_mesh2-1

```

```

37256,
*Elset, elset=_Surf-2_S1, internal, instance=tis33-1, generate
  7367, 895517, 150
*Surface, type=ELEMENT, name=Surf-2
_Surf-2_S1, S1
*Elset, elset=_m_Surf-5_SPOS, internal, instance=BP_mesh2-1, generate
  1, 37129, 1
*Surface, type=ELEMENT, name=m_Surf-5
_m_Surf-5_SPOS, SPOS
** Constraint: Constraint-1
*Rigid Body, ref node=_PickedSet49, elset=b_Set-10
*End Assembly
**
** ELEMENT CONTROLS
**
*Section Controls, name=EC-1, DISTORTION CONTROL=YES, hourglass=ENHANCED
1., 1., 1.
*Amplitude, name=Amp-1
  0., 0., 0.108, 6.5
**
** MATERIALS
**
*Material, name=Tissue
*Density
20e-08,
*Hyperelastic, arruda-boyce
0.00418, 1.15, 2.14
**
** INTERACTION PROPERTIES
**
*Surface Interaction, name=Tissue_contact
*Friction
0.28,
*Surface Behavior, pressure-overclosure=HARD
**
** BOUNDARY CONDITIONS
**
** Name: BP_buondary Type: Displacement/Rotation
*Boundary
Set-9, 1, 1
Set-9, 2, 2
Set-9, 4, 4
Set-9, 5, 5
Set-9, 6, 6
** Name: bottomfixed Type: Symmetry/Antisymmetry/Encastre
*Boundary

```

```

Set-12, ENCASTRE
** Name: xsy Type: Symmetry/Antisymmetry/Encastre
*Boundary
Set-10, XSYMM
** Name: ysy Type: Symmetry/Antisymmetry/Encastre
*Boundary
Set-11, YSYMM
**
** INTERACTIONS
**
** Interaction: Int-1
*Contact, op=NEW
*Contact Inclusions
m_Surf-5 , Surf-2
*Contact Property Assignment
, , Tissue_contact
*Contact Formulation, type=PURE MASTER-SLAVE
m_Surf-5 , Surf-2 , MASTER
** -----
**
** STEP: Step-1
**
*Step, name=Step-1, nlgeom=YES
*Dynamic, Explicit
, 0.108
*Bulk Viscosity
0.06, 1.2
**
** BOUNDARY CONDITIONS
**
** Name: BP_motion Type: Displacement/Rotation
*Boundary, amplitude=Amp-1
Set-7, 3, 3, -1.
**
** OUTPUT REQUESTS
**
*Restart, write, number interval=1, time marks=NO
**
** FIELD OUTPUT: F-Output-1
**
*Output, field, number interval=50
*Node Output
A, RF, U, V
*Element Output, directions=YES
EVF, LE, PE, PEEQ, PEEQVAVG, PEVAVG, S, SVAVG
*Contact Output

```

```

CFORCE, CSTRESS
**
** HISTORY OUTPUT: H-Output-1
**
*Output, history, time interval=0.0021
*Element Output, elset=TissueDef, variable=PRESELECT
*Integrated Output, elset=TissueDef, variable=PRESELECT
*Energy Output, elset=TissueDef, variable=PRESELECT
*Incrementation Output, variable=PRESELECT
*End Step

```

B2. 2D FEM Model

```

*Heading
** Job name: jaxi4 Model name: 2D FEM Model
** Generated by: Abaqus/CAE 6.14-2
** Preprint, echo=NO, model=NO, history=NO, contact=NO
**
** PARTS
**
*Part, name=BP
*End Part
**
*Part, name=Tissue
*Node
**54540 lines
*Element, type=CAX4RH
**54058 lines
*Nset, nset=Set-1, generate
  1, 54540,  1
*Elset, elset=Set-1, generate
  1, 54058,  1
** Section: Section-1
*Solid Section, elset=Set-1, material=Tissue
,
*End Part
**
**
** ASSEMBLY
**
*Assembly, name=Assembly
**
*Instance, name=BP-1, part=BP
  0.,  0.5,  0.

```

```

*Node
  1,    0.,    10.,    0.
*Nset, nset=BP-1-RefPt_, internal
1,
*Nset, nset=Set-1
1,
*Surface, type=SEGMENTS, name=m_Surf-1
*Rigid Body, ref node=BP-1-RefPt_, analytical surface=m_Surf-1
*Element, type=MASS, elset=Set-1_Inertia-1_
1, 1
*Mass, elset=Set-1_Inertia-1_
5e-09,
*End Instance
**
*Instance, name=Part-2-1, part=Tissue
  0.,   -7.,    0.
*End Instance
**
*Nset, nset=Set-1, instance=Part-2-1
**19 lines
*Elset, elset=Set-1, instance=Part-2-1
**19 lines
*Nset, nset=Set-2, instance=BP-1
1,
*Nset, nset=Set-3, instance=Part-2-1
**12 lines
*Elset, elset=Set-3, instance=Part-2-1, generate
22913, 23091, 1
*Nset, nset=Set-4, instance=Part-2-1
**19 lines
*Elset, elset=Set-4, instance=Part-2-1
**19 lines
*Nset, nset=Set-8, instance=BP-1
1,
*Nset, nset=Tissue, instance=Part-2-1, generate
1, 54540, 1
*Elset, elset=Tissue, instance=Part-2-1, generate
1, 54058, 1
*Nset, nset=_PickedSet19, internal, instance=Part-2-1, generate
1, 54540, 1
*Elset, elset=_PickedSet19, internal, instance=Part-2-1, generate
1, 54058, 1
*Nset, nset=_PickedSet20, internal, instance=Part-2-1, generate
1, 54540, 1
*Elset, elset=_PickedSet20, internal, instance=Part-2-1, generate
1, 54058, 1

```

```

*Elset, elset=_s_Surf-1_S2, internal, instance=Part-2-1, generate
 179, 23091, 179
*Elset, elset=_s_Surf-1_S4, internal, instance=Part-2-1, generate
23092, 53880, 179
*Surface, type=ELEMENT, name=s_Surf-1
_s_Surf-1_S2, S2
_s_Surf-1_S4, S4
*End Assembly
*Amplitude, name=Amp-1
    0.,    0.,    1.,    5.5
**
** MATERIALS
**
*Material, name=Tissue
*Density
 1e-06,
*Hyperelastic, arruda-boyce
0.00418, 1.15, 10.7
**
** INTERACTION PROPERTIES
**
*Surface Interaction, name=IntProp-1
1.,
*Friction, slip tolerance=0.005
0.28,
*Surface Behavior, pressure-overclosure=HARD
**
** BOUNDARY CONDITIONS
**
** Name: BC-1 Type: Symmetry/Antisymmetry/Encastre
*Boundary
Set-1, ENCASTRE
** Name: BC-3 Type: Symmetry/Antisymmetry/Encastre
*Boundary
Set-3, XSYMM
**
** INTERACTIONS
**
** Interaction: Int-1
*Contact Pair, interaction=IntProp-1, type=SURFACE TO SURFACE
s_Surf-1, BP-1.m_Surf-1
** -----
**
** STEP: Step-1
**
*Step, name=Step-1, nlgeom=YES, inc=1000000

```

```

*Static, stabilize, allsdtol=0.05, continue=YES
0.001, 1., 1e-09, 1.
**
** BOUNDARY CONDITIONS
**
** Name: BC-4 Type: Displacement/Rotation
*Boundary, amplitude=Amp-1
Set-8, 1, 1
Set-8, 2, 2, -1.
Set-8, 6, 6
*Adaptive Mesh Controls, name=Ada-1
1., 0.
**
** CONTROLS
**
*Controls, reset
*Controls, analysis=discontinuous
*Controls, parameters=field, field=displacement
0.01, 0.1, , , , ,
*Controls, parameters=field, field=hydrostatic fluid pressure
0.01, 0.1, , , , ,
*Controls, parameters=field, field=rotation
0.01, 0.1, , , , ,
*Controls, parameters=field, field=electrical potential
0.01, 0.1, , , , ,
**
** OUTPUT REQUESTS
**
*Restart, write, frequency=0
**
** FIELD OUTPUT: F-Output-1
**
*Output, field, variable=PRESELECT, number interval=50, time marks=NO
**
** HISTORY OUTPUT: H-Output-1
**
*Output, history, variable=PRESELECT, number interval=50, time marks=NO
*End Step

```

B3. 3D FEM Model: Insertion with Slicing Motion

```

*Heading
** Job name: jpb3 Model name: 3D FEM Slice Model
** Generated by: Abaqus/CAE 6.14-2

```

```

*Preprint, echo=NO, model=NO, history=NO, contact=NO
**
** PARTS
**
*Part, name=BP_mesh2
*Node
**37255 lines
*Element, type=R3D4
**37105 lines
*Element, type=R3D3
**24 lines
*Node
  37256,    0.,    0.,    6.
*Nset, nset=BP_mesh2-RefPt_, internal
37256,
*Nset, nset=Set-1
  37256,
*End Part
**
*Part, name=Tisspbcc
*Node
**53001 lines
*Element, type=C3D6H
**150 lines
*Element, type=C3D8RH
**26100 lines
*Elset, elset=Set-1
**1641 lines
** Region: (Section-3:Set-1), (Controls:Default)
*Elset, elset=_I1, internal, generate
  1, 150, 1
** Section: Section-3
*Solid Section, elset=_I1, material=Tissue
,
** Region: (Section-3:Set-1), (Controls:EC-1)
*Elset, elset=_I2, internal, generate
  1001, 27100, 1
** Section: Section-3
*Solid Section, elset=_I2, controls=EC-1, material=Tissue
,
*End Part
**
**
** ASSEMBLY
**
*Assembly, name=Assembly

```

```

**
*Instance, name=BP_mesh2-1, part=BP_mesh2
    0.,    0.,    16.3
    0.,    0.,    16.3,    1.,    0.,    16.3,    180.
*End Instance
**
*Instance, name=Tisspbc-1, part=Tisspbc
*End Instance
**
*Elset, elset=b_Set-3, instance=BP_mesh2-1, generate
    1, 37129,    1
*Nset, nset=Set-1, instance=Tisspbc-1
1,
*Nset, nset=Set-2, instance=Tisspbc-1
2,
**Repeat until 52850
*Nset, nset=_PickedSet95, internal, instance=Tisspbc-1
**22 lines
*Nset, nset=_PickedSet98, internal, instance=BP_mesh2-1
37256,
*Nset, nset=_PickedSet104, internal, instance=BP_mesh2-1
37256,
*Elset, elset=_Surf-2_S1, internal, instance=Tisspbc-1
**11 lines
*Surface, type=ELEMENT, name=Surf-2
_Surf-2_S1, S1
*Elset, elset=_Surf-5bp_SPOS, internal, instance=BP_mesh2-1, generate
    1, 37129,    1
*Surface, type=ELEMENT, name=Surf-5bp
_Surf-5bp_SPOS, SPOS
*Elset, elset=_m_Surf-3_SPOS, internal, instance=BP_mesh2-1, generate
    1, 37129,    1
*Surface, type=ELEMENT, name=m_Surf-3
_m_Surf-3_SPOS, SPOS
*Elset, elset=_s_Surf-3_S1, internal, instance=Tisspbc-1

*Surface, type=ELEMENT, name=s_Surf-3
_s_Surf-3_S1, S1
*Nset, nset="_T-Datum csys-2", internal
**52851 lines
*Transform, nset="_T-Datum csys-2", type=C
    0., 0., 0., 0., 0., 1
**Constraint: Eqn-1
*Equation
2
Set-1, 1, 1.

```

```

Set-2, 1, -1.
***Similar conditions until Eqn-158549
** Constraint: Constraint-1
*Rigid Body, ref node=_PickedSet104, elset=b_Set-3
*End Assembly
**
** ELEMENT CONTROLS
**
*Section Controls, name=EC-1, hourglass=ENHANCED
1., 1., 1.
*Amplitude, name=Amp-1
      0.,      0.,      1.,      6.5
**
** MATERIALS
**
*Material, name=Tissue
*Hyperelastic, arruda-boyce
0.00418, 1.15, 10.7
**
** INTERACTION PROPERTIES
**
*Surface Interaction, name=Tissue_contact
1.,
*Friction, slip tolerance=0.005
0.40,
*Surface Behavior, pressure-overclosure=HARD
**
** BOUNDARY CONDITIONS
**
** Name: Tisbottom Type: Displacement/Rotation
*Boundary
_PickedSet95, 1, 1
_PickedSet95, 2, 2
_PickedSet95, 3, 3
_PickedSet95, 4, 4
_PickedSet95, 5, 5
_PickedSet95, 6, 6
**
** INTERACTIONS
**
** Interaction: Int-1
*Contact Pair, interaction=Tissue_contact, type=SURFACE TO SURFACE
s_Surf-3, m_Surf-3
** -----
**
** STEP: Step-1

```

```
**
*Step, name=Step-1, nlgeom=YES, inc=1000000, convert sdi=YES
*Static, stabilize, allsdtol=0.05, continue=YES
0.001, 1., 1e-09, 1.
**
** BOUNDARY CONDITIONS
**
** Name: BPmotion Type: Displacement/Rotation
*Boundary, amplitude=Amp-1
_PickedSet98, 1, 1
_PickedSet98, 2, 2
_PickedSet98, 3, 3, -1.
_PickedSet98, 4, 4
_PickedSet98, 5, 5
_PickedSet98, 6, 6, 0.5
**
** CONTROLS
**
*Controls, reset
*Controls, analysis=discontinuous
*Controls, parameters=field, field=displacement
0.01, 0.1, , , , ,
*Controls, parameters=field, field=hydrostatic fluid pressure
0.01, 0.1, , , , ,
*Controls, parameters=field, field=rotation
0.01, 0.1, , , , ,
*Controls, parameters=field, field=electrical potential
0.01, 0.1, , , , ,
**
** OUTPUT REQUESTS
**
*Restart, write, frequency=0
**
** FIELD OUTPUT: F-Output-1
**
*Output, field, variable=PRESELECT, number interval=100, time marks=NO
**
** HISTORY OUTPUT: H-Output-1
**
*Output, history, variable=PRESELECT, number interval=100, time marks=NO
*End Step
```

B4. 3D FEM Model: Micro-Serrated Biopsy Punches

```

*Heading
** Job name: jms325 Model name: 3D Microserration Model
** Generated by: Abaqus/CAE 6.14-2
*Preprint, echo=NO, model=NO, history=NO, contact=NO
**
** PARTS
**
*Part, name=BP_serr_d600um_step
*Node
**148637 lines
*Element, type=R3D4
**146689 lines
*Element, type=R3D3
**3896 lines
*Node
148638,      0., -7.26360068e-17, 5.80000019
*Nset, nset=BP_serr_d600um_step-RefPt_, internal
148638,
*Nset, nset=Set-1
148638,
*Element, type=MASS, elset=Set-1_Inertia-1_
150586, 148638
*Mass, elset=Set-1_Inertia-1_
5e-09,
*End Part
**
*Part, name=Tissue
*Node
**2499690 lines
*Element, type=C3D8R
**2371968 lines
*Element, type=C3D6
**78300 lines
*Elset, elset=Set-1
**153142 lines
** Region: (Section-tissue400:Set-1), (Controls:EC-1)
*Elset, elset=_I1, internal
**148248 lines
** Section: Section-tissue400
*Solid Section, elset=_I1, controls=EC-1, material=Tissue
,
** Region: (Section-tissue400:Set-1), (Controls:Default)
*Elset, elset=_I2, internal

```

```

**4894 lines
** Section: Section-tissue400
*Solid Section, elset=_I2, material=Tissue
,
*End Part
**
**
** ASSEMBLY
**
*Assembly, name=Assembly
**
*Instance, name=BP_serr_d600um_step-1, part=BP_serr_d600um_step
    0.,    0.,    15.85
    0.,    0.,    15.85,    0.,    1.,    15.85,    180.
*End Instance
**
*Instance, name=Tissue-1, part=Tissue
*End Instance
**
*Nset, nset=Set-42, instance=BP_serr_d600um_step-1
148638,
*Nset, nset=Set-43, instance=BP_serr_d600um_step-1
148638,
*Nset, nset=Set-45, instance=Tissue-1, generate
2485369, 2568691,    1
*Nset, nset=Set-46, instance=Tissue-1
**171 lines
*Nset, nset=Set-47, instance=Tissue-1
**171 lines
*Nset, nset=b_Set-40, instance=BP_serr_d600um_step-1, generate
1, 148637,    1
*Elset, elset=b_Set-40, instance=BP_serr_d600um_step-1, generate
1, 150585,    1
*Nset, nset=b_Set-44, instance=BP_serr_d600um_step-1, generate
1, 148637,    1
*Elset, elset=b_Set-44, instance=BP_serr_d600um_step-1, generate
1, 150585,    1
*Nset, nset=_PickedSet131, internal, instance=BP_serr_d600um_step-1
148638,
*Elset, elset=_BP_serr_SPOS, internal, instance=BP_serr_d600um_step-1, generate
1, 150585,    1
*Surface, type=ELEMENT, name=BP_serr
_BP_serr_SPOS, SPOS
*Elset, elset=_Tissue_S1, internal, instance=Tissue-1, generate
152049, 236540,    1
*Surface, type=ELEMENT, name=Tissue

```

```

_Tissue_S1, S1
** Constraint: Constraint-2
*Rigid Body, ref node=_PickedSet131, elset=b_Set-44
*End Assembly
**
** ELEMENT CONTROLS
**
*Section Controls, name=EC-1, hourglass=ENHANCED
1., 1., 1.
*Amplitude, name=Amp-1
    0.,    0.,    1.25,    1.25
**
** MATERIALS
**
*Material, name=Tissue
*Density
200e-06,
*Hyperelastic, arruda-boyce
0.0238, 2.024, 0.705
**
** INTERACTION PROPERTIES
**
*Surface Interaction, name=IntProp-1
*Friction
0.28,
*Surface Behavior, pressure-overclosure=HARD
**
** BOUNDARY CONDITIONS
**
** Name: BP_boundary Type: Displacement/Rotation
*Boundary
Set-42, 1, 1
Set-42, 2, 2
Set-42, 4, 4
Set-42, 5, 5
Set-42, 6, 6
** Name: Encastre Type: Symmetry/Antisymmetry/Encastre
*Boundary
Set-45, ENCASTRE
** Name: Xsymm Type: Symmetry/Antisymmetry/Encastre
*Boundary
Set-47, XSYMM
** Name: Ysymm Type: Symmetry/Antisymmetry/Encastre
*Boundary
Set-46, YSYMM
** -----

```

```

**
** STEP: Step-1
**
*Step, name=Step-1, nlgeom=YES
*Dynamic, Explicit
, 1.25
*Bulk Viscosity
0.06, 1.2
**
** BOUNDARY CONDITIONS
**
** Name: BP_motion Type: Displacement/Rotation
*Boundary, amplitude=Amp-1
Set-43, 3, 3, -1.
**
** INTERACTIONS
**
** Interaction: Int-1
*Contact, op=NEW
*Contact Inclusions
BP_serr , Tissue
*Contact Property Assignment
, , IntProp-1
*Contact Formulation, type=PURE MASTER-SLAVE
BP_serr , Tissue , MASTER
**
** OUTPUT REQUESTS
**
*Restart, write, number interval=1, time marks=NO
**
** FIELD OUTPUT: F-Output-1
**
*Output, field, variable=PRESELECT, number interval=125
**
** HISTORY OUTPUT: H-Output-2
**
*Output, history, time interval=0.025
*Energy Output, elset=Tissue-1.Set-1
ALLAE, ALLCD, ALLCW, ALLDC, ALLDMD, ALLFD, ALLIE, ALLKE, ALLMW, ALLPD, ALLPW,
ALLSE, ALLVD, ALLWK, ETOTAL
*End Step

```

B5. 2D FEM Model: Micro-Serrated Biopsy Punches

```

*Heading
** Job name: jserr4002 Model name: 3D Microserration Model
** Generated by: Abaqus/CAE 6.14-2
*Preprint, echo=NO, model=NO, history=NO, contact=NO
**
** PARTS
**
*Part, name=BP_serr400
*End Part
**
*Part, name=TissueBlock
*Node
**95872 lines
*Element, type=CPS4R
**94996 lines
*Nset, nset=Set-175, generate
  1, 95872, 1
*Elset, elset=Set-175, generate
  1, 94996, 1
** Section: ArrudaBoyceSection
*Solid Section, elset=Set-175, material=ArrudaBoyceAbq
1.,
*End Part
**
**
** ASSEMBLY
**
*Assembly, name=Assembly
**
*Instance, name=TissueBlock-1, part=TissueBlock
*End Instance
**
*Instance, name=BP_serr400-1, part=BP_serr400
3.6800004956546, 4.25, 0.
*Node
  1, 1.32000005, 2., 0.
*Nset, nset=BP_serr400-1-RefPt_, internal
1,
*Nset, nset=Set-1
1,
*Surface, type=SEGMENTS, name=m_Surf-5
**19 lines
*Rigid Body, ref node=BP_serr400-1-RefPt_, analytical surface=m_Surf-5

```

```

*Element, type=MASS, elset=Set-1_Inertia-1_
1, 1
*Mass, elset=Set-1_Inertia-1_
0.001,
*End Instance
**
*Nset, nset=Set-12, instance=TissueBlock-1
** 47 lines
*Elset, elset=Set-12, instance=TissueBlock-1
**47 lines
*Nset, nset=Set-13, instance=BP_serr400-1
1,
*Elset, elset=_s_Surf-7_S4, internal, instance=TissueBlock-1
**40 lines
*Elset, elset=_s_Surf-7_S2, internal, instance=TissueBlock-1, generate
65659, 80264, 127
*Surface, type=ELEMENT, name=s_Surf-7
_s_Surf-7_S4, S4
_s_Surf-7_S2, S2
*End Assembly
*Amplitude, name=Amp1
0., 0., 1., 3.25
**
** MATERIALS
**
*Material, name=ArrudaBoyceAbq
*Density
4e-07,
*Hyperelastic, arruda-boyce
0.0238, 2.024, 1.41
**
** INTERACTION PROPERTIES
**
*Surface Interaction, name=ContactProp
1,
*Friction, slip tolerance=0.005
0.28,
*Surface Behavior, pressure-overclosure=HARD
**
** BOUNDARY CONDITIONS
**
** Name: Encastre Type: Symmetry/Antisymmetry/Encastre
*Boundary
Set-12, ENCASTRE
**
** INTERACTIONS

```

```
**
** Interaction: Int-1
** *Contact Pair, interaction=ContactProp, type=SURFACE TO SURFACE
s_Surf-7, BP_serr400-1.m_Surf-5
** -----
**
** STEP: Blade_insertion
**
** *Step, name=Blade_insertion, nlgeom=YES, inc=100000
** *Dynamic,application=QUASI-STATIC,initial=NO
0.001,1,1e-05
**
** BOUNDARY CONDITIONS
**
** Name: BP_motion Type: Displacement/Rotation
** *Boundary, amplitude=Amp1
Set-13, 1, 1
Set-13, 2, 2, -1.
Set-13, 6, 6
**
** OUTPUT REQUESTS
**
** *Restart, write, number interval=1, time marks=NO
**
** FIELD OUTPUT: F-Output-1
**
** *Output, field, variable=PRESELECT, number interval=100, time marks=NO
**
** HISTORY OUTPUT: H-Output-1
**
** *Output, history, variable=PRESELECT, number interval=100, time marks=NO
** *End Ste
```

Appendix C: Code for Laser Ablation

```

;REPETITION RATE: 100 kHz
;LASER POWER OF 532 NM LASER: 0.75W

dvar $feed, $overlap, $pulse_time, $passover, $pass2, $radius, $beam_dia, $overlap_R, $dist_R,
$comp, $radius_i, $comp_i

SECONDS

$beam_dia = 0.02
$radius_i= 0.150
$comp_i= 0.05
$radius= 0.150
$comp= 0.05

$overlap_R = 0.95
$dist_R = (1-$overlap_R)*$beam_dia

$passover= 0.020/$dist_R;
$pass2= 80; 60

$feed =0.1;

G92 X-0.05 Y-0.05 ; set zero
G92 C0

T0

G44 X Y ; activate possible compensation on x and y axe

T1 ; load the laser beam: tool table available from CNC operator interface,

G91

PSOPULSE X TIME 10 5 CYCLES 10000000 ; original 40 20

REPEAT 16 ; Make serrations all around the circumference

      REPEAT $passover

                PSOCONTROL X FIRE

```

```

G01 G41 X$comp F $feed ;
G1 Y0.05 ;
G03 X-($radius*2) Y0 I-$radius J0 ;

```

```

PSOCONTROL X OFF

```

```

G1 Y -0.05
G40 X$comp
G0 X (2*$radius_i-2*$comp_i)
$radius = $radius - $dist_R
$comp = $comp - $dist_R

```

```

END REPEAT

```

```

PSOPULSE X TIME 10 5 CYCLES 10000000;ORIGINAL 20 10

```

```

REPEAT $pass2 ; Make serrations all around the circumference

```

```

PSOCONTROL X FIRE

```

```

G01 G41 X$comp_i F $feed ;
G1 Y0.05 ;
G03 X-($radius_i*2) Y0 I-$radius_i J0 ;

```

```

PSOCONTROL X OFF

```

```

G1 Y -0.05
G40 X$comp_i
G0 X (2*$radius_i-2*$comp_i)

```

```

END REPEAT

```

```

G98 LINEAR Y 0.0 C22.5 F1.0 E 5

```

```

END REPEAT

```

```

T0 ; unload the tool: laser beam

```

```

END

```